UNIVERSITY OF OKLAHOMA

GRADUATE COLLEGE

The Search for White Dwarf Binaries in Astronomical Survey Data

A DISSERTATION

SUBMITTED TO THE GRADUATE FACULTY

in partial fulfillment of the requirements for the

Degree of

DOCTOR OF PHILOSOPHY

By

ALEKZANDER R. KOSAKOWSKI
Norman, Oklahoma
2021

THE SEARCH FOR WHITE DWARF BINARIES IN ASTRONOMICAL SURVEY DATA

A DISSERTATION APPROVED FOR THE
HOMER L. DODGE DEPARTMENT OF PHYSICS AND ASTRONOMY

BY THE COMMITTEE CONSISTING OF

Dr. Mukremin Kilic, Chair

Dr. Trina Hope

Dr. Xinyu Dai

Dr. Karen Leighly

Dr. John Wisniewski

Acknowledgements

I acknowledge Dr. Mukremin Kilic, my graduate advisor, for his contribution to my success as a graduate student, researcher, and professional astronomer. The guidance provided to me by Dr. Kilic has allowed me to establish myself as an active member of the professional scientific community.

I acknowledge Dr. Thomas Pannuti, my undergraduate advisor, for his contribution to my success as a researcher. Dr. Pannuti introduced me to scientific research and provided to me the tools and encouragement that I needed to take my first steps into the field of astronomy.

I acknowledge Dr. Warren Brown's contributions to the success of my dissertation as well as the success of my completed and ongoing projects. In addition to laying the ground work for part of this dissertation through the ELM Survey, Dr. Brown provided follow-up observations for countless scientifically valuable targets with his telescope access and invaluable feedback towards my research goals and methods as well as feedback on my submitted manuscripts which significantly improved their quality.

Finally, I acknowledge the contribution of my PhD committee: Dr. Xinyu Dai, Dr. Trina Hope, Dr. Karen Leighly, and Dr. John Wisniewski to my success throughout the program.

Table of Contents

List of Tables

List of Figures

Abstract

Extremely low mass (ELM) white dwarfs are excellent laboratories for studying a variety of astrophysical phenomena, including common-envelope evolution, gravitational wave emission, and merger physics. A significant amount of work has been done to identify extremely low mass white dwarfs in the northern hemisphere using various photometric surveys, such as SDSS and Pan-STARRS.

In this dissertation, I present my follow-up observations of a low-mass, eclipsing, white dwarf binary and use the data to begin the process of directly measuring the binary's rate of orbital decay due to gravitational wave emission. These measurements can be used to obtain an independent measurement of the mass of the binary as well as constrain the effects of tides through a measured offset in orbital decay rate from a purely gravitational wave model (see Piro, 2011; Benacquista et al., 2011).

I then begin the search for ELM white dwarfs in the southern hemisphere (the ELM Survey South) through a large, targeted, spectroscopic survey using the SOAR 4.1-meter telescope. This search makes use of the southern-sky photometric surveys ATLAS and SkyMapper to identify a population of white dwarf binaries in color-color space which yields a small number of low-mass white dwarfs in a large pool of candidates. The target selection criteria are expanded to include the European Space Agency's *Gaia* Data Release 2 astrometry and photometry as soon as it became available. By using reliable parallax measurements and precise magnitudes, one is able to selectively target ELM white dwarfs with significantly higher accuracy than when using a pure photometric approach.

In preparation for the next phase of the ELM Survey South, I make use of the Zwicky Transient Facility (ZTF) public photometric survey to demonstrate the effectiveness of identifying exotic variables, including double white dwarf binaries, in large survey data sets. I make use of the Box Least Squares (BLS) period finding algorithm to identify eclipsing binaries within the public ZTF data archive and present photometric and spectroscopic analyses to a select few systems, including white dwarfs and hot subdwarf stars with main sequence companions. The methods developed here will be used as a starting point towards expanding the search for ELM white dwarfs in the southern hemisphere with the upcoming large-scale photometric surveys BlackGEM and the Vera Rubin Observatory's LSST program.

Chapter 1

Introduction

1.1 White dwarfs

It is well understood that, through single star evolution, stars with mass less than about 8 $M_\odot$ will end their core-burning lives and become small, degenerate objects known as white dwarfs (Fontaine et al., 2001). White dwarfs are supported against gravitational collapse through electron degeneracy pressure, a consequence of the Pauli exclusion principle in a Fermi gas preventing electrons from occupying filled energy levels. The mass distribution for nearby ($d < 100$ pc) white dwarfs shows a dominant peak at $M_{\rm WD} = 0.59$ $\rm M_\odot$, with a shoulder extending from $M_{\rm WD} \approx 0.7 - 0.9$ $\rm M_\odot$ (Kilic et al., 2020). White dwarf radii are on the order of $R_{\rm WD} \sim 0.01$ $\rm R_\odot$, and because white dwarfs are degenerate objects, the more massive they are, the smaller their radii will be. Due to the degenerate nature of the cores of white dwarfs, the internal temperature is constant throughout the core. The heat reservoir of the white dwarf is slowly depleted by radiation through its non-degenerate atmosphere.

The core composition of a white dwarf is determined by its evolutionary history, and thus can be linked to the mass of the white dwarf. The mass of a white dwarf depends on its progenitor mass through the initial-final mass relation (see Weidemann & Koester, 1983; Kalirai et al., 2008; Williams et al., 2009; Cummings et al., 2018; Canton et al., 2019), and its evolutionary history. White dwarfs formed in binary systems may undergo one or more episodes of mass loss, such as strong stellar winds or common envelope

binary evolution, resulting in a white dwarf with low mass ($M_{\rm WD} \lesssim 0.5$ M$_\odot$). On the other hand, massive progenitor stars ($M \approx 8$ M$_\odot$) or binary double degenerate white dwarf mergers may form more massive white dwarfs. However, due to the limitations of electron degeneracy pressure, there is an upper limit to the allowed mass of a white dwarf. Under ideal conditions, a white dwarf with mass greater than the Chandrasekhar mass ($M_{\rm WD} \approx 1.4$ M$_\odot$; Chandrasekhar (1931)) will begin electron capture processes, during which the electrons and protons combine to form neutrons and release heat. The outcome of this process depends on the core composition of the white dwarf and how the massive white dwarf obtains such a high mass. Work by Nomoto & Iben (1985) towards the outcome of white dwarf mergers suggests that, for the merger of CO-core white dwarfs with a total mass larger than the Chandrasekhar limit, the result is strongly dependent on the mass transfer rate. For mass transfer rates larger than $\dot{M} \gtrsim 0.2\ \dot{M}_{\rm Eddington}$, carbon will ignite off-center due to the increasing temperature from accretion and lead to a ONeMg-core white dwarf, which may collapse into a stable neutron star through electron capture. While for mass transfer rates $\dot{M} \lesssim 0.2\ \dot{M}_{\rm Eddington}$, core-central carbon deflagration leads to a supernova explosion. Additionally, Webbink (1984) demonstrated that the merger of a double white dwarf binary with CO core compositions and total mass $M_{\rm total} \approx 1.45 - 2.4$ M$_\odot$ may lead to unstable mass transfer and result in a Type I supernova explosion (see also Nomoto, 1986; Schwab, 2021). However, a super-Chandrasekhar white dwarf is not a prerequisite for a supernova explosion. A sub-Chandrasekhar CO-core white dwarf accreting helium may ignite a helium shell flash, which then may produce an inward carbon detonation, potentially resulting in what is known as a "double-detonation“ supernova explosion (Nomoto, 1982a,b) (see also Polin et al., 2019; Gronow et al., 2021).

Because white dwarfs follow well-understood cooling tracks, it is possible to obtain the time the star has spent as a white dwarf, known as its "cooling age," if its mass, temperature, and atmospheric composition are known. While the cooling age is usually a good indicator of age of the white dwarf, there are events that act to rejuvenate a white dwarf and make it appear younger than it really is. For example, a single massive white dwarf formed through the merger of two lesser mass white dwarfs will not have an accurate measure of its cooling age due to the merger process. Even past-accretion from a binary companion would affect the cooling age, making a white dwarf appear younger than it really is. Despite these possibilities, the cooling age together with an estimate of its progenitor main sequence age based on the white dwarf mass, it becomes possible to estimate the total age of the star, and therefore the total age of the star's local environment. For example, Kilic et al. (2019) have used the Gaia population of white dwarfs to obtain an estimate on the age of the nearby Galactic halo (see also Winget et al., 1987; Liebert et al., 1988; Kalirai, 2012; Hansen et al., 2013; Torres et al., 2021). See Fontaine et al. (2001) for a detailed review of the uses of white dwarfs in cosmochronology.

1.2 White dwarf classification

A white dwarf is classified by the presence of specific elemental absorption or emission features within its spectrum. White dwarfs are labelled with a two or three letter classification system. The first letter is always a "D" to indicate that it is a degenerate object. The next letter depends on the features present in the object's spectrum. The most common classifications for white dwarfs are: DA, DB, DO, DQ, DZ, and DC. The

spectrum of a DA white dwarf is dominated by Hydrogen absorption features, without any other features present. DB and DO type white dwarfs are dominated by neutral and singly-ionized Helium absorption features, respectively. DQ white dwarfs are dominated by Carbon features. DZ white dwarfs show various metal absorption, which may include Calcium, Silicon, Magnesium, and Iron, among others. Finally, DC white dwarfs show no features, resulting in a smooth blackbody spectrum. Figure 1.1 presents a real-world optical spectrum for each of these classes of white dwarf, downloaded from the Montreal White Dwarf Database[1] (Dufour et al., 2017). White dwarfs that show evidence for two of these characteristics are classified by both types present, with the stronger spectral feature being labelled first. For example: a hydrogen-dominated atmosphere that shows strong hydrogen lines with weak neutral helium lines is classified as a DAB, while a helium-dominated atmosphere that shows strong helium lines and weak hydrogen lines is classified as a DBA. Wesemael et al. (1993) provide an excellent illustrative overview of the the various classifications of white dwarfs and their spectra.

[1] https://www.montrealwhitedwarfdatabase.org/

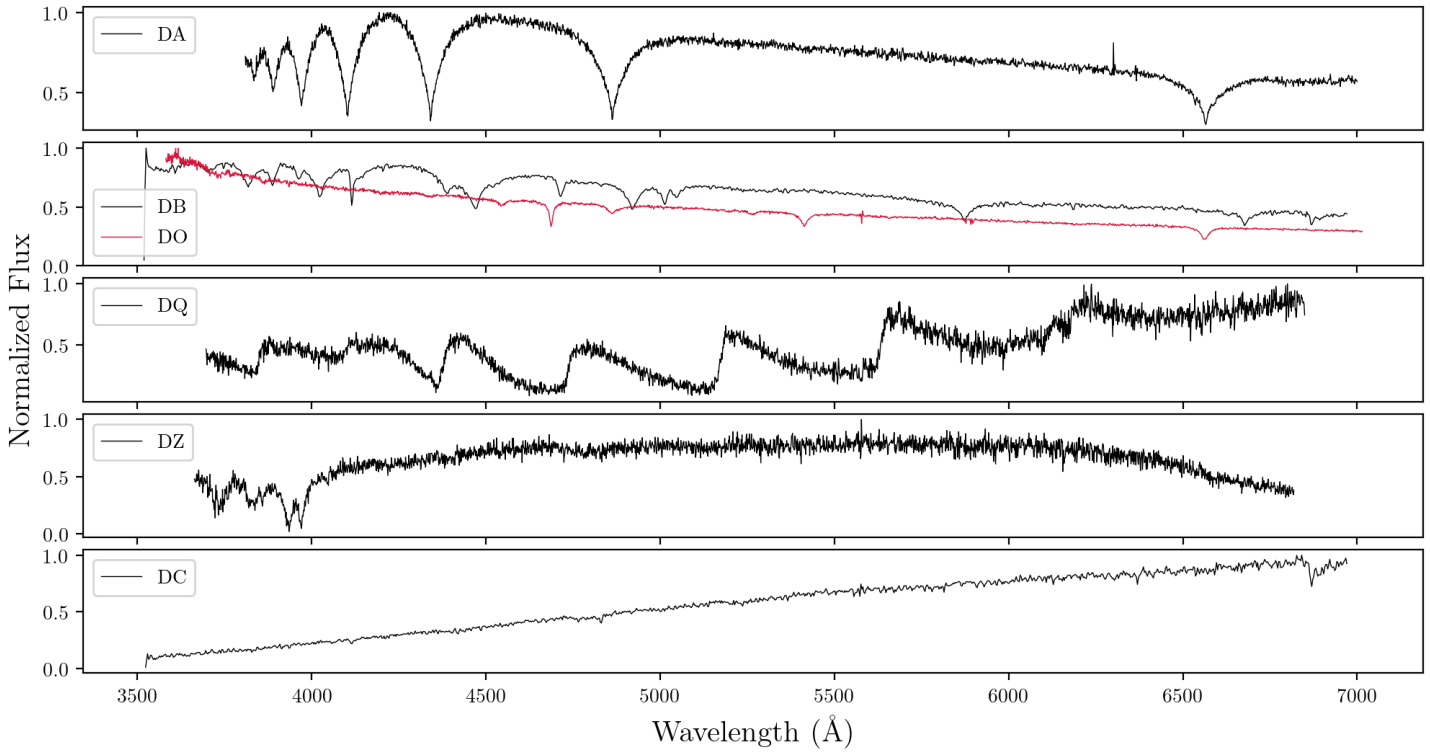

Fig. 1.1.— Example white dwarf spectra downloaded from the Montreal White Dwarf Database.

1.3 White Dwarf Spectroscopy

Because we are only able to directly observe the thin outer atmosphere of a white dwarf, our classifications are based entirely on the atmospheric composition, which varies based on physical properties of the star such as its effective temperature and the depth of its convection zone, as well as potential accretion from a companion or debris disk. While a detailed analysis of the spectral evolution of white dwarfs is beyond the scope of this dissertation, the interested reader is encouraged to continue reading on this topic with the work of Bédard et al. (2020). Information about the interior of the white dwarf must be obtained through detailed studies of stellar pulsations visible in the white dwarf's light curve. However, because white dwarfs only pulsate in specific temperature ranges known as the "instability strips" (Winget & Kepler, 2008; Van Grootel et al., 2012, 2015), studies of the white dwarf interior are a limited to these specific cases. Information obtained through studies of the white dwarf's spectra are limited to details about the star's atmospheric properties, such as its effective temperature, surface gravity, and atmospheric chemical composition.

The shape of the absorption features in a white dwarf's spectrum is described by the combination of the physics of many types of spectral line broadening, the most important of which being Stark broadening (Tremblay & Bergeron, 2009a); a type of pressure broadening caused by interactions between charged particles. With knowledge of spectral line broadening and radiative transfer processes, it becomes possible to create synthetic spectra representing the atmosphere of white dwarf with specific parameters. These synthetic spectra can then be directly compared to an observed white dwarf spectrum

to estimate the parameters of the observed white dwarf, including its surface gravity, effective temperature, Helium or metal abundance, and magnetic field strength. This method of obtaining observed white dwarf parameters through the use of synthetic spectra is known as the spectroscopic technique and was developed and implemented for a large sample of DA white dwarfs by Bergeron et al. (1992) to estimate white dwarf masses through spectroscopy.

Throughout this dissertation, I have applied a variation of this spectroscopic technique to determine the surface gravities ($\log g$ reported in cgs units) and effective temperatures ($T_{\rm eff}$ in units of Kelvin) for various DA white dwarfs. I follow the process described in Tremblay & Bergeron (2009a) (see also Liebert et al., 2005). In short: first, the observed spectrum and grid of synthetic spectra are split into the wavelength regions surrounding the absorption lines that are to be fitted. Next, each absorption line is normalized individually such that its continuum is unity. Finally, I apply a Levenberg-Marquardt minimization algorithm with a chi-squared merit function to the observed spectrum, using the grid of synthetic spectra. The first partial-derivatives of the synthetic spectra with respect to each of the fitted parameters are used in a steepest-descent-style approach towards finding the best-fitting model spectrum. Cubic-spline interpolation is applied across the grid of synthetic spectra to generate new models as the process iterates towards convergence on a best-fitting solution. Because the equivalent width of the Balmer lines peaks at around $T_{\rm eff} \approx 10,000 - 13,000$ K (see Daou et al., 1990; Bergeron et al., 1995), spectroscopic fits to white dwarfs may result in two chi-squared minima, one on each side of this temperature range. I perform the same fitting procedure to each target twice, once with initial temperature $T_{\rm eff,i} = 8000$ K (the "cold" solution) and once with initial

temperature $T_{\rm eff,i} = 20,000$ K (the "hot" solution). In the event that the two solutions result in different best-fitting models due to this chi-squared degeneracy, visual inspection of each solution is used to determine which fit to accept as the true solution. This inspection is based on how well the models fit the higher-order Balmer lines, which are strongly dependent on the surface gravity. A weighted chi-squared method may be appropriate for automating this selection depending on the quality of the observed spectrum. Comparison with photometric fits is occasionally required if the quality of the spectroscopic fits is poor. Figure 1.2 displays an output fit for the "cold“ solution (left) and the "hot“ solution (right) to the same spectrum. In this example, we accept the "cold" solution as it better fits the cores of the higher-order lines and the wings of the lower-order lines.

Because observed spectra do not have formal observed uncertainties for each observed data point, the reported best-fitting uncertainties are purely statistical and are based on the covariance matrix of the fit scaled by a correction factor obtained from the N-dimensional 1σ Gaussian contours in chi-squared space, where N is the number of parameters fit (see chapter 5.4 in Press (2002) for details on the Levenberg-Marquardt method and the statistical uncertainties associated with it). Therefore, while the reported uncertainties do strongly depend on the signal-to-noise ratio of the observed spectra, they are not observed uncertainties. In addition to the uncertainties associated with the fitting algorithm itself, Liebert et al. (2005) found sources of external errors to be $\sigma_g = 0.038$ dex and $\sigma_T = 1.2$ % in surface gravity and effective temperature, respectively, based on fits to many different spectra of the same white dwarfs. This additional external uncertainty should be added in quadrature with the uncertainty estimated from the covariance of the fit.

1.3.1 Extremely Low Mass White Dwarfs

Extremely Low Mass (ELM) white dwarfs are a relatively rare population of $M \leq 0.3\mathrm{M}_{\odot}$ He-core white dwarfs that form after severe mass loss. Because the main sequence lifetime of an ELM white dwarf progenitor through single-star evolution is longer than a Hubble time, the Universe is not yet old enough to form ELM white dwarfs through single-star evolution channels. Therefore, ELM white dwarf systems must form through binary interaction, typically following one of two dominant evolutionary channels: Roche lobe overflow or common-envelope evolution (Li et al., 2019). It should be noted that, while almost all of the known ELM white dwarf systems are found in compact binaries, Justham et al. (2009) predicted a population of single ELM white dwarfs that are the

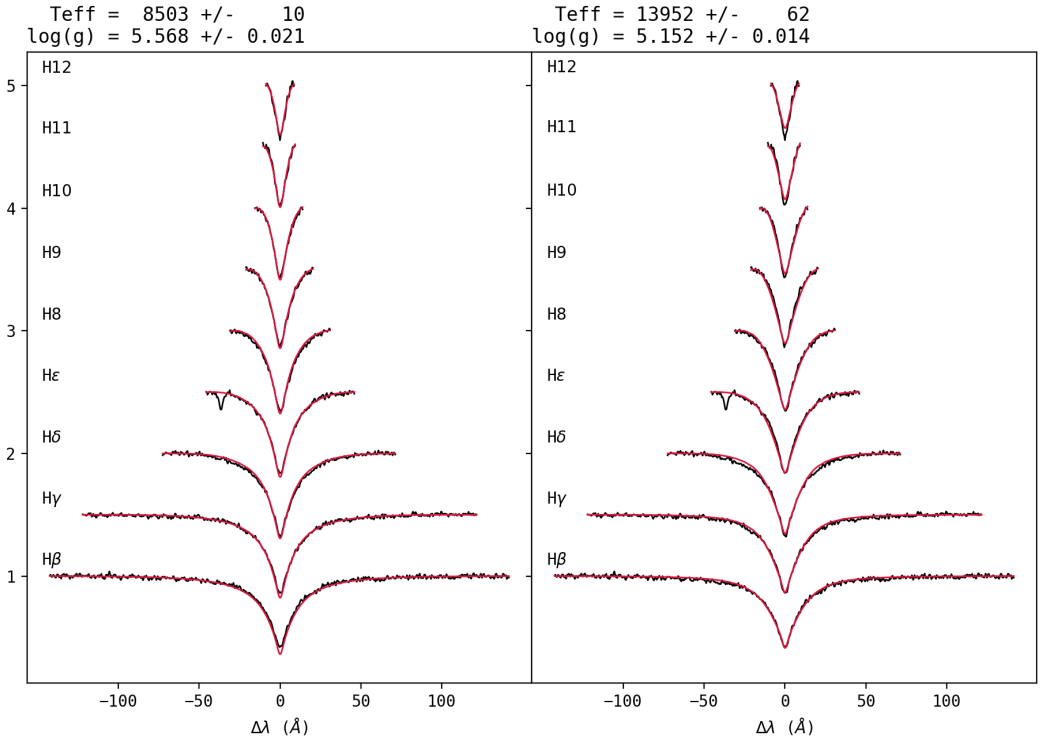

Fig. 1.2.— Example output from the spectroscopic fitting algorithm. The left plot shows the best-fitting "cold" solution to one of our targets. The right plot shows the best-fitting "hot" solution to the same target.

surviving cores of giant stars whose envelope was stripped by a companion during a supernova explosion.

In support of binary evolution models, virtually all known ELM white dwarfs are found in binary systems, with about half of the known systems expected to merge within a Hubble time due to the emission of gravitational waves (Kilic et al., 2010; Brown et al., 2010, 2020b). Compact double-degenerate merging systems are the dominant sources of the gravitational wave foreground at mHz frequencies (Nelemans et al., 2001; Nissanke et al., 2012; Korol et al., 2017; Lamberts et al., 2019). Identification of additional merging systems allows for better characterization of the gravitational wave foreground for the upcoming Laser Interferometer Space Antenna (LISA) mission. Because ELM white dwarfs form through binary evolution, studying such systems provides information about the relatively poorly-understood, and relatively short, common envelope stage of binary evolution.

The fate of ELM white dwarf systems is strongly dependent on the mass ratio of the stars in the system. The system's mass ratio determines whether eventual mass transfer is stable or unstable (Marsh et al., 2004; Kremer et al., 2017), which then determines the system's merger timescale and merger outcomes. Potential outcomes for these merging systems include single massive white dwarfs, supernovae, Helium-rich stars such as R CorBor stars, and AM CVn systems. While it is generally thought that stable mass transfer results in an AM CVn, Shen (2015) have shown that, through dynamical friction caused by nova outbursts, all interacting double-degenerate white dwarf systems may merge (see also Brown et al., 2016b). To fully understand the formation channels of these various merger outcomes, a more complete sample of merging progenitor systems

is needed. Because ELM white dwarf systems are signposts for compact binary systems, increasing the ELM white dwarf sample directly improves the sample of merging systems which provides stronger constraints on the formation channels and rates of the various merger products.

The ELM Survey

The ELM Survey (Kilic et al., 2010; Brown et al., 2010, 2020b) was designed to identify extremely low mass white dwarfs using color and magnitude information from SDSS photometry and spectroscopic fits to the available SDSS spectroscopy. White dwarfs were selected based on their colors and determined to be low mass through atmospheric parameters including surface gravities obtained through spectroscopic fits to their follow-up data. Radial velocity measurements were then used to determine if the white dwarf was in a binary. The first ELM white dwarfs of the ELM Survey were identified in a similar survey for Hypervelocity stars (Brown et al., 2006a,b). By the end of the eight-part ELM Survey project, 98 double white dwarf binaries had been discovered (Brown et al., 2020b).

Because the ELM Survey targeted white dwarfs with large velocity semi-amplitudes, it was biased towards identifying white dwarf binaries that evolved into compact configurations. This bias within the ELM Survey has two effects: 1. The ELM Survey's white dwarf sample provides an excellent sample of evolved systems from which we can study the details of common-envelope evolution and measure the formation rate of merger products from systems containing low-mass white dwarfs, especially in systems whose orbital configurations allow eclipse measurements. 2. The compact nature of these low

mass white dwarf systems provides a large sample of gravitational wave sources that will be detectable with LISA, which will be sensitive to gravitational wave emission at mHz frequencies ($f_{\rm GW} = 2/P_{\rm orb}$). Similar gravitational wave binaries will be detectable by LISA throughout the Galaxy at distances far beyond the limits of electromagnetic radiation. Thus, a large sample of compact white dwarf binaries may be used to study the structure of the Milky Way (see Korol et al., 2019).

Because, by design, the original ELM Survey was limited to the northern sky, part of this dissertation begins a new survey that aims to find ELM white dwarfs in the southern sky using a variety of techniques, including a similar color selection from SkyMapper and ATLAS photometry and reliable parallax measurements from Gaia, as well as large-scale variability searches in astronomical survey data from ZTF and ASAS-SN. The completed ELM Survey South will, when combined with the northern-sky ELM Survey, provide an all-sky distribution of ELM white dwarfs, which has previously been impossible due to lack of southern-sky photometric surveys. Additionally, formation rates for various WD+WD merger products will be further constrained with the addition of the southern sky white dwarf binaries. With advanced selection techniques, we may be able to include the regions of sky towards the Galactic center and Magellanic clouds that are not significantly affected by extinction, which will help us prepare for dual follow-up observations through standard electromagnetic radiation techniques and gravitational waves, which will be unaffected by the high extinction in these regions of the sky.

1.4 Dissertation overview

This dissertation is broken up as follows. In chapter 2, I present a brief overview of the facilities and instruments used throughout this dissertation. In chapter 3, I present my published follow-up analysis of the low mass, eclipsing, white dwarf binary SDSS J082239.54+304857.19. After obtaining the eclipse-discovery light curve in Brown et al. (2017), I obtained follow-up observations and used the eclipsing light curve together with spectroscopic observations to constrain the orbital inclination and orbital period as well as the radii, temperatures, and masses of the two stars in binary. Additionally, I obtained the first observations towards measuring the orbital decay of the binary due to its emission of gravitational waves. Chapter 3 is a reproduction of my published work in the Monthly Notices of the Royal Astronomical Society (MNRAS) and has been reproduced with permission granted to the first-author by the copyright agreement for use in a doctoral dissertation. The reference to the original work is as follows: Kosakowski, A., Kilic, M., Brown W., MNRAS, Volume 500, Issue 4, February 2021, Pages 5098–5105, (doi: 10.1093/mnras/staa3571).

In chapter 4, I present the first steps towards obtaining a large sample of ELM white dwarfs located in the southern sky through a large, targeted, spectroscopic survey using the SOAR 4.1-meter telescope. Chapter 4 is a reproduction of my published work in the Astrophysical Journal (ApJ) and has been reproduced with permission granted to the authors by the copyright agreement for use in a doctoral dissertation. The reference to the original work is as follows: Kosakowski, A., Kilic, M., Brown W., Gianninas, A., The Astrophysical Journal, Volume 894, Issue 1, id.53, 14 pp. (2020) (doi:

10.3847/1538-4357/ab8300).

In chapter 5, I present the results from my variability search within the public Zwicky Transient Facility data archive through use of the box-least squares algorithm. These analyses are designed to begin the next phase of the ELM Survey South by developing methods for efficiently identifying variable white dwarf binaries within large astronomical survey data and will be applied to future southern-sky surveys such as BlackGEM (Groot et al., 2019) and the Vera Rubin observatory's LSST program.

Finally, I present a summary this dissertation and discuss future work in chapter 6.

Chapter 2

Facilities and Instruments

Much of the results of this dissertation are due to the many nights of on-site and remote observing performed with the Apache Point Observatory 3.5-meter and SOAR 4.1-meter telescopes. Here I present a summary of the facilities and instruments used throughout this dissertation.

2.1 Apache Point Observatory

The Apache Point Observatory (APO) is a collection of telescopes located in Sunspot, New Mexico, USA. The site contains the 0.5-meter Astrophysical Research Consortium Small Aperture Telescope, the New Mexico State University 1.0-meter Telescope, the 2.5-meter Sloan Foundation Telescope, and the Astrophysical Research Consortium 3.5-meter Telescope. My work throughout this dissertation made use of 44 half-nights of observation time using the 3.5-meter telescope with the Agile photometer and Dual-Imaging Spectrograph.

2.1.1 The Agile Photometer

The Agile photometer (Mukadam et al., 2011) is a high-speed CCD photometer used to obtain nearly-continuous, single-filter, exposures of a field without gaps between individual exposures caused by finite CCD data read-out times. Because of this feature, Agile is the ideal instrument for observing systems that display variability on short time-scales, including pulsating white dwarfs, fast rotators, and eclipsing white dwarf

binaries with eclipse durations on the timescale of $\sim$ 60 s. To accomplish this, Agile uses a 1K $\times$ 2K-pixel CCD, with half (1K $\times$ 1K-pixels) actively collecting data while the other half performs the CCD data read-out process between exposures. After an exposure is completed, the data is transferred to the inactive part of the CCD to be read out, allowing a new exposure begin without significant delay caused by the read out process. This method allows nearly-continuous exposures with integrations times as low as the read-out time of the CCD, which is typically 4 s with a standard observing setup, but can be as low as $\approx$ 0.3 s or as high as $\approx$ 10.7 s.

Agile has an unbinned CCD plate scale of 0.130 arcsec pixel^{-1}, which provides a field of view of approximately 2.2 arcmin $\times$ 2.2 arcmin. Because Agile is thermo-electrically cooled to -40° C, it hosts a large dark current, measured at 13.3 e^{-} pixel^{-1} s^{-1} unbinned.

2.1.2 The Dual-Imaging Spectrograph

The Dual-Imaging Spectrograph (DIS) is an optical spectrograph with medium resolving power (R = 1000 – 7000). DIS makes use of a dichroic to split incoming light at $\lambda \approx$ 5350 Angstrom into two beams simultaneously imaged by individual cameras. The blue beam includes the entire Balmer series except for Hα, which allows for efficient white dwarf classification when paired with a low-resolution blue grating (B400; 1.83 Angstrom pixel^{-1}). When paired with the high resolution blue grating (B1200; 0.62 Angstrom pixel^{-1}), DIS becomes a powerful tool to obtain precise measurements of the radial of objects, which manifests itself as small shifts in the central position of the absorption lines in the spectrum. Similarly, when paired with the high resolution red grating (R1200; 0.58 Angstrom pixel^{-1}), precise measurements of magnetic field

strengths may be accomplished through measurements of Zeeman splitting of the Hα line. These measurements may also be used to determine rotation rates of magnetic white dwarfs.

2.2 The Southern Astrophysical Research Telescope

The Southern Astrophysical Research telescope (SOAR) is a 4.1-meter telescope located on Cerro Pachón, Chilé. In addition to the SOAR telescope, the site on Cerro Pachón hosts the Gemini South 8.1-meter telescope and the Vera Rubin Observatory 8.4-meter survey telescope (Ivezić et al., 2019). My research has made use of 27 nights of observation time on the SOAR 4.1-meter telescope with the Goodman high-throughput spectrograph.

2.2.1 The Goodman High-Throughput Spectrograph

The Goodman high-throughput spectrograph (Clemens et al., 2004) allows both photometric imaging and spectroscopy. With an imaging plate scale of $0.15''$ pixel^{-1}, the field of view in imaging mode covers a diameter of $D \approx 7.2$ arcmin over 3096×3096 unbinned pixels. When setup for spectroscopy, the Goodman spectrograph provides wavelength dispersion between $0.12 - 1.00$ Angstrom pixel^{-1} and single-channel wavelength coverage of $3200 - 9000$ Angstrom, depending on the configuration being used. My research exclusively made use of the 930 lines mm^{-1} grating, providing spectral coverage between $3550 - 5250$ Angstrom with wavelength dispersion 0.42 Angstrom pixel^{-1}, which covers the entire Balmer series except Hα and provides measured radial velocity uncertainties $\sigma_v \approx 10$ kms^{-1}.

2.3 Gemini North

Gemini North is an 8.1-meter telescope located on Mauna Kea, Hawai'i, USA. Gemini North is the twin to the Gemini South telescope on Cerro Pachón, Chilé. Together, these two telescopes provide detailed, high-quality data for the entire sky. This dissertation makes use of 209 minutes of observation time using the 'Alopeke photometer on the Gemini North telescope.

2.3.1 'Alopeke

'Alopeke (Scott & Howell, 2018) is a permanently-mounted high-speed photometer attached to the Gemini North telescope. 'Alopeke is a back-illuminated electron-multiplying CCD and, similar to the Agile photometer at APO, uses a high-speed, frame-transfer CCD to allow photometric observations of the same field without any gaps due to read out times. The 'Alopeke CCD is an array of 1024×1024 px with a plate scale of ≈ 0.01 arcsec px^{-1} in speckle mode or ≈ 0.0725 arcsec px^{-1} in wide field mode, resulting in a field of view of 6.7 arcsec or 60 arcsec, respectively. 'Alopeke makes use of a beam-splitter to perform simultaneously two-color imaging, making it ideal for studying eclipsing systems in various filters. Gemini North's twin telescope, Gemini South, makes use of an identical instrument known a Zorro.

Chapter 3

Multi-band light curve analysis of the 40.5-minute period eclipsing double-degenerate binary SDSS J082239.54+304857.19

3.1 Introduction

Eclipsing binary systems provide rare opportunities to directly measure the physical parameters of both of the stars in the system. If the primary and secondary eclipses are both clearly visible, it is possible to test the theoretical mass-radius relationship (Parsons et al., 2017a). Furthermore, with precisely-measured mid-eclipse times, it is also possible to measure the effects of orbital decay due to the loss of orbital angular momentum from gravitational wave emission and torques caused by tidal interaction (Piro, 2011; Benacquista et al., 2011; Fuller et al., 2013).

Even in eclipsing systems where the secondary eclipse is obscured by a significantly brighter primary star, it is still possible to place constraints on the properties of the hidden secondary star by using the information contained within the primary eclipse through light curve fitting. Additional information on these invisible companions can be obtained from radial velocity measurements of the primary star, which provide information on the system's orbital period and mass ratio. Comparing results from light curve fitting with evolutionary models and stellar atmosphere models allows for an independent way to confirm the temperature and radii of both of the stars in the binary system.

As of this work's publication, there are only 14 known eclipsing double-degenerate

systems. With periods ranging from 7 to 354 minutes, these systems are: NLTT 11748 (Steinfadt et al., 2010), CSS 41177 (Drake et al., 2010; Parsons et al., 2011), GALEX J171708.5+675712 (Vennes et al., 2011), J0651+2844 (Brown et al., 2011), J0751−0141 (Kilic et al., 2014a), J1152+0248 (Hallakoun et al., 2016), J0822+3048 (Brown et al., 2017), J1539+5027 (Burdge et al., 2019a), ZTF J1901+5309 (Coughlin et al., 2020), ZTF J0538+1953 (Burdge et al., 2020a), ZTF J2029+1534 (Burdge et al., 2020a), ZTF J0722−1839 (Burdge et al., 2020a), ZTF J1749+0924 (Burdge et al., 2020a), and ZTF J2243+5242 (Burdge et al., 2020b). Here we report on follow-up observation and analysis of the relatively faint ($g_0 = 20.198 \pm 0.023$ mag), 40.5-minute period double-degenerate eclipsing binary system SDSS J082239.54+304857.19 (hereafter: J0822+3048) using the APO 3.5-meter and Gemini North 8.1-meter telescopes.

Originally discovered as a part of an ongoing search for extremely low mass ($M < 0.3$ $M_\odot$) white dwarfs (Brown et al., 2020a; Kosakowski et al., 2020a), J0822+3048 is the seventh eclipsing double white dwarf binary discovered (Brown et al., 2017). In our discovery publication, we used the MMT 6.5-meter telescope with the blue-channel spectrograph to obtain radial velocity measurements of the J0822+3048 system and showed that it contains a $M_A = 0.304 \pm 0.014$ $M_\odot$ DA white dwarf and a degenerate companion with mass $M_B = 0.524 \pm 0.050$ $M_\odot$ on a 40.5 minute orbit. We then obtained 68 minutes of broadband photometry with a blue filter made of Schott BG40 filter glass (BG40 filter, 340 − 600 nm) using the Apache Point Observatory (APO) 3.5-meter telescope frame-transfer camera, Agile (Mukadam et al., 2011), and found two short ($\sim$ 60-second), 0.2 mag deep eclipses in the light curve with a separation consistent with the orbital period obtained through our radial velocity fits. Based on these two eclipses,

we placed weak constraints on the absolute radii of the stars in the system.

In this work, we expanded upon our discovery data with an additional 492 minutes of APO BG40 broadband filter data spread across two additional observing epochs for a total BG40 filter baseline of over 318 days, as well as 209 minutes of simultaneous r-band and i-band filter data from the 8.1-meter Gemini North telescope using the high-speed camera, 'Alopeke (Scott & Howell, 2018). We use these data to further constrain the component radii, orbital inclination, and mid-eclipse timing of the system.

This paper is organized as follows. In section 2, we present the observations and discuss the data reduction steps used to create our final light curves. In section 3 we discuss our data analysis methods, and in section 4 we discuss our results on the binary system parameters and conclude.

3.2 Observations and Data Reduction

3.2.1 Apache Point Observatory

Our eclipse discovery data for J0822+3048 was obtained on UT 2017 March 02 using the 3.5-meter telescope at the Apache Point Observatory (APO) with the BG40 broadband filter on the Agile frame-transfer camera (Mukadam et al., 2011) exposing for 68 minutes with 30-second back-to-back exposures. Due to the short duration of the eclipses, this discovery dataset captured two primary eclipses, each containing only two data points.

We obtained follow-up data on UT 2017 November 16 and UT 2018 January 14 using an identical setup to the discovery data with 30-second exposures. Our first night of follow-up observations spanned 322 minutes. We excluded the final 81 minutes of data

due to cloud coverage significantly affecting the light curve. The remaining 241 minutes includes six primary eclipses. Our second night of follow-up observations spanned 251 minutes and covers six primary eclipses. One of these eclipses is lost due to instrument problems. Figure 3.1 shows our calibrated light curves for our BG40 datasets. Our best-fitting model from our Monte Carlo light curve fits to the APO BG40 data (discussed below) is overplotted as a solid red line.

3.2.2 Gemini North

We supplemented the APO BG40 broadband filter data with simultaneous r- and i-band observations using the dual-channel frame-transfer camera, 'Alopeke (Scott & Howell, 2018) on the 8.1-meter Gemini North telescope. The observations were taken in eight, nearly back-to-back, observing blocks each containing 100 back-to-back 15-second exposures on UT 2019 March 12 as a part of the program GN-2019A-Q-119 (PI: Kosakowski). These observations spanned 209 minutes and included five primary eclipses. Cloud coverage affected the quality of the data about two hours into the observations. Unfortunately, due to an issue with the GPS timing synchronization between the telescope and the 'Alopeke instrument at the time of observation, our Gemini data is systematically shifted by about -21 seconds. We note that the relative frame timing is unaffected by this systematic shift. Figure 3.2 shows our calibrated Gemini r-band (top) and i-band (bottom) light curves. Our best-fitting model from our Monte Carlo light curve fits to the Gemini r-band and i-band data (discussed below) are overplotted as solid red lines.

3.2.3 Data Reduction

We used the IRAF package CCDRED to perform image reduction using a set of bias images, dark images, and twilight flats, each taken on the same nights as our observations. We performed relative aperture photometry using the IRAF package DAOPHOT using a circular source aperture with radius based on the FWHM of each image and a background annulus surrounding each source aperture. For our APO Agile data, we used two nearby, relatively bright, nonvariable field stars to calibrate the resulting light curve. For our Gemini 'Alopeke data, because the 'Alopeke instrument has a much smaller field of view than Agile, we only had three nearby, non-variable, field stars of similar brightness available to calibrate our target light curve. We detrended each light curve by fitting and subtracting a third-order polynomial. Finally, we converted our APO data timing system from beginning-of-exposure TAI to middle-of-exposure Barycentric Dynamical Time (BJD_TDB; Eastman et al. (2010) and our Gemini data timing from end-of-exposure TAI to middle-of-exposure BJD_TDB.

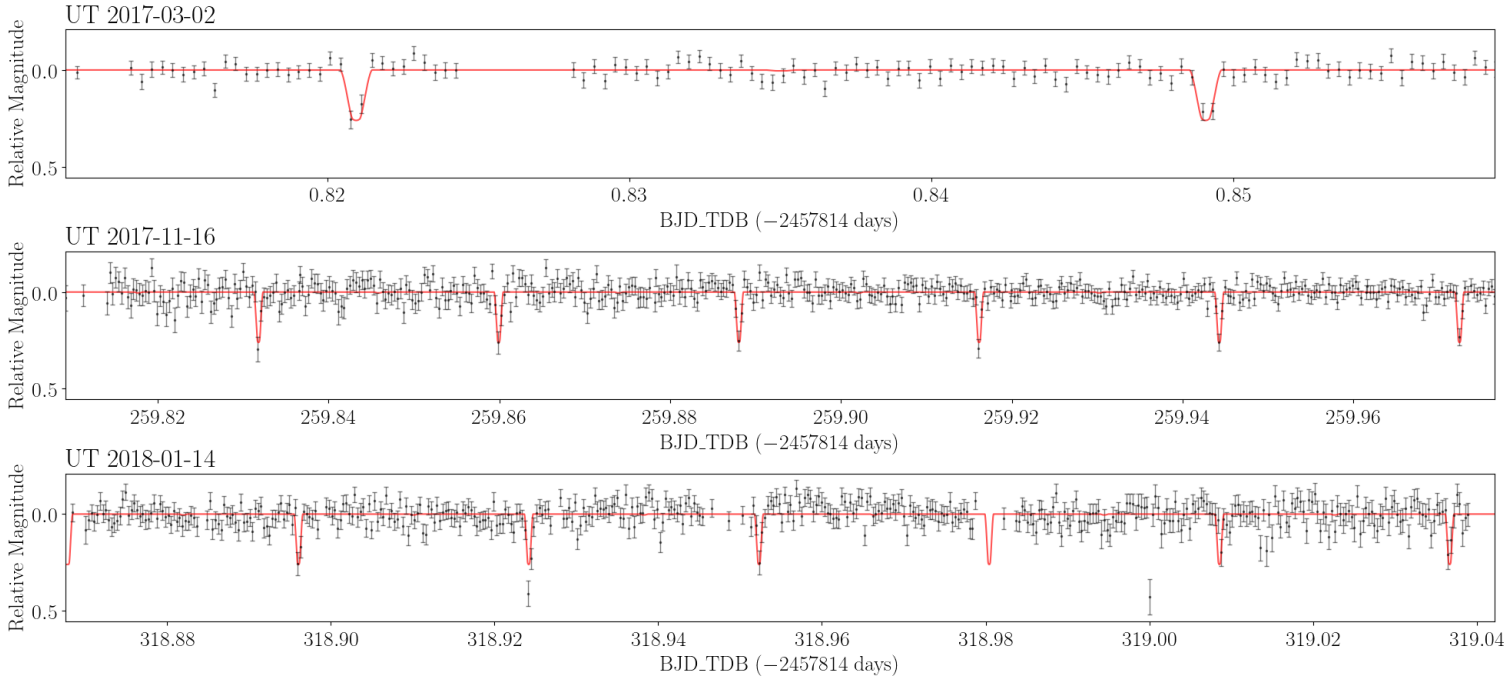

Fig. 3.1.— Calibrated light curves for APO BG40 broadband from UT 2017 March 02 (top), UT 2017 November 16 (middle), and UT 2018 January 14 (bottom). The best-fit model based on light curve fitting to the combined APO data with JKTEBOP discussed in the text is overplotted in red.

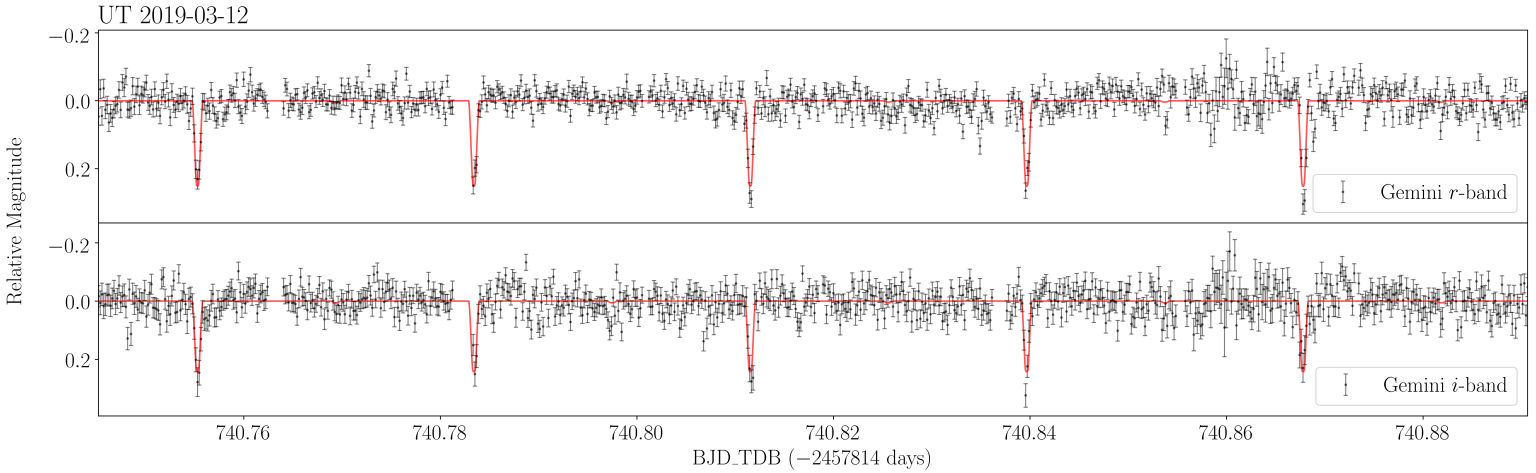

Fig. 3.2.— Calibrated light curves for Gemini r-band (top) and i-band (bottom) filters obtained simultaenously on UT 2019 March 12. The best-fit model based on light curve fitting with JKTEBOP discussed in the text is overplotted in red. The timing shown is as recorded by the 'Alopeke instrument and is systematically offset by about 21 seconds due to an instrument problem discussed in the text.

3.3 Initial Period Determination

The orbital period of the J0822+3048 system was originally determined using radial velocity measurements based on the Balmer lines in the optical spectrum and roughly confirmed through light curve fitting of the discovery light curve containing two adjacent primary eclipses. We combined our new APO BG40 broadband data with the discovery dataset to create a master light curve spanning just over 318 days and containing 13 primary eclipse measurements. We used this master light curve to perform light curve fitting and to precisely determine the orbital period of the J0822+3048 system.

Since the periods obtained through radial velocity measurements and the eclipsing light curve of the discovery dataset are only roughly consistent, to obtain an appropriate initial period estimate for light curve fitting, we used the AstroPy implementation of the Lomb-Scargle periodogram to create a power spectrum from all of the combined APO BG40 data using simple models with varying numbers of sine-terms. We limited our period range to search between 40 and 41 minutes with a step size of about 1 ms. Our Lomb Scargle models each returned an identical best-fit frequency at 35.55448746 cycles d^{-1}. While we do not estimate uncertainties on this initial measurement, this frequency is only 0.0002 cycles d^{-1} ($\approx$ 0.01 s) greater than the original frequency obtained using radial velocity observations of 35.55429140 cycles d^{-1}. We used this period as our initial value when performing light curve fitting discussed in the next section.

3.4 System Parameters - Light Curve Fitting

3.4.1 APO BG40 Broadband fits

We modeled the system parameters using JKTEBOP (Southworth et al., 2013), which uses Levenberg-Marquardt minimization to obtain best-fit parameter values. For the BG40 dataset, we fitted for the sum and ratio of the fractional system component radii ($r = R/a$), inclination angle, stellar light ratio, and orbital period. We chose to fix the mass ratio and initialized these parameters based on values taken from the discovery paper, with exceptions for the orbital period, which we initialized based on our previous Lomb-Scargle estimate.

We used a 4-parameter limb darkening law with coefficients for a $T_{\rm eff} = 14,000$ K, $\log g = 7.14$ He core white dwarf primary star and $T_{\rm eff} = 5,000$ K, $\log g = 8.00$ C/O core white dwarf secondary star. Due to technical limitations in the JKTEBOP software restricting limb darkening values to be greater than -1.0, we used the limb-darkening coefficients of Gianninas et al. (2013) for the LSST u-, g-, r-, and i-band filters and converted these to the BG40 broadband filter system using equation 3 of Hallakoun et al. (2016). The Gianninas et al. (2013) intensity functions are in good agreement with the updated Claret et al. (2020) intensity functions so we expected this substitution to have minimal effect on our results. Similarly, we used fixed gravity darkening coefficients from Claret et al. (2020) for the u-, g-, r-, and i-band filters and once again converted these to the BG40 system using equation 3 in Hallakoun et al. (2016). The best-fitting models for our APO BG40 and Gemini r-band and i-band fits are overplotted onto the calibrated light curve data and shown in Figures 3.1 and 3.2, respectively.

We used JKTEBOP's Monte Carlo analysis to create parameter distributions and estimate uncertainties for each of our fitted parameters. This is done by creating a simulated light curve based on Gaussian perturbations to the best-fit model light curve and performing Levenberg-Marquardt minimization to the simulated light curve. Details for this Monte Carlo analysis method can be found in Southworth et al. (2004) and Southworth et al. (2005). We performed 15,000 of these Monte Carlo fits to the combined BG40 master light curve and filtered out results that converged to unphysical values, such as inclination angles $i < 80^{\circ}$ that would not show eclipses in this system. After filtering, we were left with over 13,600 successful fits from which we created the resulting parameter distributions. Figure 3.3 shows the final parameter distributions for our APO BG40 light curve fits. The diagonal shows the 1-D histograms with a 1-D Gaussian Kernel Density Estimate (KDE) overplotted as a blue-shaded distribution. We marked the locations of the median fit and the 1σ range of the data if the distribution is single-peaked. Because our 30-second exposures poorly sample the short primary eclipses, and because our light curves do not show a clear secondary eclipses, the secondary star's radius and the system's inclination are not well-constrained to a single best value and are strongly anti-correlated. For these double-peaked distributions, we fitted a Gaussian to each peak separately and report the resulting central value and width of each Gaussian as the 'best' fits. We overplotted these best fits and their 1σ range as red and blue vertical lines on top of their respective peaks. Best-fit values for each parameter are reported above each histogram. The off-diagonal plots show 2-D distributions of each Monte Carlo fit with individual results marked as black points and 2-D Gaussian KDE overplotted as colored contours.

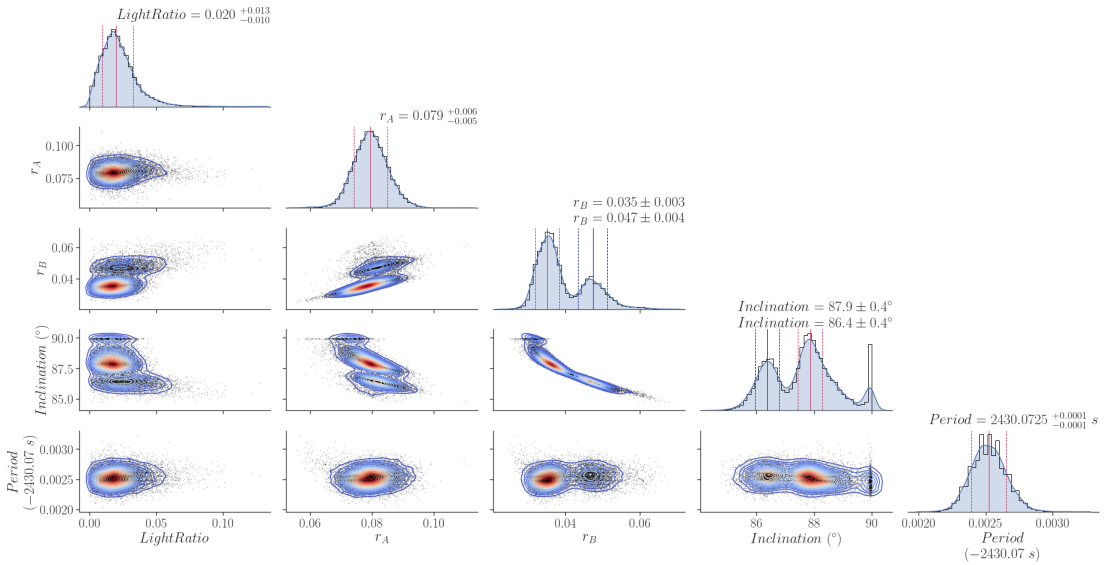

Fig. 3.3.— Parameter distributions from Monte Carlo fits to the combined APO BG40 broadband light curve. The diagonal contains the 1-D parameter distributions split into 40 bins (black histogram) with a 1-D Gaussian KDE overplotted as a blue shaded distribution. The off-diagonal plots contain the 2-D parameter distributions with 2-D Gaussian KDE contours overplotted. Primary/Secondary median fits and 1σ ranges are marked with vertical red/blue lines for single/double-peaked distributions. Due to the poorly constrained light ratio and lack of visible secondary eclipses in the light curve, the secondary star's radius and the system's inclination are not well-constrained to a single peak and are strongly anti-correlated.

3.4.2 Gemini r-band & i-band fits

For our Gemini r-band and i-band fits, we performed 15,000 Monte Carlo simulations fitting for sum and ratio of the fractional system component radii, inclination, and light ratio. We initialized the parameters based on the best-fitting parameters from the APO BG40 data. We chose to fix the period at the best-fit result from the BG40 data fit due to the much longer baseline of the APO data. Our Gemini r-band and i-band parameter distributions can be seen in Figures 3.4 and 3.5 and follow the same organization as Figure 3.3.

While all peak values agree within their respective 1σ ranges across each filter, we note that the large temperature difference between the primary and secondary stars resulted in a 3σ detection of the cooler secondary star in the system's light ratio for the redder Gemini r- and i-band filters. This increased significance allowed the Gemini fits to strongly favor one peak over another, essentially breaking the degeneracy between the system's inclination and the secondary star's fractional radius. Best-fit parameters and their uncertainties for all filters are presented in Table 3.1, along with their variance-weighted mean values. We calculated absolute radius values based on our light curve fitting using the orbital separation $a = 0.364 \pm 0.008$ $R_\odot$ from the discovery publication. Figure 3.6 shows the resulting phase-folded light curves using the period from our APO BG40 dataset fits. We overplot the best-fit models created from the best-fit parameters in Table 3.1 as a solid red line and zoom in to the regions surrounding the primary and secondary eclipses.

Table 3.1: Best-fit parameters from the APO BG40 broadband and Gemini r-band and i-band datasets. Peak values for double-peaked distributions are reported together. Preferred solutions to the double-peaked parameters are presented in a bold font for clarity. We include the variance-weighted mean values across all filters for each parameter.

Parameter	BG40 broadband	r-band	i-band	Mean Value
Light Ratio	$0.020^{+0.013}_{-0.010}$	$0.016^{+0.006}_{-0.005}$	$0.027^{+0.010}_{-0.009}$	
$r_B + r_A$	$0.118^{+0.013}_{-0.010}$	$0.128^{+0.008}_{-0.007}$	$0.122^{+0.011}_{-0.009}$	0.124±0.005
r_B/r_A	**0.449±0.015**	**0.445±0.010**	**0.439±0.014**	**0.444±0.007**
	0.573±0.027	0.565±0.026	0.572±0.029	0.570±0.016
i (°)	**87.9±0.4**	**87.5±0.4**	**87.7±0.5**	**87.7±0.2**
	86.4±0.4	86.0±0.3	86.0±0.4	86.0±0.2
Period (min)	40.501209± (2×10^{-6})			
R_A ($R_\odot$)	0.029±0.010	0.032 ± 0.009	0.031 ± 0.010	0.031±0.006
R_B ($R_\odot$)	**0.013±0.009**	**0.014±0.008**	**0.013±0.008**	**0.013±0.005**
	0.017±0.009	0.018 ± 0.009	0.018 ± 0.009	0.018±0.005

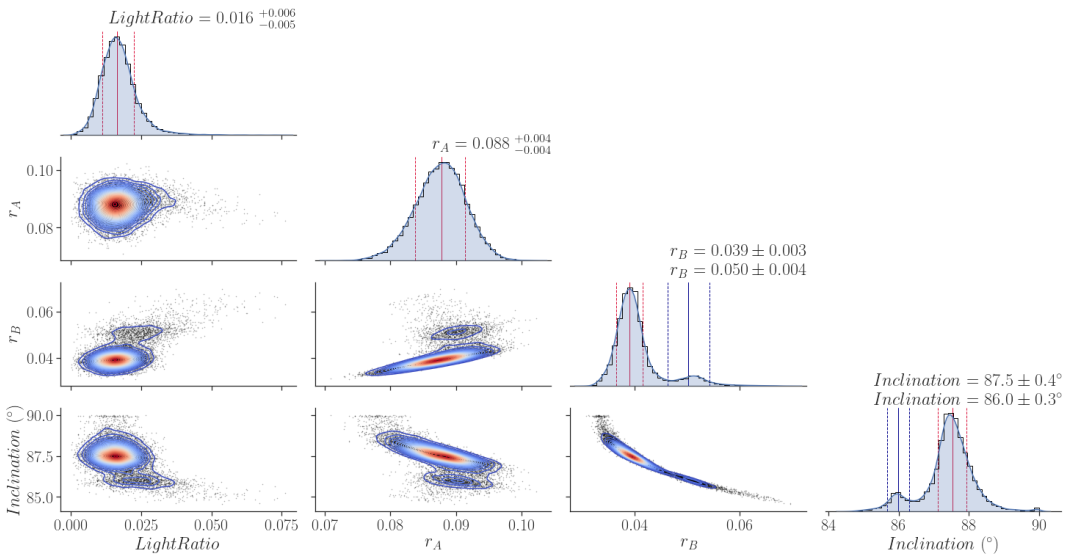

Fig. 3.4.— Parameter distributions from Monte Carlo fits to the Gemini r-band light curve. The diagonal contains the 1-D parameter distribution split into 40 bins (black histogram) with a 1-D Gaussian KDE overplotted as a blue shaded distribution. The off-diagonal plots contain the 2-D parameter distributions with 2-D Gaussian KDE contours overplotted. Primary/Secondary median fits and 1σ ranges are marked with vertical red/blue lines for single/double-peaked distributions.

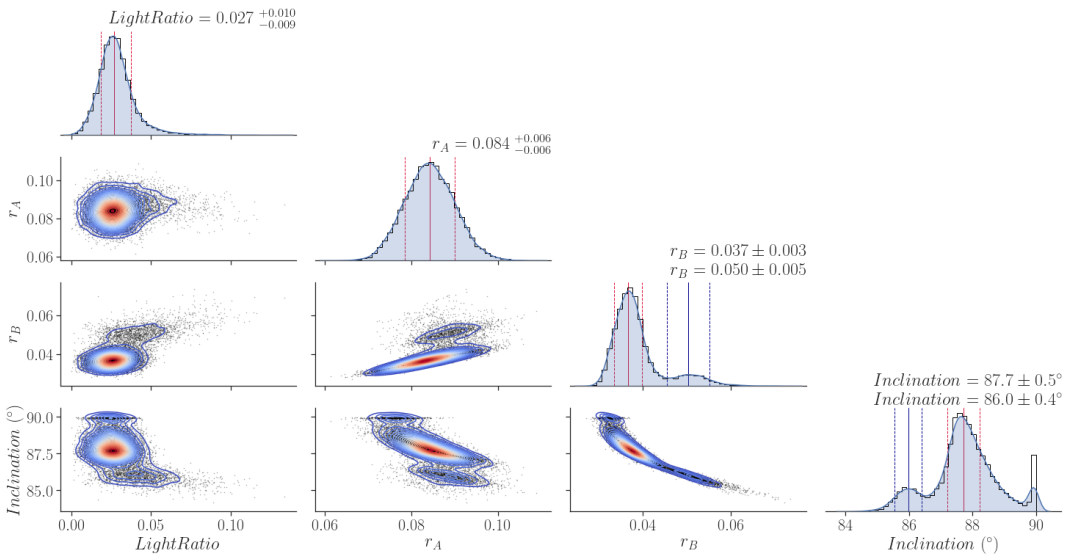

Fig. 3.5.— Parameter distributions from Monte Carlo fits to the Gemini i-band light curve. The diagonal contains the 1-D parameter distribution split into 40 bins (black histogram) with a 1-D Gaussian KDE overplotted as a blue shaded distribution. The off-diagonal plots contain the 2-D parameter distributions with 2-D Gaussian KDE contours overplotted. Primary/Secondary median fits and 1σ ranges are marked with vertical red/blue lines for single/double-peaked distributions.

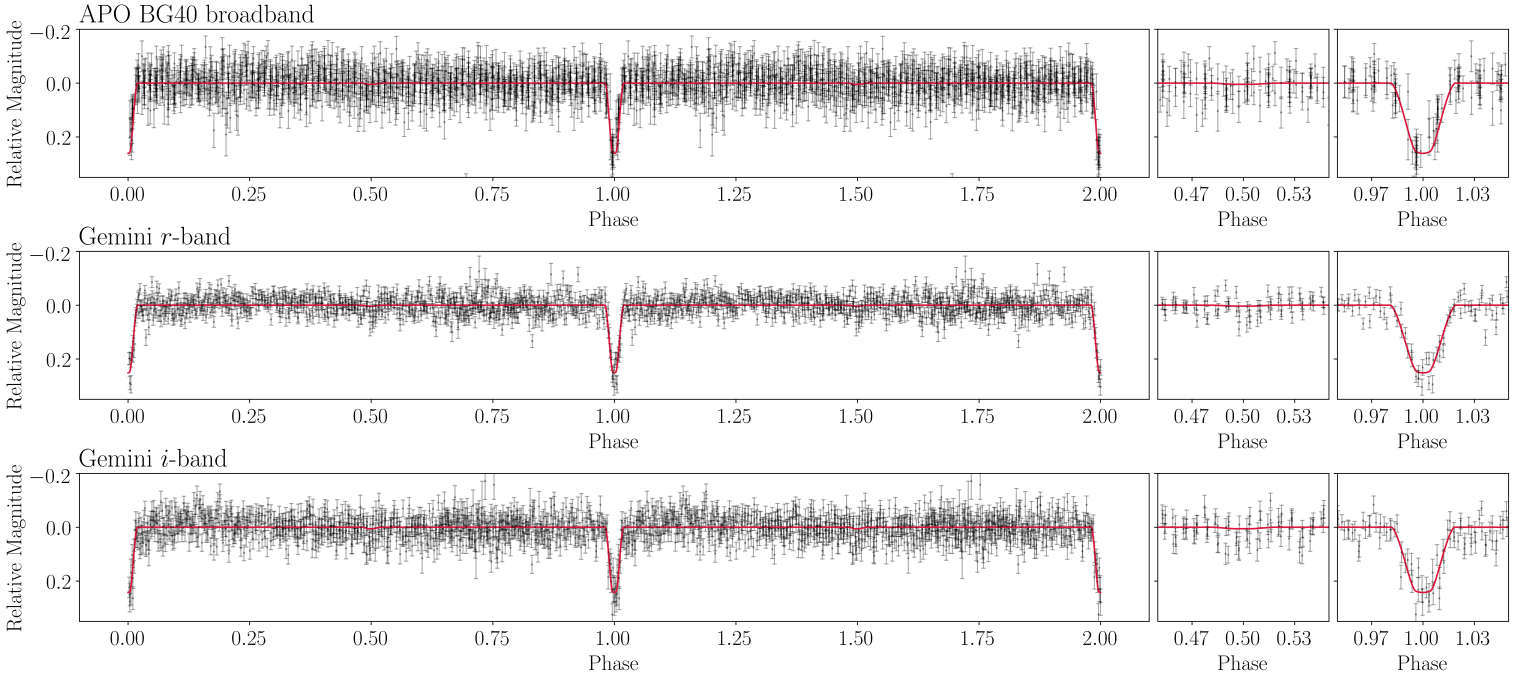

Fig. 3.6.— Phase-folded light curves for APO BG40 broadband (top), Gemini r-band (middle), and Gemini i-band (bottom). Best-fit models based on JKTEBOP Monte Carlo results are overplotted in red. Zoomed-in plots surrounding the primary and secondary eclipses are included for each filter. The secondary eclipse is not seen in any filter.

3.5 Estimating Effective Temperature and Radius of the Secondary Star

3.5.1 Temperature Estimate

We used the best-fitting parameters from our light curve fitting to estimate the effective temperature of the secondary star. We first calculated the system's absolute magnitude using the extinction-corrected SDSS apparent magnitudes and the distance from the discovery data obtained through spectroscopic models. We then interpolated over the C/O core DA white dwarf cooling models of Tremblay et al. (2011a)[1] to a mass of $M_B = 0.524\,\mathrm{M}_\odot$. Our interpolation resulted in effective temperatures $T_{\mathrm{eff},r} = 5210 \pm 150$ K and $T_{\mathrm{eff},i} = 5180 \pm 120$ K for the r-band and i-band, respectively. We took the variance-weighted mean of these results and accepted $T_{\mathrm{eff}} = 5200 \pm 100$ K as the secondary white dwarf's effective temperature.

3.5.2 Radius Estimates

Between our light curve fitting results across three filters, the component radii for the J0822+3048 system are fairly-well constrained to a single solution. Here we compare our results to evolutionary model predictions for an $M = 0.304 \pm 0.014\,\mathrm{M}_\odot$ He core primary white dwarf and $M = 0.524 \pm 0.050\,\mathrm{M}_\odot$ C/O core secondary white dwarf.

For the primary white dwarf, we interpolated over the He core white dwarf evolutionary tracks of Istrate et al. (2016), including elemental diffusion and stellar rotation, and obtain a primary radius of $R_A = 0.025 \pm 0.001\,\mathrm{R}_\odot$. This value roughly agrees within 1σ of our

[1] http://www.astro.umontreal.ca/~bergeron/CoolingModels

estimate from the light curve fitting of $R_A = 0.031 \pm 0.006$ R$_\odot$.

For the secondary star, we interpolated over the evolutionary models for C/O core composition, thick hydrogen layer ($q_H = 10^{-4}$), white dwarfs Fontaine et al. (2001). This interpolation resulted in a radius estimate of $R_B = 0.014 \pm 0.001$ R$_\odot$. This is in excellent agreement with our estimate from light curve fitting of $R_B = 0.013 \pm 0.005$ R$_\odot$. Our light curve fitting results agree well with the mass-radius relation for white dwarfs and confirms that our Gemini r- and i-band fit results have identified the correct peak where our APO BG40 fit failed. In addition, because the secondary star's radius and the system's inclination were strongly anti-correlated, we are now also able to select the correct inclination peak at $i = 87.9 \pm 0.4°$ in our APO BG40 distribution.

3.6 Eclipsing Timing Estimate and Orbital Decay

The orbit of compact double-degenerate systems decays due to the loss of angular momentum (Landau & Lifshitz, 1958). While gravitational waves are generally the dominant source of angular momentum loss in these compact systems, torques caused by strong tidal interaction between the stars in compact systems may also contribute significantly to the total angular momentum loss (Piro, 2011; Benacquista et al., 2011; Fuller et al., 2013). Eclipse timing measurements taken over long baselines have been used as a method to directly measure the effects of orbital decay in these systems.

In the case of the 12-minute period eclipsing double-degenerate binary J0651+2844 (Brown et al., 2011), Hermes et al. (2012) measured the system's mid-eclipse timing over a baseline of 13 months and showed that the period of the system is decaying at a rate

of $\dot{P} = (-9.8 \pm 2.8) \times 10^{-12}$ s s^{-1}. The authors showed that, while the system shows evidence for tidal interaction in its ellipsoidal variations, a longer baseline is required to measure the orbital decay contribution from the tidal interaction in the system.

Similarly, Burdge et al. (2019a) have used new and archival data to perform mid-eclipse timing measurements of the 7-minute period eclipsing double-degenerate binary J1539+5027. They precisely measured the system's orbital decay with a 10 year baseline and showed that the orbital decay is consistent with constant change in period $\dot{P} = (-2.373 \pm 0.005) \times 10^{-11}$ s s^{-1}. Additionally, Burdge et al. (2019c) have identified a 20-minute non-eclipsing double-degenerate binary system showing strong ellipsoidal variation caused by tidal distortions. They used these ellipsoidal variations to measure the orbital decay of the system caused by gravitational wave emission and estimated the contribution to the decay from tidal effects. Finally, Burdge et al. (2020b) have identified an 8.8-minute period eclipsing double-degenerate binary system using ZTF archival data and show that the system is undergoing rapid orbital decay. They estimated that tidal effects could contribute as much as 7.5 percent to the orbital decay of the system.

We measured the time of mid-eclipse for each of our APO epochs to prepare for future orbital decay studies of the J0822+3048 system. Because of the systematic offset in the timing of our Gemini data, we estimated the mid-eclipse time only for the three epochs of APO BG40 data. For each epoch of data, we performed 50,000 Monte Carlo fits using JKTEBOP to fit the light curves for only the mid-eclipse time, using the best-fit parameters in Table 3.1 as initial parameters.

We used the time of ingress and egress from the best-fit model light curve to estimate the eclipse duration as $T_{eclipse} \approx 90$ seconds, with minimum light lasting ≈ 20 seconds. We therefore excluded results with mid-eclipse timing greater than 45 seconds from the median fit value, as those results place the middle of the eclipse outside of the observed range of the eclipse itself. Figure 3.7 shows the resulting distribution for each epoch of data. We fit a Gaussian to the central peak of each distribution and report the central value and width as the best-fit and 1σ uncertainty. These values are reported in Table 3.2. We calculated the offset of each observed mid-eclipse time from its expected value by measuring the eclipse timing offset from a linear projection based on the first epoch's time of eclipse and the orbital period of the system. We note that in our second and third APO BG40 data sets, the measured mid-eclipse timings are +3.0 and +2.9 seconds off of the expected time assuming no orbital decay, but each agree within the relatively large ± 4.3 seconds 1σ range on the discovery dataset's mid-eclipse timing.

Despite not recording a significant offset in the measured mid-eclipse timing, we revisited the decay of mid-eclipse timing due to gravitational waves using the two new epochs of APO data discussed in this work. Figure 3.8 shows an $(O - C)$ diagram with the best-fit mid-eclipse timing measurements to our two new epochs of APO BG40 data (black data points with error bars) plotted as an offset from the expected mid-eclipse timing assuming no orbital decay (black dashed line) with a period $P = 0.0281258394$ d. We exclude the discovery data set due to its relatively large uncertainties. We plot the projected offsets in mid-eclipse timing out to the expected launch date of the LISA mission in 2034, based on angular momentum loss solely due to the emission of gravitational waves (Piro, 2011) as a red dashed line with shaded 1σ region dominated by the uncertainties

Table 3.2: Best-fit mid-eclipse times (barycentric dynamical time) for the APO BG40 broadband data.

T_0 (BJD_TDB)
2457814.82095 ± 0.00005
2458073.88809 ± 0.00002
2458132.89610 ± 0.00003

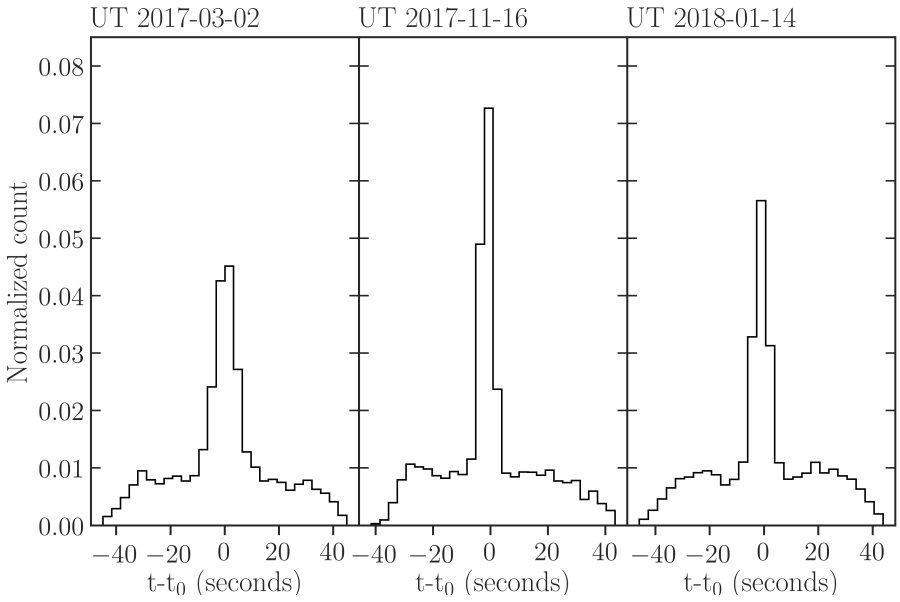

Fig. 3.7.— Mid-eclipse timing distributions from 50,000 Monte Carlo fits to each of the three APO BG40 broadband light curves. Fits that converged greater than 45 seconds from the median were excluded as unphysical.

in the masses of each star in the system. We used these projected values and the mean uncertainty in our measured values with 30-second exposure times and calculate that a 3σ significant mid-eclipse timing offset measurement will be possible in the year 2023, at which point the J0822+3048 system will eclipse 8.4 ± 0.7 seconds earlier than expected as measured from our second APO epoch.

3.7 Conclusions

We have expanded upon the discovery APO BG40 light curve of J0822+3048 with an additional 492 minutes of APO BG40 data and 209 minutes of simultaneous Gemini r-band and i-band data. We analyzed these light curves and improved the estimates for the absolute radii of both stars in the system using a combination of light curve fitting and white dwarf evolutionary models. Our fits resulted in variance-weighted mean component radii values of $R_A = 0.031 \pm 0.006$ R$_\odot$, $R_B = 0.013 \pm 0.005$ R$_\odot$, and system inclination $i = 87.7 \pm 0.2°$. In addition, we use the results from light curve fitting together with white dwarf cooling models to estimate the secondary white dwarf's effective temperature at $T_{\rm eff} = 5200 \pm 100$ K.

Finally, we have reported an accurate and precise orbital period for this system and measured mid-eclipse times for each epoch of APO data for use with future eclipsing timing variability studies. We show that, with 30-second exposures, a 3σ significant mid-eclipse offset measurement will be possible during the year 2023, at which point the mid-eclipse time will be offset by -8.4 ± 0.7 seconds due to the loss of angular moment from the emission of gravitational waves. With the expected launch of the LISA mission in 2034, we predict that J0822+3048 will show an 83.7 ± 7.3 s offset in mid-eclipse timing by the time LISA launches. While J0822+3048 falls just below the LISA 4-year sensitivity curve with a signal-to-noise ratio of $S/N \approx 3.6$, with its precise period and sky position known, a gravitational wave detection may be possible.

While we have placed constraints on the parameters of the stars in the system, there is still room for improvement. Higher-quality data may provide the first direct detection of

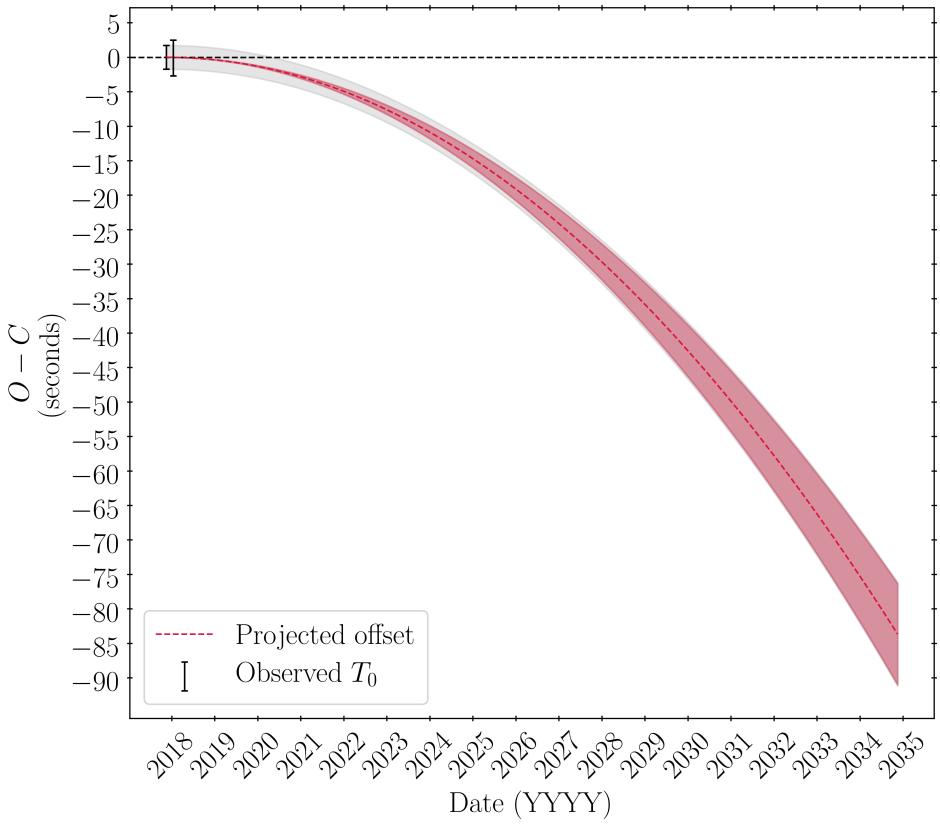

Fig. 3.8.— Best-fit mid-eclipse timing measurements for J0822+3048 for our two new epochs of APO data discussed in the text plotted as offsets to the expected mid-eclipse timing, in seconds, based on the period of $P = 0.0281258394$d determined through light curve fitting. We include the projected offsets based on Piro (2011) estimates of angular momentum loss solely due to gravitational wave emission as a function of time as a red dashed line with a shaded 1σ range up to the expected launch date of the LISA mission in 2034. The dark grey shaded region represents the projected offset from gravitational wave emission, but also includes uncertainty in our initial time of eclipse measurement added in quadrature.

the secondary eclipse, allowing for absolute measurements on the secondary's radius and temperature. Additionally, reduced exposure times will allow for increased significance in future orbital decay measurements and are therefore also desired.

Acknowledgements

This work was supported in part by the NSF under grant AST-1906379. This research is based in part on observations obtained with the Apache Point Observatory 3.5-meter telescope, which is owned and operated by the Astrophysical Research Consortium

Some of the Observations in the paper made use of the High-Resolution Imaging instrument(s) 'Alopeke. 'Alopeke was funded by the NASA Exoplanet Exploration Program and built at the NASA Ames Research Center by Steve B. Howell, Nic Scott, Elliott P. Horch, and Emmett Quigley. 'Alopeke was mounted on the Gemini North telescope of the international Gemini Observatory, a program of NSF's NOIRLab, which is managed by the Association of Universities for Research in Astronomy (AURA) under a cooperative agreement with the National Science Foundation. on behalf of the Gemini partnership: the National Science Foundation (United States), National Research Council (Canada), Agencia Nacional de Investigación y Desarrollo (Chile), Ministerio de Ciencia, Tecnología e Innovación (Argentina), Ministério da Ciência, Tecnologia, Inovações e Comunicações (Brazil), and Korea Astronomy and Space Science Institute (Republic of Korea).

This research made use of Astropy,[2] a community-developed core Python package for Astronomy (Astropy Collaboration et al., 2013, 2018).

[2]http://www.astropy.org

Chapter 4

The ELM Survey South. An Effective Search for Extremely Low Mass White Dwarfs

4.1 Introduction

The single-star evolution of a solar-metallicity main sequence star with mass below about 8 $M_\odot$ typically results in the formation of a CO-core white dwarf with mass of around 0.6 $M_\odot$ or an ONe-core white dwarf with mass of $M_{\rm ONe} > 1.05$ $M_\odot$ (Woosley & Heger, 2015; Lauffer et al., 2018). The formation of low mass He-core white dwarfs ($M < 0.5$ $M_\odot$) requires that the progenitor loses a significant amount of mass while on the red giant branch. This mass loss can occur in metal-rich single-stars (Kilic et al., 2007) or in close binary systems, in which the companion strips the low-mass white dwarf progenitor of its outer envelope before it begins Helium burning. However, because the nuclear burning lifetime of single stars that would form Extremely Low Mass ($M < 0.3$ $M_\odot$; ELM) white dwarfs is longer than a Hubble time, these systems must form through binary interaction.

Previous surveys targeting ELM white dwarfs have taken advantage of the abundance of photometric measurements of the northern sky to select candidate systems for follow-up observations. At the conclusion of the ELM Survey, Brown et al. (2020b) had identified 98 double-degenerate white dwarf binary systems through careful photometric cuts in SDSS photometry, which account for over half of the known double-degenerate systems in the Galaxy. With almost all of the currently known ELM systems located in the northern sky, we begin the search for ELM systems in the southern sky with two different target

selection methods based on ATLAS, SkyMapper, and Gaia photometry.

The layout of this paper is as follows. In section 2, we begin by discussing our ATLAS+SkyMapper color target selection method and observations. We discuss results and briefly comment on the detection efficiency. In section 3, we discuss our Gaia parallax target selection method and discuss the results and efficiency. Finally, we summarize our conclusions in section 4.

4.2 A Survey Based on ATLAS and SkyMapper Colors

The ELM Survey has been successful at identifying a large number of double white dwarfs based on the Sloan Digital Sky Survey (SDSS) photometry. The $u-g$ and $g-r$ colors are excellent indicators of surface gravity and temperature, respectively. With the availability of the $u-$band data from the VST ATLAS and SkyMapper surveys in the southern sky, we based our target selection on color cuts to the VST ATLAS Data Release 2 and Data Release 3 (Shanks et al., 2015) and SkyMapper Data Release 1 (Wolf et al., 2018).

4.2.1 ATLAS Color Selection

VST ATLAS is a southern sky survey designed to image 4,500 deg^2 of the southern sky at high galactic latitudes in the SDSS $ugriz$ filter set with similar limiting magnitude to SDSS ($r \sim 22$). With the release of DR3 in March 2017, each filter has a total southern sky coverage of $\approx 3,000-3,700$ deg^2.

We constructed our color cuts based on the results of the previous ELM white dwarf (Brown et al., 2016a) and Hypervelocity Star (Brown et al., 2014) surveys. We defined

our color cuts to include the region of color-space including late-B type hypervelocity star candidates, which coincidentally overlaps with the low-mass white dwarf evolutionary tracks. Figure 4.1 shows our color selection region.

To construct our VST ATLAS DR2+DR3 sample, we first de-reddened and converted the native ATLAS colors into SDSS (u_0, g_0, r_0, and i_0) using reddening values of Schlegel, Finkbeiner, & Davis (1998) and color conversion equations of Shanks et al. (2015). We exclude targets located along the line of sight to the Galactic bulge and restricted target g_0 magnitude to $15 \leq g_0 < 20$. We remove quasars from the list by imposing a cut on $r - i$, and limit our sample to objects with $11,000\ \mathrm{K} \lesssim T_{\mathrm{eff}} \lesssim 22,000\ \mathrm{K}$ by imposing a $g - r$ color cut. While our temperature limits are chosen to avoid contamination from sdA and sdB stars, which are generally found outside of this temperature range, such a temperature cut introduces a selection bias against ELM white dwarf systems that form through stable Roche lobe overflow (Li et al., 2019). Our exact photometric cuts are defined by

$$15 \leq g_0 < 20$$

$$-0.42 < (g-r)_0 < -0.2$$

$$(r-i)_0 < -0.05$$

$$(u-g)_0 < 1.15$$

$$(u-g)_0 < -2.67(g-r)_0 + 0.25 \;||\; (u-g)_0 < 0.97$$

$$(u-g)_0 > 2.0(g-r)_0 + 1.21 \;||\; (u-g)_0 > 0.65$$

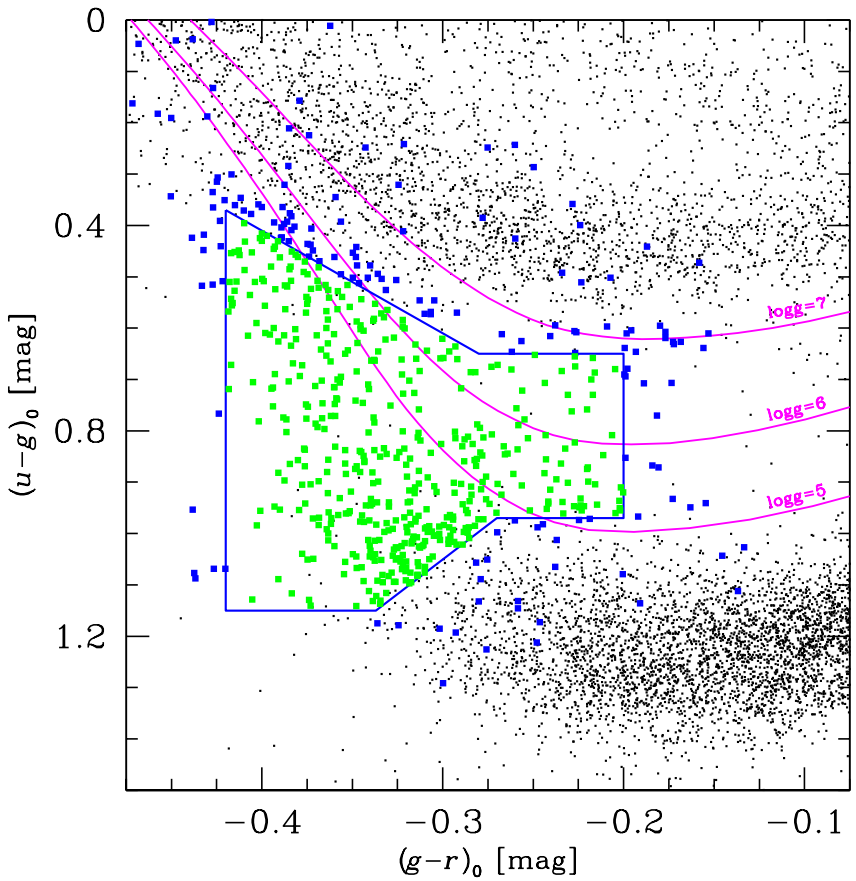

Fig. 4.1.— Target selection region for the VST ATLAS data set as described in the text. The colored dots mark every ATLAS object with $15 < g_0 < 20$ mag and with a follow-up spectrum (green points satisfy the target selection region shown in blue bounds, and blue points are outside of our final target list), black dots are all other objects in ATLAS, restricted to $17.5 < g < 19.5$ mag for sake of clarity. We overplot the DA white dwarf cooling tracks for log g=5, 6, and 7 as magenta lines. Excluding objects visually identified as "bad" (close doubles, objects in globular clusters, etc.), our spectroscopic follow-up is 89% complete in the range $16 < g_0 < 20$ mag.

4.2.2 SkyMapper Color Selection

SkyMapper is a southern sky survey designed to image the entire southern sky in the $uvgriz$ filter set. SkyMapper DR1, released June 2017, provides data on over 20,000 deg^2 of the southern sky, with approximately 17,200 deg^2 covered by all six filters. SkyMapper DR1 is a shallow survey with limiting magnitude around 17.75 for each filter.

From the SkyMapper DR1 dataset, we selected all objects with $E(B-V) < 0.1$ and stellarity index `class_star` > 0.67, where `class_star` $= 1.0$ represents a star. We then removed targets along the line of sight of the Galactic Bulge and the Large and Small Magellanic Clouds. Finally, we de-reddened and applied the following color cuts in the native SkyMapper $uvgriz$ system (Bessell et al., 2011) to create a clean sample. Figure 4.2 shows our target selection region.

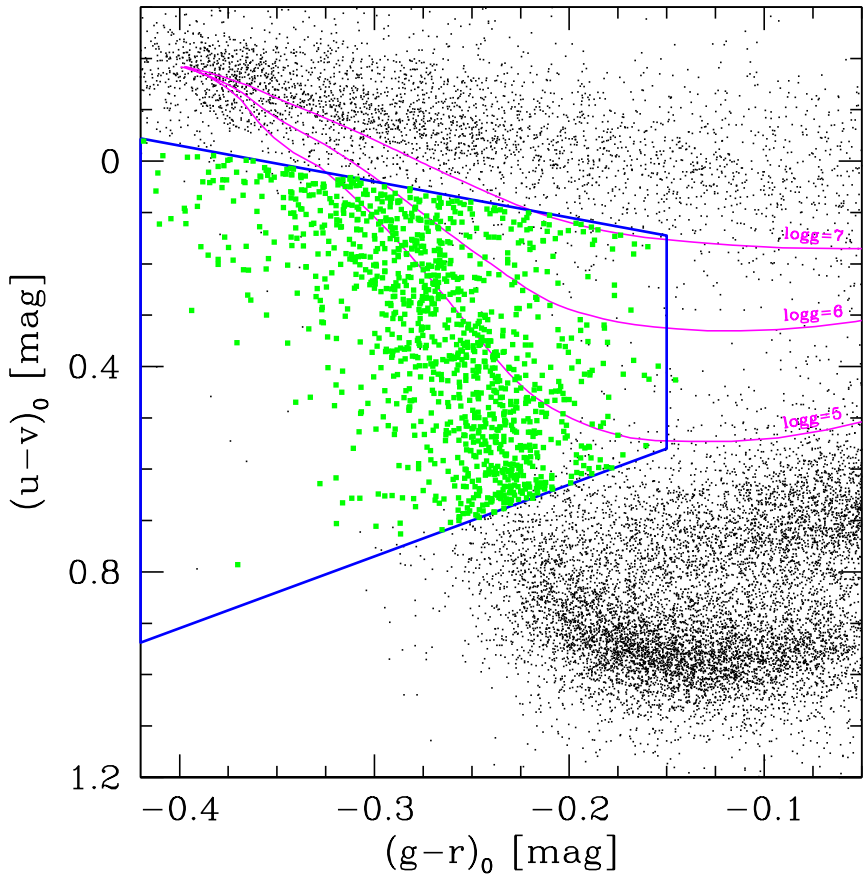

Fig. 4.2.— Target selection region for the SkyMapper DR1 data set as described in the text. Blue lines mark our target selection region. Green points represent all of our SkyMapper candidates. We overplot the DA white dwarf cooling tracks for log g=5, 6, and 7 as magenta lines.

Table 4.1. Observing setup summary for our ATLAS + SkyMapper observations.

Telescope	Instrument	Grating (lines mm^{-1})	Slit	Resolution (Å)	Spectral Coverage (Å)	# Targets Observed
SOAR 4.1m	Goodman	930	0.95″	2.4	3550 – 5250	48
			1.01″	2.6	3550 – 5250	487
Walter Baade 6.5m	MagE	175	0.70″	1.0	3600 – 7000	134
Tillinghast 1.5m	FAST	600	1.50″	1.7	3600 – 5400	10
			2.00″	2.3	3600 – 5400	2
MMT 6.5m	Blue Channel	832	1.00″	1.0	3500 – 4500	21
			1.25″	1.2	3500 – 4500	10

$$g > 10.5$$

$$-0.42 < (g-r)_0 < -0.15$$

$$0.7(g-r)_0 + 0.25 < (u-v)_0 < -1.4(g-r)_0 + 0.35$$

$$3.5(g-r)_0 + 1.0 < (u-g)_0 < 0.8 - (g-r)_0$$

$$0.91(r-i)_0 - 0.16 < (g-r)_0 < -0.425(r-i)_0 - 0.28$$

4.2.3 Observations

Because the previously known ELM white dwarfs in the main survey (Brown et al., 2020b) display an average 240 km s^{-1} velocity semi-amplitude, our observation setup is optimized to obtain radial velocity uncertainty of 10 km s^{-1}, which allows for reliable orbital solutions. We initially observed candidates based on color information. We perform atmospheric fits to each target at the end of each night. Targets with atmosphere solutions consistent with ELM white dwarfs are followed up with at least eight radial velocity measurements, including back-to-back exposures and exposures separated by 1 day to search for short and long-period variability. After our initial measurements, we then attempt to sample the fitted RV curve to reduce period aliasing.

Our target selection and observing strategy lead to a bias against the ELM white dwarfs that form through the stable Roche Lobe overflow channel (see Figure 10 of Li et al., 2019). Some of these are predicted to be found in longer period systems with lower velocity semi-amplitudes. Our observing strategy works well for the ELM white dwarfs

that we discover, but we are less likely to find the longer period systems by design. A summary of our observing setup for each our ATLAS+SkyMapper target lists is available in Table 4.1.

We observed 532 unique systems over 14 nights across three observing campaigns on March 2017 (NOAO Program ID: 2017A-0076), August 2017 (NOAO Program ID: 2017B-0173), and March 2018 (NOAO Program ID: 2018A-0233) using the SOAR 4.1-meter telescope located on Cerro Pachón, Chile. We used the Goodman high throughput spectrograph (Clemens et al., 2004) with the blue camera and 0.95″ or 1.01″ slits with 930 lines mm^{-1} grating resulting in spectral resolution of ≈2.5Å covering the wavelength range 3550 - 5250Å, which includes all of the Balmer lines except Hα. To ensure accurate wavelength calibration, we paired each target exposure with an FeAr or FeAr+CuAr calibration lamp exposure. We obtained multiple exposures of spectrophotometric standard stars each night to facilitate flux calibration. The median seeing for each night ranged from $0.8 - 1.0''$.

We observed 134 additional systems using the Walter Baade 6.5-meter telescope with the MagE spectrograph, located at the Las Campanas Observatory on Cerro Manqui, Chile. We used the 0.7″ slit with the 175 lines mm^{-1} grating resulting in spectral resolution of ≈1.0Å covering 3,600 - 7,000Å.

We observed 12 additional systems using the Fred Lawrence Whipple Observatory (FLWO) 1.5-meter Tillinghast telescope with the FAST spectrograph, located on Mt. Hopkins, Arizona. We used the 1.5″ or 2.0″ slits with the 600 lines mm^{-1} grating resulting in spectral resolution of ≈1.7Å or ≈2.3Å between 3,600Å - 5,400Å.

We observed 31 additional systems using the MMT 6.5-meter telescope with the Blue

Channel Spectrograph, located on Mt. Hopkins, Arizona. We used the 1.0″ or 1.25″ slits with the 832 lines mm^{-1} grating resulting in spectral resolution of 1.0Å or 1.2Å covering the wavelength range 3,500 - 4,500Å.

4.2.4 Radial Velocity and Orbital Fits

We used the IRAF cross-correlation package RVSAO (Kurtz & Mink, 1998) to calculate radial velocities. For each object, we first cross-correlated all spectra with a low-mass white dwarf template and then summed them to produce a zero-velocity spectrum unique to that object. We then measured radial velocities for each exposure against the object-specific zero-velocity template and corrected for the Solar System barycentric motion. We obtained median radial velocity uncertainty of 10 km s^{-1}. To confirm the binary nature of our candidates, we performed orbital fitting to radial velocity measurements using a Monte Carlo approach based on Kenyon & Garcia (1986).

4.2.5 Stellar Atmosphere Fits

We obtained stellar atmosphere parameters by fitting all of the visible Balmer lines Hγ to H12 in the summed spectra to a grid of pure-Hydrogen atmosphere models that cover the range of 4,000 K $\leq T_{\rm eff} \leq$ 35,000 K and 4.5 $\leq \log g \leq$ 9.5 and include Stark broadening profiles of Tremblay & Bergeron (2009a). Extrapolation was performed for targets with temperatures or $\log g$ outside of this range. Specifics for our fitting technique can be found in detail in Gianninas et al. (2011, 2014). For the systems in which the Ca II K line is visible, we mask out the data in the wavelength region surrounding and including the Ca II 3933.66Å line from our fits.

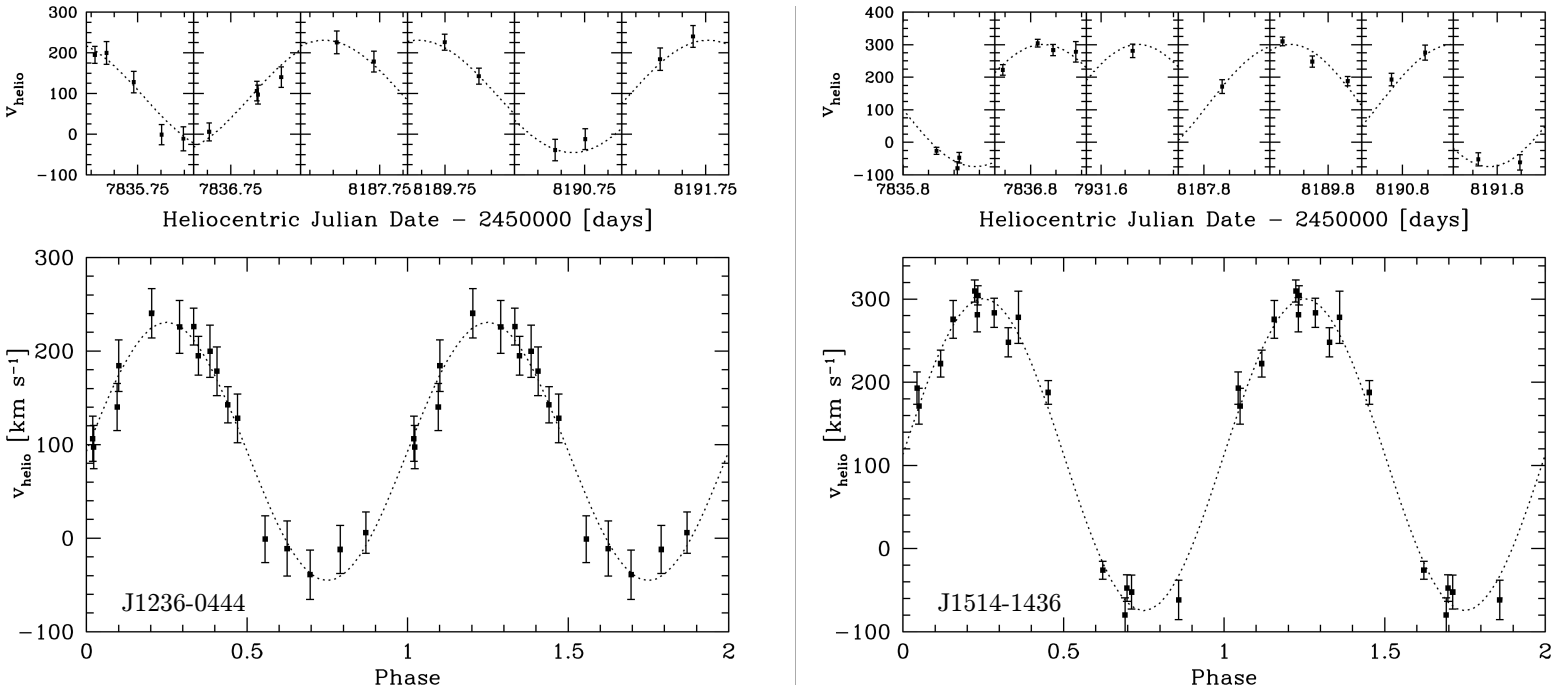

Fig. 4.3.— Top: observed radial velocities for J1236−0444 (left) and J1514−1436 (right) with best-fit orbit overplotted as a dotted line. Bottom: radial velocity data phase-folded to best-fit period. A table of radial velocity measurements is available in the Appendix.

4.2.6 ELM White Dwarfs in ATLAS+SkyMapper

We fit pure-Hydrogen atmosphere models to all 709 unique targets that show Balmer lines and note that only 33 of these systems are consistent with ELM white dwarf temperature and surface gravity. Of these systems, J0027−1516 and J1234−0228 are previously published ELM white dwarfs (Brown et al., 2020b; Kilic et al., 2011). We obtained follow-up spectra and constrained the orbit of three of these systems and confirm that two (J123619.70−044437.90 and J151447.26−143626.77) are ELM white dwarfs, while the third system (J142555.01−050808.60) is likely a metal-poor sdA star. We briefly discuss J1425−0508 in the following section. Figures 4.3 and 4.4 show our orbital and model atmosphere fits for J1236−0444 and J1514−1436.

J1236−0444 is an ELM white dwarf with best-fit atmosphere solution of $\log g = 6.28 \pm 0.02$ and $T_{\rm eff}$ = 11,100 ± 110 K. Istrate et al. (2016) He-core ELM white dwarf evolutionary tracks indicate that J1236−0444 is a 0.156±0.01 $M_\odot$ white dwarf. Orbital fits to the 17 radial velocity measurements give a best-fit period of 0.68758 ± 0.00327 d with velocity semi-amplitude of 138.0 ± 6.6 km s^{-1} (Figure 4.3, left). Using the binary mass function

$$\frac{(M_2 \sin i)^3}{(M_1 + M_2)^2} = \frac{PK^3}{2\pi G}, \tag{4.1}$$

with primary ELM white dwarf mass M_1, orbital period P, velocity semi-amplitude K, and inclination $i = 90°$, we calculate the minimum companion mass $M_{2,\rm min} = 0.37 \pm 0.04$ $M_\odot$.

J1514−1436 is an ELM white dwarf with best-fit atmosphere solution of $\log g = 5.91 \pm 0.05$ and $T_{\rm eff}$ = 9,170 ± 30 K. Istrate et al. (2016) He-core ELM white dwarf

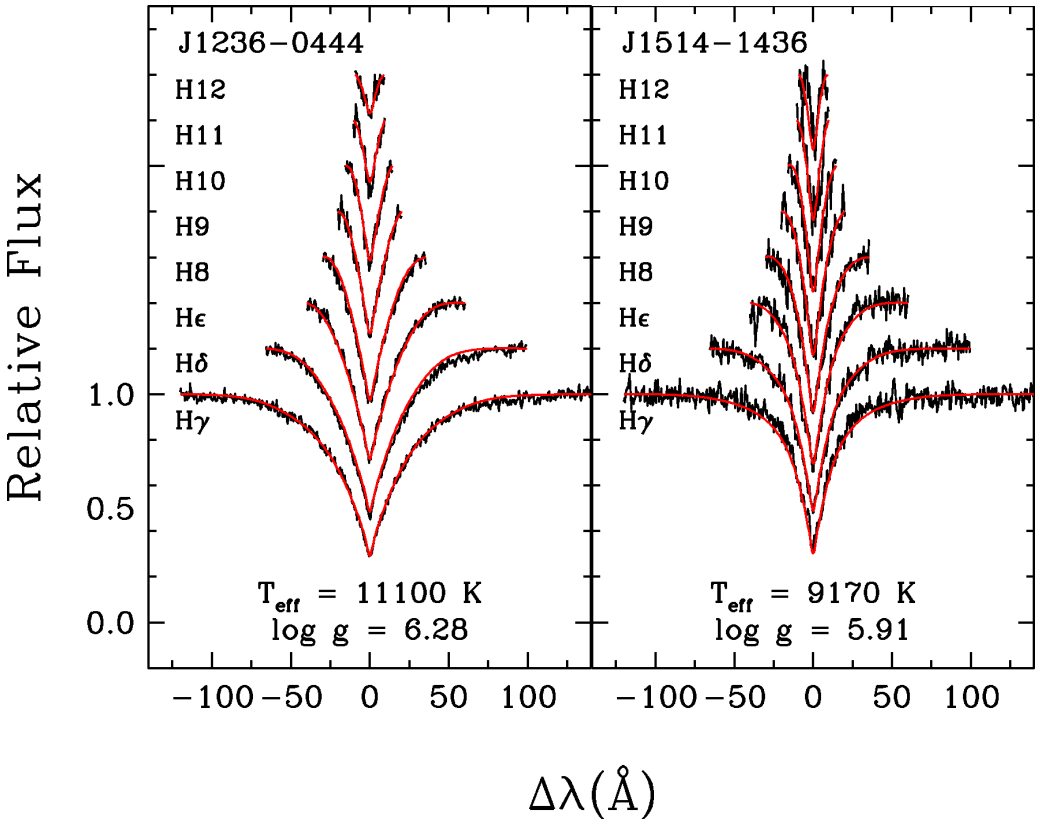

Fig. 4.4.— Normalized Balmer line profiles for J1236−0444 (left) and J1514−1436 (right) with best-fitting pure Hydrogen atmosphere model (up to H12) overplotted in red. Line profiles are shifted vertically for clarity. The wavelength region surrounding the Ca II 3933.66Å line was masked from the fit to J1514−1436.

evolutionary tracks indicate that J1514−1436 is a 0.167±0.01 $M_\odot$ white dwarf. Orbital fits to the 16 radial velocity measurements give a best-fit period of 0.58914 ± 0.00244 d with velocity semi-amplitude 187.7 ± 6.6 km s^{-1} (Figure 4.3, right). The minimum companion mass for this system is 0.64 ±0.06 $M_\odot$.

The orbit of compact double degenerate systems slowly decays due to the loss of angular moment caused by the emission of gravitational waves (Landau & Lifshitz, 1958). The merger timescale of these systems can be calculated if the mass of each object and their orbital period is known by using the equation

$$\tau_{\rm merge} = \frac{(M_1 + M_2)^{1/3}}{M_1 M_2} P^{8/3} \times 10^{-2} \text{ Gyr} \tag{4.2}$$

where M_1 and M_2 are the ELM white dwarf and companion star masses in solar masses, and P is the period in hours. We use Equation 3.2 together with the minimum companion mass, $M_{2,\rm min}$, to estimate the maximum merger time for these systems. Neither J1236−0444 nor J1514−1436 will merge within a Hubble time.

4.2.7 sdAs in ATLAS+SkyMapper

In addition to cool ELM white dwarfs, there exists a large population of subdwarf A-type (sdA) stars with $7,000 \text{ K} < T_{\rm eff} < 20,000$ K (with most below 10,000 K) and $4.5 < \log g < 6.0$ (Kepler et al., 2016; Pelisoli et al., 2018a) that are often confused with ELM white dwarfs in low-resolution spectroscopy. Brown et al. (2017b) and Pelisoli et al. (2018a,b) have shown that the surface gravities derived from pure-hydrogen atmosphere model fits suffer from up to 1 dex error for sdA stars. This is likely due to metal line blanketing that is missing in the pure-hydrogen atmosphere models and the lower

signal-to-noise ratio of observed spectra below 3,700 Å.

We note that while 33 of our objects appear to have atmospheres consistent with ELM white dwarfs, 29 are cool ($T_{\rm eff} < 10,000$ K) and share their parameter space with sdA stars. Yu et al. (2019) have shown through binary population synthesis that only 1.5% of sdA stars in a 10 Gyr old population are ELM white dwarfs, with the remaining 98.5% being metal-poor main sequence stars (see also Pelisoli et al., 2018a, 2019). Therefore, the majority of our 29 candidates with $\log g = 5 - 7$ and $T_{\rm eff} = 8,000 - 10,000$ K are likely metal-poor main-sequence stars.

We obtained 25 radial velocity measurements for one of these candidates, J1425−0508. Figure 4.5 displays our best-fit model atmosphere and orbital fits. J1425−0508 is best-explained by a 8,570 K and $\log g = 5.59$ model based on the assumption of a pure Hydrogen atmosphere. Our radial velocity measurements result in the best-fit period of 0.798 ± 0.005 d with velocity semi-amplitude $K = 54.1 \pm 3.4$ km s^{-1}. As demonstrated by Brown et al. (2017b) and Pelisoli et al. (2018a), the surface gravity for such a cool object is likely over-estimated, and the relatively low semi-amplitude of the velocity variations and the Gaia parallax of 0.25 ± 0.08 mas favors a low-metallicity main-sequence sdA star, rather than a cool ELM white dwarf.

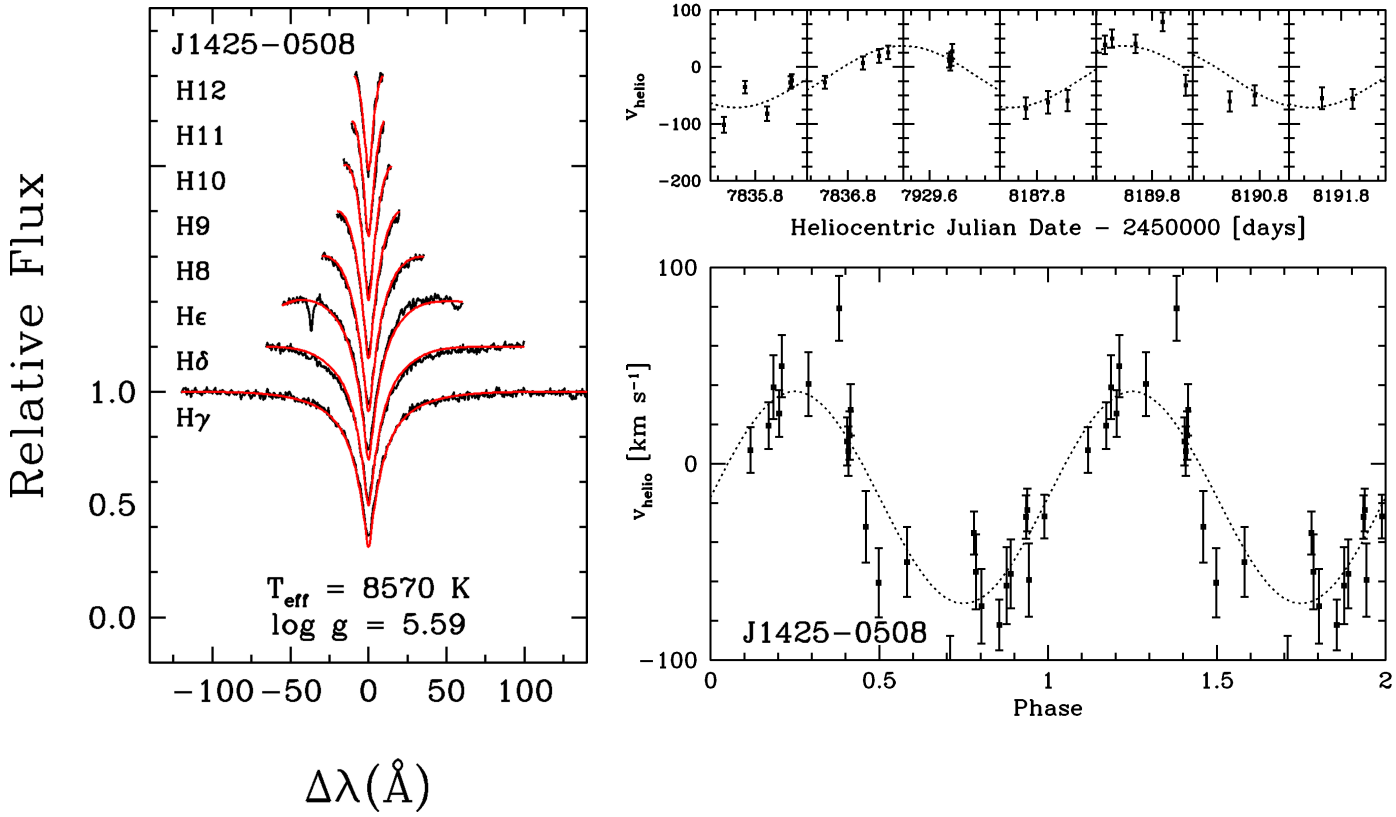

Fig. 4.5.— Best-fit pure Hydrogen atmosphere model and radial velocity measurements of J1425−0508. A table of radial velocity measurements is available in the Appendix.

Given the problems with distinguishing ELM white dwarfs from sdAs, we use the eclipsing system NLTT 11748 (Steinfadt et al., 2010) as a prototype to estimate the radii of each of our candidates. NLTT 11748 is a well-studied eclipsing ELM white dwarf system with $T_{\rm eff} \approx 8,700$ K and $R \approx 0.043$ $R_\odot$ (Kaplan et al., 2014). We use a similar approach to what is done by Brown et al. (2020b) and compare the Gaia parallax for each candidate with its predicted parallax if it were similar in nature to NLTT 11748, obtained by inverting the distance calculated from the candidate's apparent magnitude and the absolute magnitude of NLTT 11748. This comparison provides a radius estimate relative to a known ELM white dwarf.

Figure 4.6 shows the comparison between predicted parallax and Gaia parallax for each of our 29 candidates with the 1:1 and 50:1 lines overplotted. We note that most candidates are consistent with the 50:1 line to within 2σ, suggesting that they are ~50 times larger than NLTT 11748 with radii R~2 $R_\odot$. J0155−4148 is a strong ELM white dwarf candidate; it lies along the 4:1 line with a radius compatible with an ELM white dwarf. We note that there are four additional candidates that are consistent with the 1:1 line, but their Gaia parallax values are uncertain with `parallax_over_error<2`. We will present our follow-up observations of J0155−4148 in a future publication.

4.2.8 Survey Efficiency

From our ATLAS+SkyMapper color-selection method, we observed 709 unique systems. Of these systems, we confirm only four to contain an ELM white dwarf, two of which were previously known. In addition to these four confirmed ELM white dwarfs, we report 123 DA white dwarfs with $\log g > 7.0$ (Table 4.4) and 29 additional candidates with

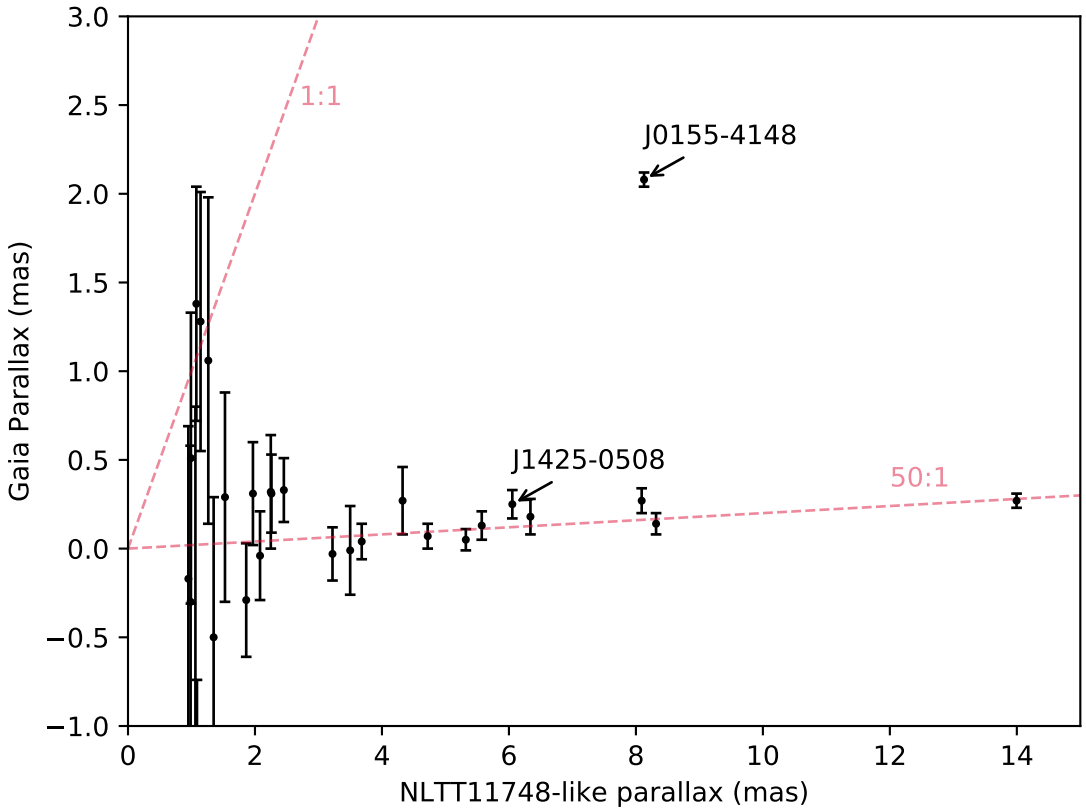

Fig. 4.6.— Comparison between Gaia parallax and predicted NLTT 11748-like parallax for the 29 sdA stars identified in our survey. 1:1 and 50:1 parallax ratio lines are marked as red dashed lines and labeled. Candidates consistent with the 50:1 line have a radius estimate of $R \sim 2R_{\odot}$ and cannot be white dwarfs. Candidate J0155−4148 lies along the 4:1 line with a radius compatible with an ELM WD.

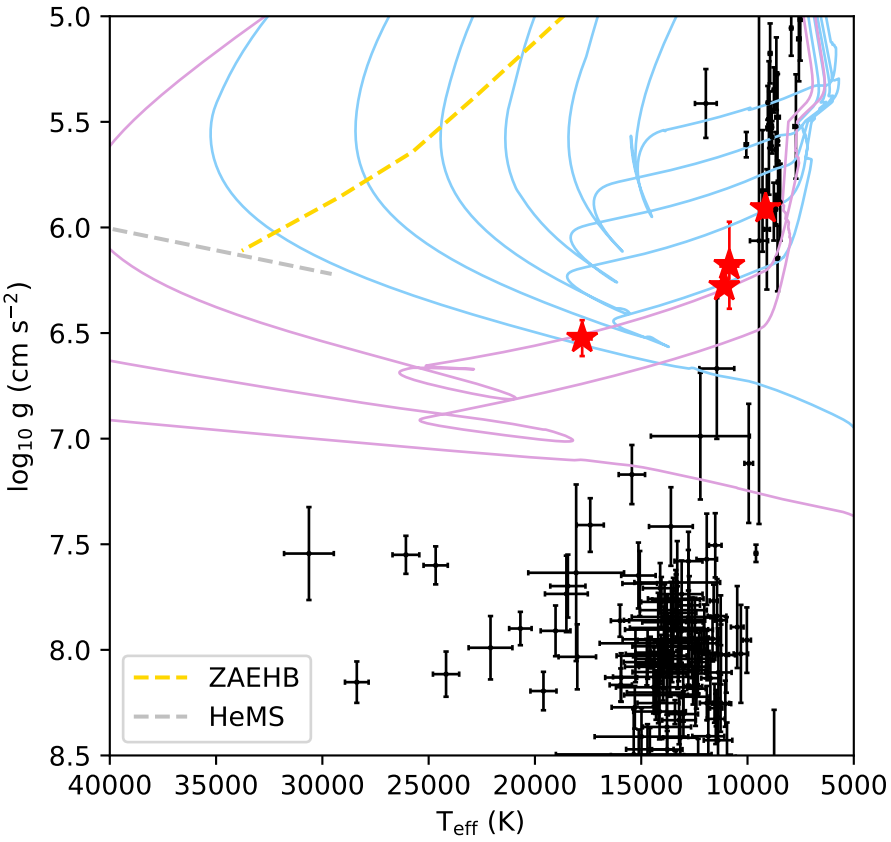

Fig. 4.7.— $\log g$ vs $T_{\rm eff}$ plot of our VST ATLAS DR2+DR3 and SkyMapper DR1 targets with Hydrogen-dominated atmospheres and $\log(g) > 5.0$. Red stars show the locations of the confirmed ELM systems identified through our color selection. Evolutionary tracks for 0.205 $M_\odot$ (light blue) and 0.306 $M_\odot$ (purple) ELM WDs from Istrate et al. (2016) are overplotted. Hydrogen shell flashes during evolution cause loops seen in the model tracks. The silver and gold dashed lines show the locations of the Helium main sequence (HeMS) and zero-age extreme-horizontal branch (ZAEHB), respectively. The group of objects at $T_{\rm eff} \approx 10,000$ K and $\log g \lesssim 6.0$ are normal subdwarf type-A stars. Much of our seletion resulted in normal-mass white dwarfs, seen as the group of objects at $\log g \approx 8.0$.

$5.0 < \log g < 7.0$ (Table 4.5). This low efficiency in our photometric selection may be due to potential color calibration issues in the ATLAS DR3 dataset. In addition, the low efficiency of the SkyMapper selection is likely due to the shallow depth of the SkyMapper DR1, which limits the survey volume for ELM white dwarfs.

Figure 4.7 shows the distribution of temperatures and surface gravities for all targets observed as a part of our ATLAS + SkyMapper DR1 color selection with $\log g \geq 5.0$. We mark the locations of the four observed ELM white dwarf systems with red stars. We overplot the 0.2 $M_{\odot}$ (light blue) and 0.3 $M_{\odot}$ (purple) white dwarf evolutionary tracks of Istrate et al. (2016).

In total, we confirm that only four of our systems (plus the candidate system J0155−4148) contain an ELM white dwarf, two of which are new discoveries. Our ATLAS + SkyMapper target selection method has an ELM white dwarf detection efficiency of ∼0.6% and a white dwarf detection efficiency of about 18%, making the majority of our targets unaligned with our targets of interest.

We note that all four of our confirmed ELM white dwarfs originated from our ATLAS sample. Given the surface density of ELM white dwarfs between $17 < g < 20$ in the SDSS footprint, we expect to find ∼10 ELM white dwarfs in our observed ATLAS sample. However, the spatial distribution of our candidates varied systematically over the ATLAS DR3 footprint, suggesting that photometric calibration in the VST ATLAS DR3 varied across the survey. Similarly for the $15 < g < 17$ ELM white dwarf sample in the SDSS footprint, we expect to find one ELM white dwarf within our observed SkyMapper sample. While we have not yet confirmed the nature of J0155−4148, this system originated from our SkyMapper sample and is likely an ELM white dwarf. Our SkyMapper results are

consistent with what is expected given the lower limiting magnitude.

4.3 Gaia Parallax Based Selection

The availability of Gaia DR2 in April 2018 opened a new window into ELM white dwarf target selection. Gaia photometry and parallax measurements provide a direct measurement of the luminosity of each object, enabling a clear distinction between low-luminosity white dwarfs and brighter main-sequence stars. ELM white dwarfs are a few times larger in radii compared to average 0.6 $M_{\odot}$ white dwarfs at the same temperature (color), but they are still significantly smaller than A-type stars. Hence, Gaia parallaxes provide a powerful method to create relatively clean samples of ELM white dwarfs (see also Pelisoli & Vos, 2019), and also for the first time enable an all-sky survey.

Since the ELM Survey has already observed the SDSS footprint, here we focus on the southern sky, but exclude the Galactic plane ($|b| < 20^{\circ}$) due to significant extinction and avoid the Small and Large Magellanic Clouds. We also apply cuts to astrometric noise and color excess based on recommendations from Lindegren et al. (2018). Figure 4.8 shows the distances and Gaia magnitudes for sources with $-0.4 < G_{\rm BP} - G_{\rm RP} < 0.2$. This color range corresponds to $T_{\rm eff} = 8,000 - 25,000$ K, where Balmer lines are relatively strong. Green lines mark the region for $M_G = 6.0 - 9.7$ mag objects, and blue and red triangles mark the previously confirmed normal white dwarfs and ELM white dwarfs in this magnitude range, respectively. Magenta triangles mark other types of previously known objects, like subdwarf B stars and cataclysmic variables (CVs).

For a more intuitive look at our target selection region, we plot the same sample

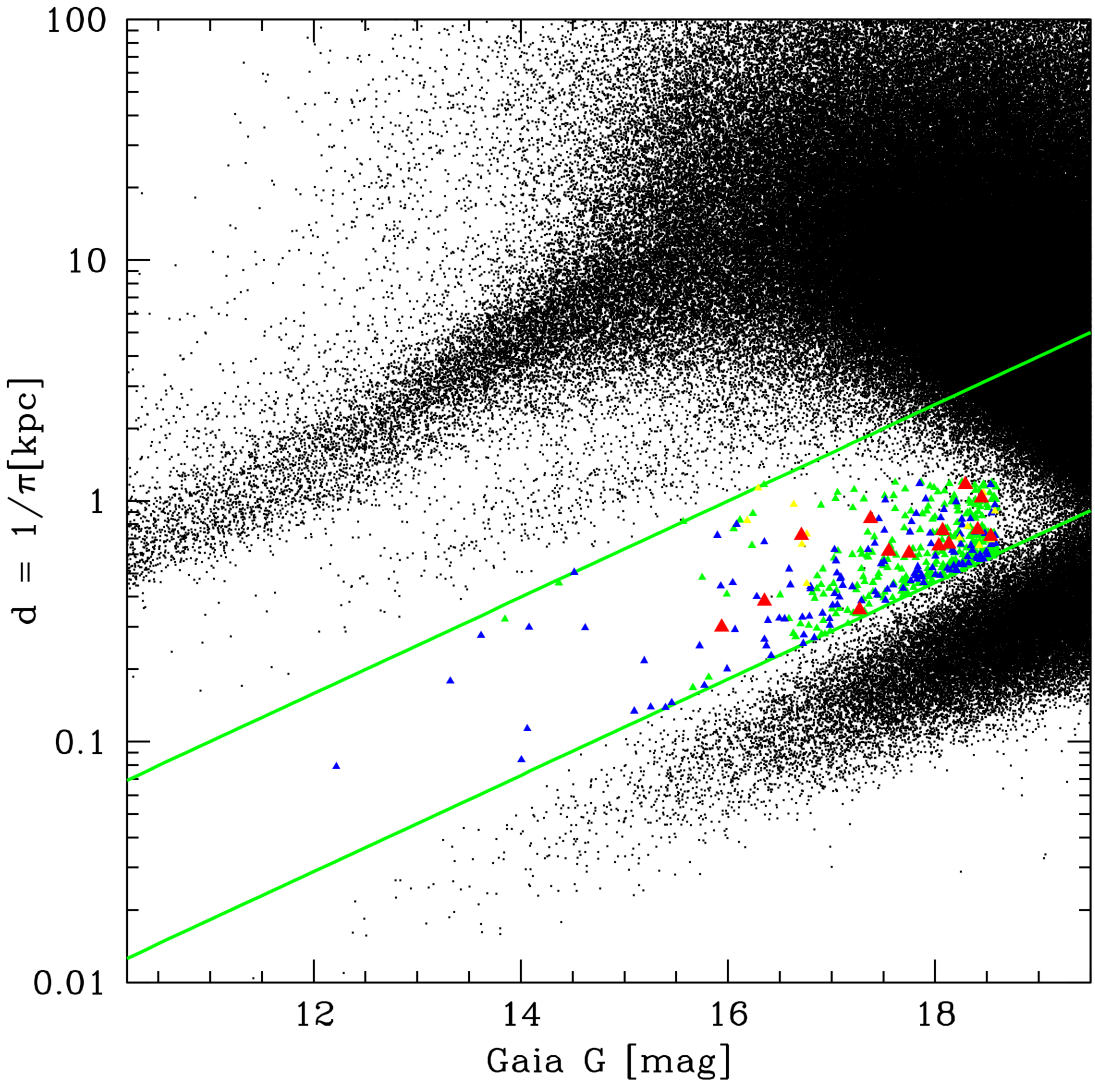

Fig. 4.8.— Target selection region for Gaia parallax method described in text. Green lines mark the region for $M_G = 6.0 - 9.7$ mag. Green triangles are the ELM candidates identified through our Gaia parallax selection. Red triangles are known ELMs. Blue triangles are known WDs. Yellow triangles are other types of previously known objects, like subdwarf B stars and cataclysmic variables.

on a color-magnitude diagram in Figure 4.9. The white dwarf sequence stretches from $M_G = 10$ mag on the left to about 12 mag on the right. Our Gaia-selected targets are all over-luminous compared to this sequence and are dominated by relatively hot white dwarf candidates with bluer colors. Since we did not impose a cut on parallax errors, the top right portion of this diagram is dominated by non-white dwarf stars that are scattered into this region due to large parallax errors.

To minimize contamination from main-sequence stars, we limit our target selection to the region defined by parallax-distance $(1/\varpi) < 1.2$ kpc, and to remove potential contamination from poorly-calibrated colors on fainter targets, we limit the apparent Gaia G-band magnitude to $G < 18.6$ mag. Because normal white dwarfs dominate at larger absolute magnitudes, we impose an absolute G-band magnitude limit of $M_G < 9.7$ to avoid large numbers of normal white dwarfs. Our Gaia target selection resulted in 573 candidates, 180 of which were also identified by Pelisoli & Vos (2019) as ELM white dwarf candidates.

Our Gaia target selection is defined by

$|b| \geq 20$

$G < 18.6$ mag

$6.0 < M_G < 9.7$

$\texttt{R.A.} > 100^\circ$ or ($\texttt{R.A.} < 100^\circ$ & $\texttt{Dec.} > -60^\circ$)

$\texttt{phot\_bp\_mean\_flux\_over\_error} > 10$

$\texttt{phot\_rp\_mean\_flux\_over\_error} > 10$

$-0.4 \leq (G_{BP} - G_{RP}) \leq 0.2$

$\frac{1}{\varpi} < 1.2$

We observed a total of 82 unique systems over four consecutive nights in March 2019 (NOAO Program ID: 2019A-0134). All observations were taken with the SOAR 4.1-meter telescope using the Goodman Blue Spectrograph with the 1.01″ long-slit resulting in a spectral resolution of 2.6Å covering the wavelength range of 3550Å - 5250Å. Median seeing for each night was between 0.8 − 1.0 arcsec. Radial velocities, orbital solutions, and model atmosphere fits were obtained identically to as described in section 2.

4.3.1 Results

We fit pure-Hydrogen atmosphere models to all 82 targets and identify six systems consistent with ELM white dwarfs. Figure 4.10 shows our model fits to the Balmer line profiles for these six systems. All six are hotter than 10,000 K, have $\log g = 5 - 7$, and

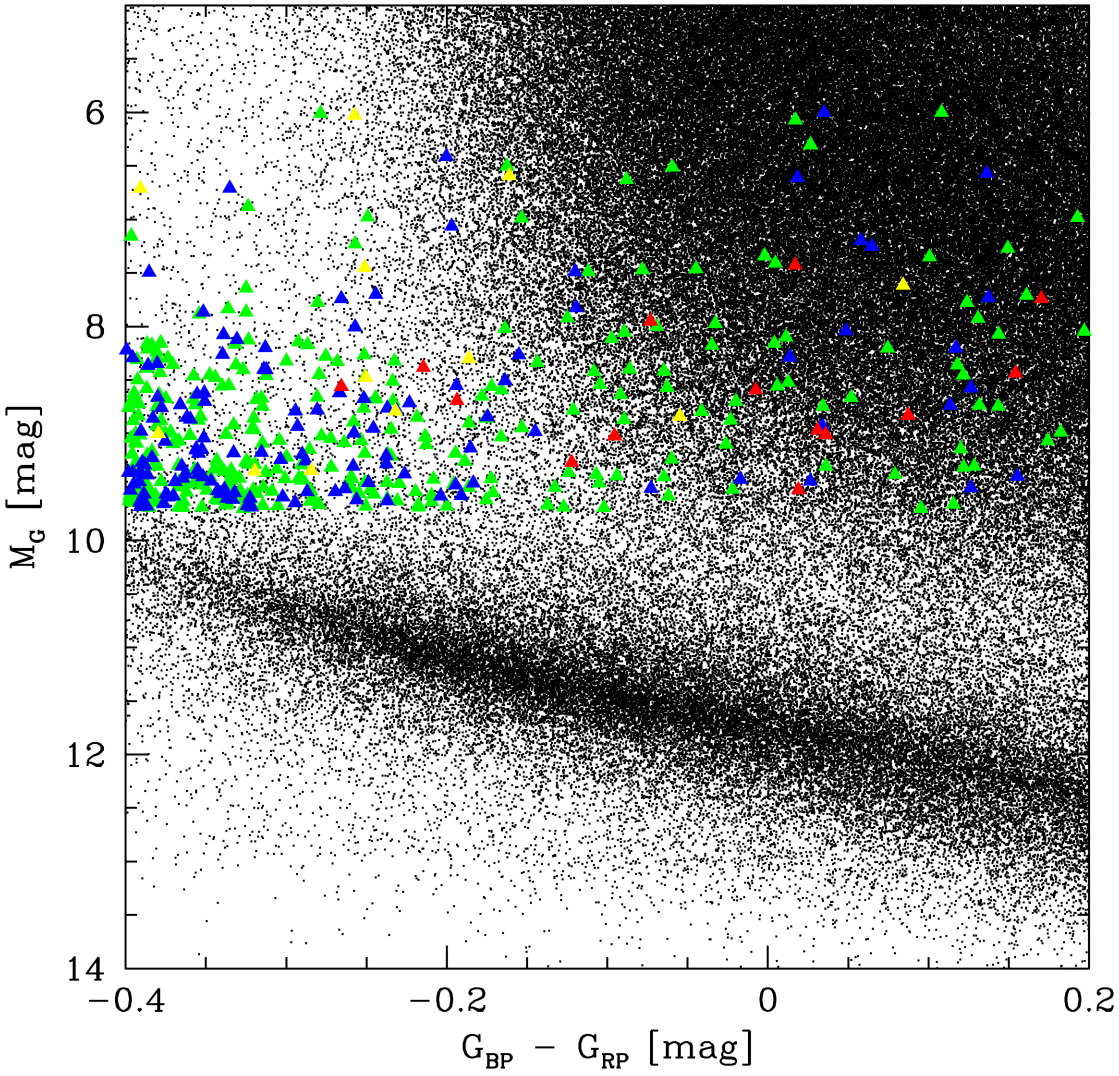

Fig. 4.9.— Color-magnitude diagram corresponding to our Gaia parallax selection described in the text. The symbols are the same as in Figure 8. We select objects with Gaia magnitude $M_G = 6.0 - 9.7$ mag.

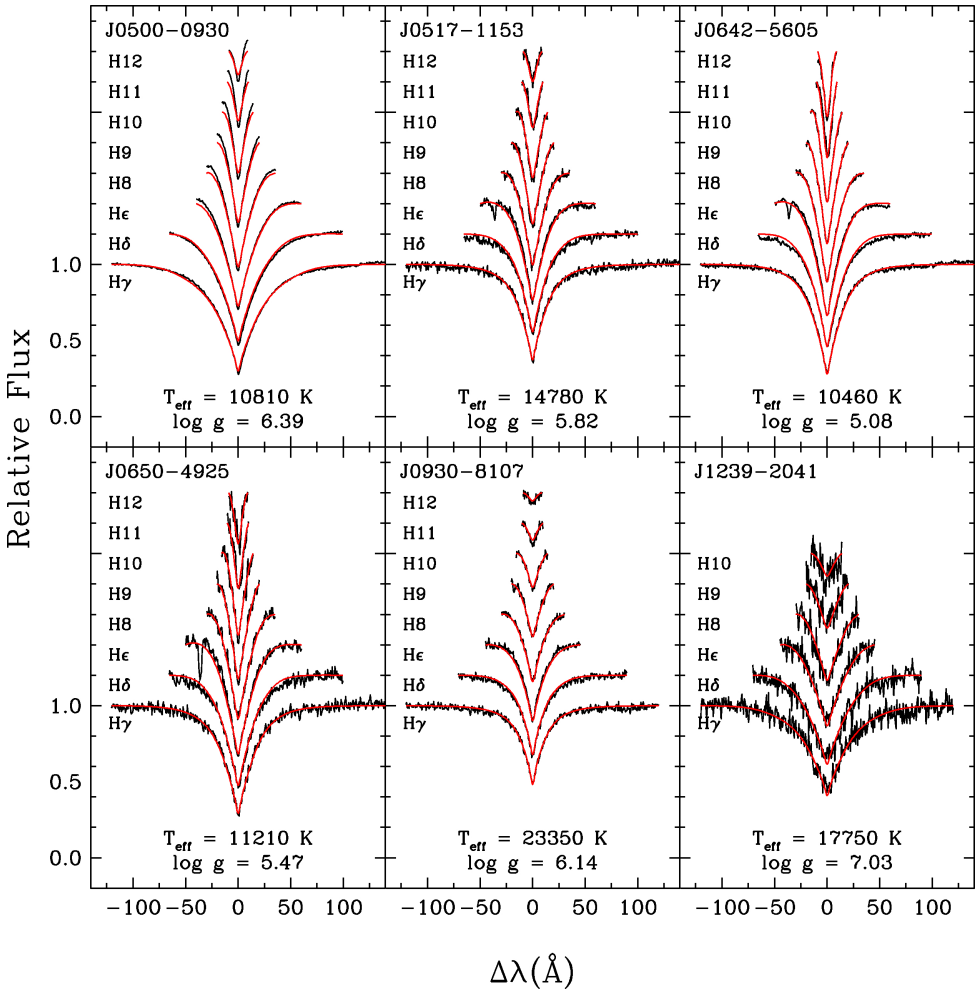

Fig. 4.10.— Normalized Balmer line profiles for the six new ELM WD systems identified through our Gaia DR2 parallax selection. Best-fit pure-Hydrogen atmosphere models are overplotted in red with best-fit parameters printed in each subfigure. The Ca II K line at 3933.66Å in the wing of Hϵ is masked from fits where it is visible. Line profiles are shifted vertically for clarity. Due to lower signal-to-noise, we limit our fitting of J1239−2041 to include only up to H10.

show significant velocity variability. However, we were only able to constrain the orbital period for four of these systems so far. Details for each system are discussed below.

J0500−0930

J050051.80−093056.98 (2MASS J05005185−0930549) was originally identified as an ELM white dwarf candidate by Scholz et al. (2018) for its high proper motion. To explain its over-luminous nature, Scholz et al. (2018) suggested that the system contains an ELM white dwarf and estimate atmospheric parameters $\log g \approx 6 - 6.5$ and $T_{\rm eff}$ = 11,880 ± 1,100 K.

We obtained $\log g = 6.39 \pm 0.02$ and $T_{\rm eff}$ = 10,810 ± 40 K from fitting our SOAR spectra with pure H atmosphere models, in agreement with the original estimates of Scholz et al. (2018). We obtained seven radial velocity measurements of J0500−0930 with SOAR 4.1-meter telescope using the Goodman spectrograph, 50 with the FLWO 1.5-meter telescope using FAST, and one with the MMT 6.5-meter telescope with the Blue Channel Spectrograph. Fitting an orbit to this combined dataset of 58 spectra resulted in a best-fit period of $P = 0.39435 \pm 0.00001$ d with velocity semi-amplitude $K = 146.8 \pm 8.3$ km s^{-1} (Figure 4.11). We use the ELM white dwarf evolutionary models of Istrate et al. (2016) to estimate its mass to be 0.163 ± 0.01 $M_\odot$ and calculated its minimum companion mass to be 0.30 ± 0.04 $M_\odot$, potentially making this a double low-mass white dwarf system. With apparent Gaia G-band magnitude of 12.6 and Gaia parallax of 13.97 ± 0.05 mas, this is currently both the brightest and closest known ELM white dwarf system. This system will not merge within a Hubble time.

J0500−0930 was within the field of view of the Transiting Exoplanet Survey Satellite

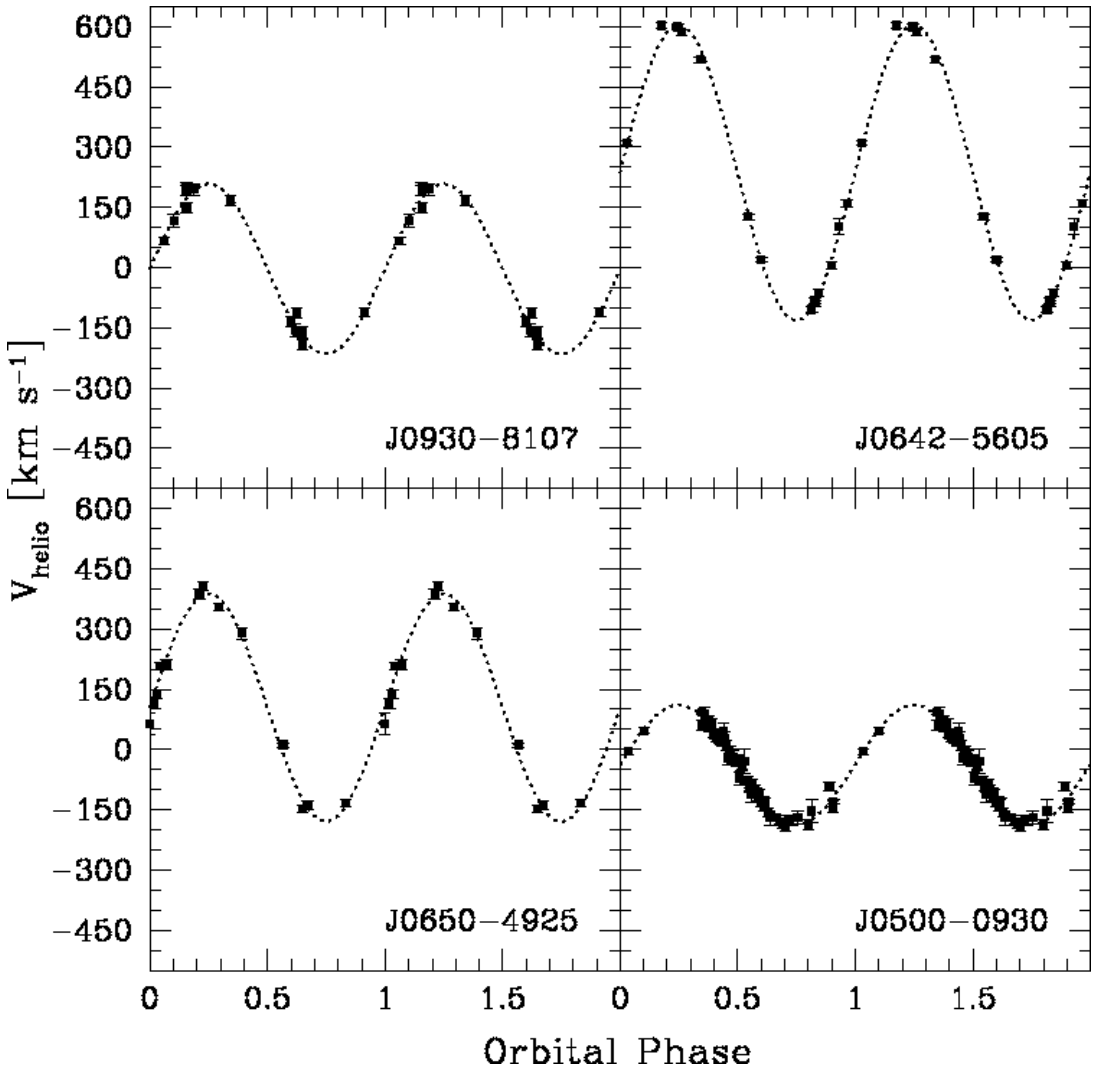

Fig. 4.11.— Best-fit orbital solutions plotted as a function of phase to the four constrained ELM WD systems based on data from SOAR, FLWO, and MMT. A table of radial velocity measurements is available in the Appendix.

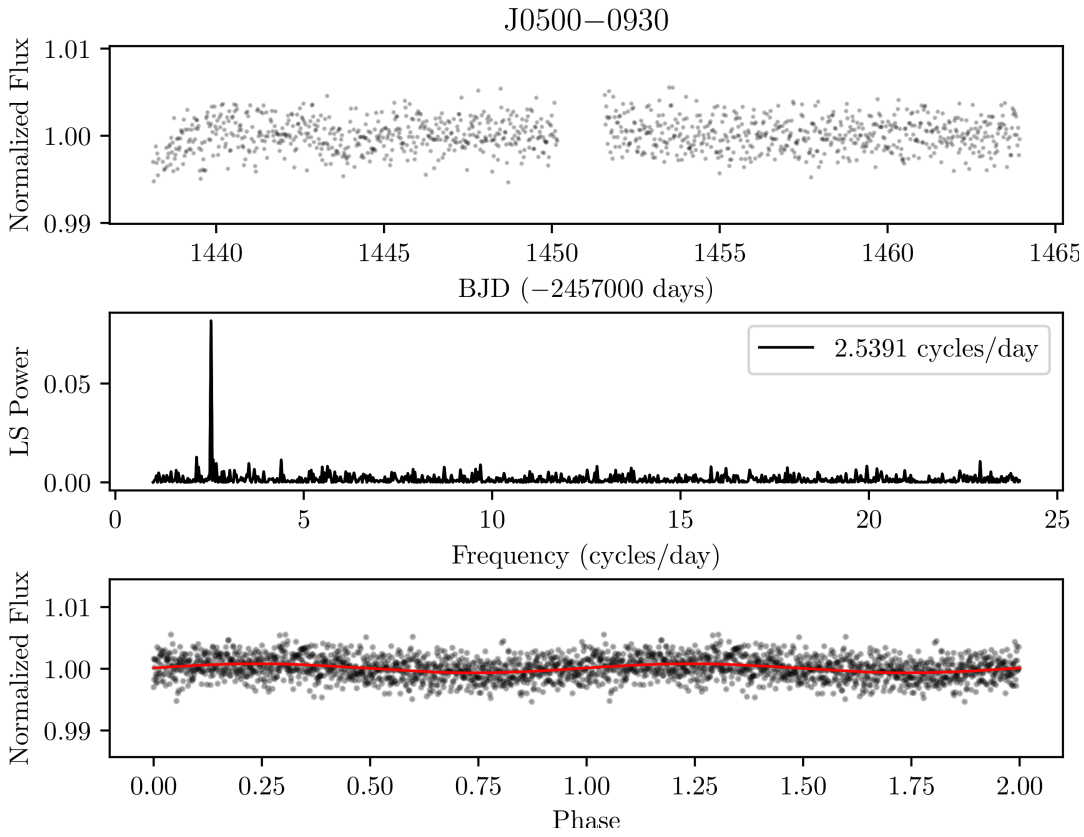

Fig. 4.12.— TESS Light curve (top), Lomb Scargle periodogram (middle), and phase folded light curve (bottom) of J0500−0930. We overplot the best-fit frequency model onto the phase folded light curve for clarity.

TESS (Ricker et al., 2015) during Sector 5 observations. TESS provides Full-Frame Images (FFIs) of each sector at 30-minute cadence over a roughly 27 d observing window. We used the open source Python tool eleanor (Feinstein et al., 2019) to produce a light curve for J0500−0930. We downloaded a time series of 15 pixels by 15 pixels "postcards" containing TESS data for the target and its immediate surroundings from the Mikulski Archive at the Space Telescope Science Institute (MAST). We then perform background subtraction, aperture photometry, and correct for instrumental systematic effects. We use the corrected flux measurements with data quality flags set to 0 to remove data points that are affected by issues like attitude tweaks or cosmic rays (Feinstein et al., 2019).

We use the Astropy implementation of the Lomb Scargle periodogram to check for variability in the TESS data. Figure 4.12 shows the TESS FFI light curve of J0500−0930, its Lomb Scargle periodogram, and phase folded light curve at the highest-peaked frequency. Remarkably, there is a small ($0.074^{+0.008}_{-0.007}$%) but significant peak at a frequency of 2.5391 ± 0.0025 cycles d^{-1}. This frequency is within 1.3σ of the orbital frequency measured from our radial velocity data. The predicted amplitude of the relativistic beaming effect in J0500−0930 is ~ 0.1% (Shporer et al., 2010). However, since the TESS pixels are relatively large (21 arcsec pixel^{-1}) and 90% of the point spread function is spread over 4 pixel^2, dilution by neighboring sources is common in the TESS data. There are two relatively red sources with $G_{\rm RP}$ = 16.0 and 16.9 mag within a 2 pixel radius of J0500−0930 that likely dilute the variability signal. Hence, the observed photometric variability is consistent with the relativistic beaming effect, confirming our orbital period measurement from the radial velocity data.

J0517−1153

J051724.97−115325.85 has a best-fit atmosphere solution of $\log g = 5.82 \pm 0.02$ and $T_{\rm eff}$ = 14,780 ± 70 K (Figure 4.10), making this a clear ELM white dwarf system. We obtained 13 spectra of this object over four nights and detect significant radial velocity variations. However, due to significant period aliasing in the best-fit orbit, further follow-up is required to constrain its orbit and determine companion mass and merger time. TESS full-frame images of J0517−1153 do not reveal any significant photometric variability.

J0642−5605

J064207.99−560547.44 is an ELM white dwarf with $\log g = 5.08 \pm 0.02$ and $T_{\rm eff}$ = 10,460 ± 70 K (Figure 4.10). We obtained 14 spectra, resulting in best-fit orbit with period $P = 0.13189 \pm 0.00006$ d and velocity semi-amplitude $K = 368.0 \pm 27.0$ km s^{-1} (Figure 4.11). The minimum companion mass is 0.96 ± 0.17 M$_\odot$. J0642−5605 will merge within 1.3 Gyr.

J0642−5605 is within the continuous viewing zone of the TESS mission, and was observed as part of Sectors 1-13, except Sector 7. Figure 4.13 shows the TESS FFI light curve of J0642−5605 obtained over almost a year, its Lomb Scargle periodogram, and phase folded light curve at the highest-peaked frequency. This white dwarf shows 2.77 ± 0.02% photometric variability at a frequency of 15.17820 cycles per day, which is roughly twice the orbital frequency measured from our radial velocity data. In addition, there is a smaller but significant peak at the orbital period of the system. Hence, TESS data not only confirm the orbital period, but also reveal variability at half the orbital period, revealing ellipsoidal variations in this system. These variations are intrinsic to the source,

and are also confirmed in the ASAS-SN data (Kochanek et al., 2017).

J0650−4925

J065051.48−492549.46 is an ELM white dwarf with best-fit atmosphere solution of $\log g = 5.47 \pm 0.03$ and $T_{\rm eff}$ = 11,210 ± 90 K (Figure 4.10). From our 13 radial velocity measurements, we obtained a best-fit orbital period $P = 0.17453 \pm 0.00028$ d with velocity semi-amplitude $K = 284.2 \pm 39.4$ km s^{-1} (Figure 4.11). The minimum companion mass is 0.67 ± 0.21 $M_\odot$. J0650−4925 will merge within a Hubble time, with a maximum gravitational wave merger time of 3.6 Gyr. TESS full-frame images on J0650−4925 do not reveal any significant photometric variability.

J0930−8107

J093008.47−810738.32 is an ELM white dwarf with best-fit atmosphere solution of $\log g = 6.14 \pm 0.02$ and $T_{\rm eff}$ = 23,350 ± 120 K (Figure 4.10). Fitting 14 radial velocity measurements, we obtained for the best-fit period $P = 0.08837 \pm 0.00005$ d with velocity semi-amplitude $K = 212.0 \pm 9.0$ km s^{-1} (Figure 4.11). J0930−8107 has a mass of 0.24 ± 0.01 $M_\odot$ with minimum companion mass of 0.29 ± 0.02 $M_\odot$, potentially making this a double ELM white dwarf system. J0930−8107 will merge within a Hubble time, with a maximum gravitational wave merger time of 0.9 Gyr.

J0930−8107 is included in Sectors 11, 12, and 13 of the TESS mission full-frame images. The combined light curve and its FT show a peak at 7.084 cycles per day with 0.035 ± 0.006 amplitude. However, this peak is only visible in the Sector 11 data, indicating that it is most likely not intrinsic to the star. J0930−8107 is the shortest period

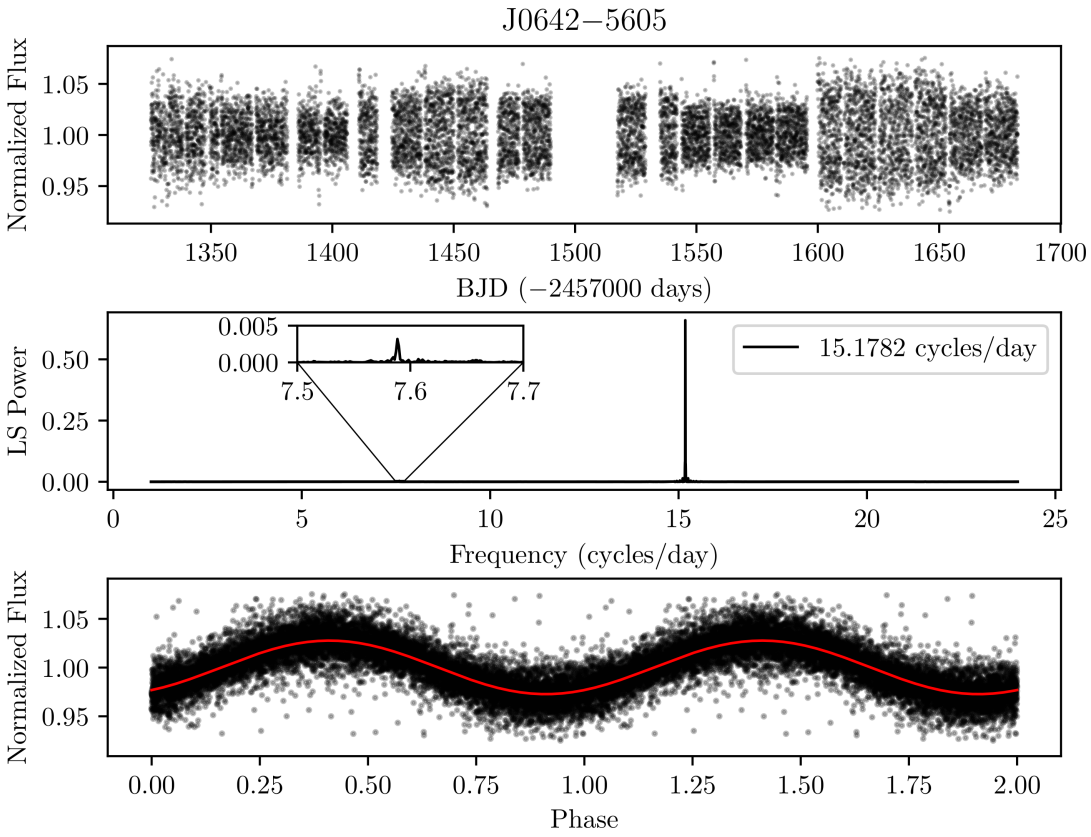

Fig. 4.13.— TESS Light curve (top), Lomb Scargle periodogram (middle), and phase folded light curve (bottom) of J0642−5605. We include a zoomed inset plot showing the region surrounding the small peak at the orbital period of the system. We overplot the best-fit frequency model onto the phase folded light curve for clarity.

system presented here, and the observed variability in the TESS data does not match the orbital period (11.3 cycles per day), and is likely caused by contamination from neighboring sources in the TESS images.

J1239−2041

J123950.37−204142.28 has a best-fit atmosphere solution of $\log g = 7.03 \pm 0.04$ and $T_{\rm eff}$ = 17,750 ± 210 K (Figure 4.10). We obtained six spectra of J1239−2041 over three nights and measure significant radial velocity variations. However, due to significant period aliasing, additional follow-up is required to constrain the orbit and determine companion mass and merger time. Based on the Istrate et al. (2016) He-Core ELM white dwarf models, J1239−2041 is a 0.30 ± 0.01 $M_\odot$ He-core white dwarf. TESS full-frame images on J1239−2041 do not reveal any significant photometric variability.

4.3.2 Survey Efficiency

We observed 82 unique systems using our Gaia parallax target selection method. Of these 82 systems, six contain an ELM white dwarf based on stellar atmosphere fits. We confirmed all six of these to be in compact binary systems and obtained precise orbital periods for four systems, two of which will merge within a Hubble time.

Figure 4.14 shows a $\log g$ vs $T_{\rm eff}$ plot of the objects fit with Hydrogen atmospheres and $\log g > 5.0$. Black points are objects observed in this survey, identified through Gaia parallax. Red stars mark the location of the six new ELM systems identified through Gaia parallax. Blue stars mark the locations of the two new ELM white dwarfs identified in our ATLAS + SkyMapper color selection discussed earlier in this work. Purple points

mark the locations of the ELM white dwarfs previously published in the ELM Survey. We overlay the Istrate et al. (2016) 0.2 $M_{\odot}$ (light blue) and 0.3 $M_{\odot}$ (purple) He-core ELM white dwarf evolutionary tracks, Helium main-sequence (HeMS, silver dashed line) and Zero-Age Extreme-Horizontal Branch (ZAEHB, gold dashed line) for reference.

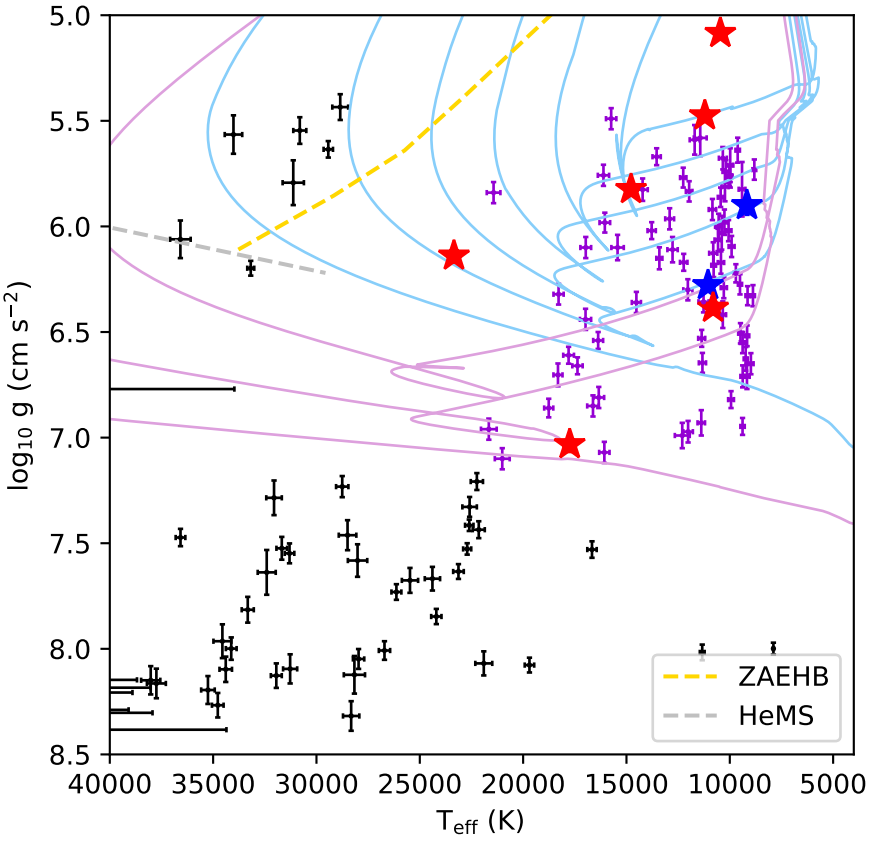

Fig. 4.14.— log(g) vs T_{eff} plot of the 82 systems observed through our Gaia parallax selection. Red stars represent of the six ELM systems identified from our Gaia parallax selection. Blue stars represent two new ELMs identified from our ATLAS+SkyMapper color selection. Purple points show the locations of previously published ELM WDs from the ELM Survey. Evolutionary tracks for 0.205 $M_{\odot}$ (light blue) and 0.306 $M_{\odot}$ (purple) ELM WDs from Istrate et al. (2016) are overplotted. Hydrogen shell flashes cause loops seen in the model tracks. The silver and gold dashed lines show the locations of the Helium main sequence (HeMS) and zero-age extreme-horizontal branch (ZAEHB).

Table 4.2:: The physical parameters of the eight new ELM WDs identified in this work. Targets marked with a ⋆ are also included in Pelisoli & Vos (2019) as ELM WD candidates.

Gaia Source ID	Object	R.A.	Dec.	Gaia G (mag)	Gaia Parallax (mas)	$T_{\rm eff}$ (K)	$\log g$ (cgs)	$M_{\rm WD}$ ($M_\odot$)
3680368505418792320	J1236−0444	12:36:19.70	−04:44:37.90	17.29	1.91±0.12	11100±110	6.28±0.02	0.156±0.01
6308188582700310912	J1514−1436	15:14:47.26	−14:36:26.77	18.27	0.57±0.22	9170±30	5.91±0.05	0.167±0.01
3183166667278838656	J0500−0930 ⋆	05:00:51.80	−09:30:56.98	12.62	13.97±0.05	10810±40	6.39±0.02	0.163±0.01
2989093214186918784	J0517−1153 ⋆	05:17:24.97	−11:53:25.85	16.22	1.56±0.06	14780±70	5.82±0.02	0.179±0.01
5496812536854546432	J0642−5605 ⋆	06:42:07.99	−56:05:47.44	15.26	1.42±0.03	10460±70	5.08±0.02	0.182±0.01
5503089133341793792	J0650−4925 ⋆	06:50:51.48	−49:25:49.46	17.07	0.96±0.06	11210±90	5.47±0.03	0.182±0.01
5195888264601707392	J0930−8107 ⋆	09:30:08.47	−81:07:38.32	16.25	1.17±0.04	23350±120	6.14±0.02	0.238±0.01

Continued on next page

Table 4.2 – continued from previous page

Gaia Source ID	Object	R.A.	Dec.	Gaia G (mag)	Gaia Parallax (mas)	T_{eff} (K)	$\log g$ (cgs)	M_{WD} ($M_\odot$)
3503613283880705664	J1239−2041	12:39:50.37	−20:41:42.28	18.98	1.41±0.33	17750±210	7.03±0.04	0.305±0.01

In addition to the six new ELM systems, we identify 49 white dwarfs (Table 4.6), 20 of which are low-mass ($0.3M_{\odot} \leq M_{WD} \lesssim 0.5M_{\odot}$), seven subdwarf B stars (Table 4.7), and four emission-line systems. We present the spectra of the emission line systems in the appendix (Figure 4.15). We note that 37 of the 49 white dwarfs in Table 4.6 are hotter than 25,000 K, the upper limit of our target selection criterion. We believe this is due to issues with extinction correction applied to the Gaia DR2 photometry. With issues in extinction correction, it is not surprising that we are finding a large number of hot white dwarfs contaminating our sample. The reduced spectra used for atmosphere and orbital fitting for all targets published here is archived in Zenodo[1] in `FITS` format (Kosakowski et al., 2020b).

Our updated selection method, based on Gaia DR2 parallax measurements, identified six new ELM white dwarfs and 20 low-mass white dwarfs within only 82 targets, while excluding subdwarf type-A stars which heavily contaminated our ATLAS and SkyMapper selection.

4.4 Summary and Conclusions

We present the results from a targeted survey for ELM white dwarfs in the southern sky using two different techniques. Prior to the Gaia DR2, we relied on photometry from the VST ATLAS and SkyMapper surveys to select blue stars with low-surface gravity. We note that the VST ATLAS DR4, released April 2019, offers an improved calibration based on Gaia photometry and a larger southern sky footprint over DR2+DR3 used in our survey. Similar to VST ATLAS DR4, SkyMapper DR2 provides not only an extended southern

[1]http://doi.org/10.5281/zenodo.3635104

sky footprint, but deeper photometry in the $uvgriz$ bands with limiting magnitudes of about 19 mag in the g and r filters.

With the release of Gaia DR2 astrometry, we developed a new target selection method using Gaia parallax measurements and tested it in March 2019 using 82 objects. We identified six new ELM white dwarf binary systems and 20 additional systems with $M < 0.5 M_{\odot}$, which correspond to $\sim 7\%$ and $\sim 32\%$ efficiency for ELM and low-mass white dwarfs with $M < 0.5 M_{\odot}$, respectively. In total, we identified eight new ELM white dwarf systems, and constrained the orbital parameters for six of these systems, three of which will merge within 4 Gyr. We present a summary of the physical and orbital parameters for these eight new ELM white dwarf systems in Tables 4.2 and 4.3, respectively.

While it appears that Gaia parallax is an efficient method for targeting ELM white dwarfs, we note that Pelisoli & Vos (2019) have created a target list of 5672 (including 2898 with Dec$< 0°$) ELM white dwarf candidates based on Gaia colors and astrometry with no restrictions on reddening. Five of our eight new ELM white dwarf systems are also included in Pelisoli & Vos (2019) as ELM white dwarf candidates, but three are missing from their catalog as Pelisoli & Vos (2019) applied stricter cuts to create their catalog. In addition to these five ELM systems, 27 of our other targets with SOAR spectra were also included in Pelisoli & Vos (2019). Almost all of these are normal DA white dwarfs or sdB stars, indicating a non-negligible contamination of their ELM candidate list.

Table 4.3:: Orbital parameters for the six new binaries identified in this work. Radial velocity measurements for all targets are presented in the Appendix. Targets marked with a ⋆ are also included in Pelisoli & Vos (2019) as ELM WD candidates.

Object	$P_{\rm Orbital}$ (d)	$M_{2,\rm min}$ (km s^{-1})	$\tau_{\rm max}$ ($M_\odot$)	(Gyr)
J1236−0444	0.68758±0.00327	138.0±6.6	0.37±0.04	···
J1514−1436	0.58914±0.00244	187.7±6.6	0.63±0.06	···
J0500−0930 ⋆	0.39435±0.00001	146.8±8.3	0.30±0.04	···
J0642−5605 ⋆	0.13189±0.00006	368.0±27.0	0.96±0.17	1.3
J0650−4925 ⋆	0.17453±0.00028	284.2±39.4	0.67±0.21	3.6
J0930−8107 ⋆	0.08837±0.00005	212.0±9.0	0.29±0.03	0.9

The shortest period ELM white dwarf binaries will serve as multi-messenger laboratories as they are detected by the Laser Interferometer Space Antenna (LISA). Hence, the discovery of additional systems now is important for characterizing such systems before LISA is operational. We are continuing to observe our remaining catalogue based on our Gaia selection and, along with the eclipsing and tidally distorted ELM white dwarf discoveries from the Zwicky Transient Facility (see Burdge et al., 2019b) and the upcoming Large Synoptic Survey Telescope, we hope to significantly increase the known

population of ELM white dwarfs in the next few years

4.5 Acknowledgements

We thank the anonymous referee for helpful comments and suggestions that greatly improved the quality of this work. This work was supported in part by the Smithsonian Institution, and in part by the NSF under grant AST-1906379. This project makes use of data obtained at the Southern Astrophysical Research (SOAR) telescope, which is a joint project of the Ministério da Ciência, Tecnologia, Inovações e Comunicaçãoes do Brasil, the U.S. National Optical Astronomy Observatory, the University of North Carolina at Chapel Hill, and Michigan State University. This research made use of Astropy,[2] a community-developed core Python package for Astronomy (Astropy Collaboration et al., 2013, 2018).

4.6 Facilities

MMT (Blue Channel spectrograph), FLWO:1.5m (FAST spectrograph), SOAR (Goodman spectrograph), Magellan (MagE)

4.7 Appendix

4.7.1 Additional Systems: Emission Line Objects

Among all of the systems observed throughout our survey, we identified a handful of emission line systems. For completeness, here we display the optical spectrum for these

[2]http://www.astropy.org

four objects (Figure 4.15). J0409−7117 (Figure 4.15, top) shows evidence of an accretion disk in its Balmer and metal (e.g., Mg) emission lines. J0409−7117 was identified as a CV or WD+M candidate by Pelisoli & Vos (2019). One of these emission line objects, J1358−3556 (Figure 4.15, bottom), shows variability at a frequency of 12.3 cycles per day in the TESS full-frame images. J1358−3556 was also identified as a CV or WD+M candidate by Pelisoli & Vos (2019). There are two additional targets in our sample that show variability in TESS data. J0950−2511 is a low-mass white dwarf with an estimated mass of $M = 0.44 \pm 0.02 M_{\odot}$, but with weak Balmer emission lines visible in the line cores. The Catalina Sky Survey found variations with a period of 0.318654 d (Drake et al., 2017), and TESS full-frame images also show variability at the same period. In addition, J0711−6727 shows significant variations at a frequency of 4.86 cycles per day. Follow-up spectroscopy would be useful to constrain the nature of variability in these systems.

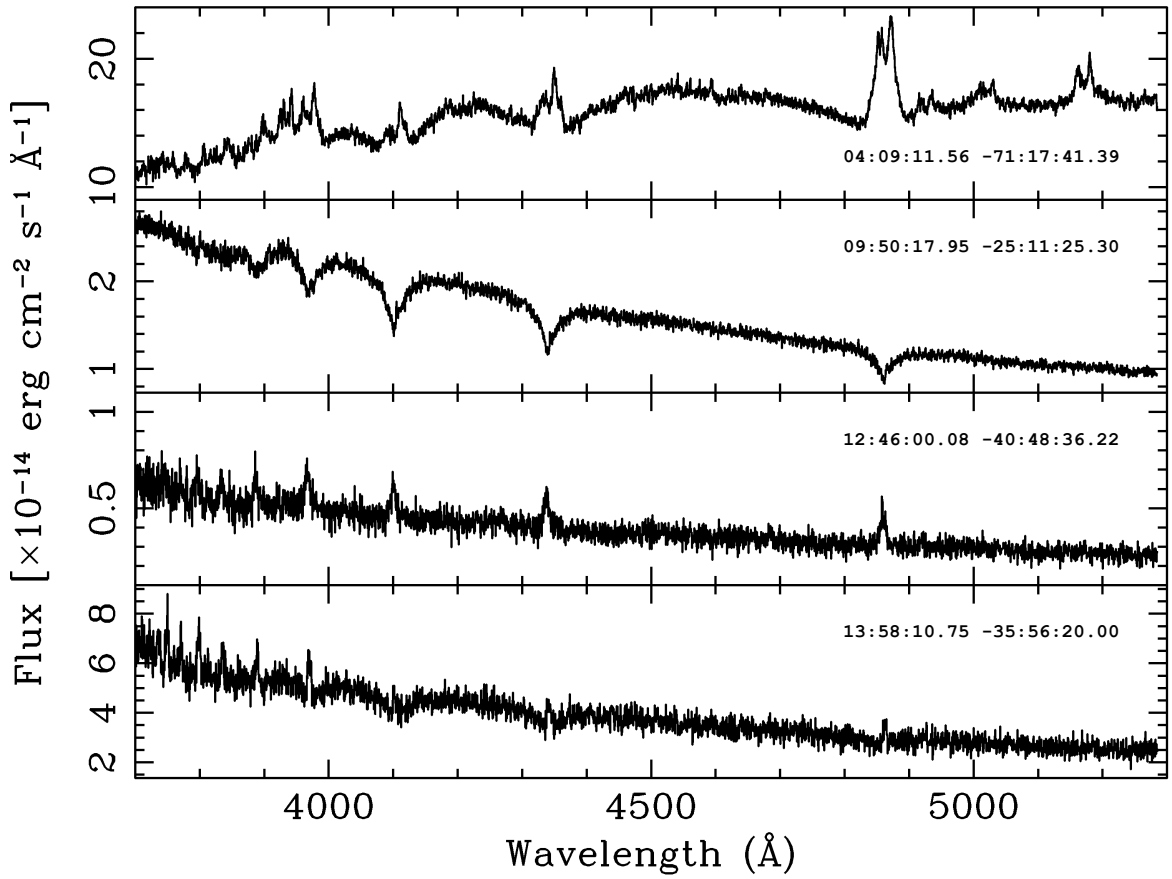

Fig. 4.15.— Spectra of emission line objects observed as a part of the ELM Survey South: I. Hydrogen emission lines can be seen in the core of broad Balmer lines in all objects. J0409−7117 shows multi-peaked Hydrogen and Metal emission lines. J0950−2511 shows faint emission lines systematically offset towards the red wing of Balmer line cores. Both J0409−7117 and J1358−3556 were identified as CV or WD+M candidates by Pelisoli & Vos (2019).

Table 4.4:: Table of 123 white dwarfs observed as a part of our ATLAS+SkyMapper target selection. Targets marked with a ⋆ are also included in Pelisoli & Vos (2019) as ELM WD candidates. Targets marked with a ‡ are also included in Gentile Fusillo et al. (2017) catalogue of VST ATLAS white dwarfs candidates.

Gaia Source ID	Object	R.A.	Dec.	Gaia G (mag)	Gaia Parallax (mas)	T_{eff} (K)	log g (cgs)	M_{WD} ($M_\odot$)
2314720431736648960	J0000−3102	00:00:41.06	−31:02:45.82	20.05	2.95±1.43	13810±1950	7.90±0.16	0.55±0.09
2421224556841719680	J0001−1218	00:01:17.04	−12:18:42.66	20.09	2.28±0.86	12680±1660	8.98±0.21	1.19±0.09
2427460643197388672	J0011−1143	00:11:04.66	−11:43:49.98	17.08	0.25±0.11	11910±330	8.25±0.08	0.76±0.06
2316638774585068672	J0021−3154	00:21:40.44	−31:54:42.44	18.53	0.73±0.27	11250±380	8.02±0.14	0.62±0.09
2318640465567548800	J0024−2933	00:24:29.67	−29:33:38.45	19.88	3.13±0.78	10030±190	7.95±0.16	0.57±0.09

Continued on next page

Table 4.4 – continued from previous page

Gaia Source ID	Object	R.A.	Dec.	Gaia G (mag)	Gaia Parallax (mas)	T_{eff} (K)	$\log g$ (cgs)	M_{WD} ($M_\odot$)
2424786459119647104	J0024−1107	00:24:54.96	−11:07:43.28	19.46	2.86±0.62	13510±910	7.96±0.12	0.59±0.07
2315815721412502656	J0026−3224 ‡	00:26:06.30	−32:24:23.77	17.05	9.09±0.10	13160±810	8.42±0.11	0.87±0.08
2319211352620639616	J0030−2803	00:30:53.20	−28:03:36.11	19.90	2.31±0.63	12010±450	8.69±0.09	1.04±0.06
2346428148058537856	J0035−2627	00:35:49.84	−26:27:19.84	19.55	2.18±0.49	11490±420	8.33±0.12	0.81±0.08
2370382902950807296	J0036−1657	00:36:25.85	−16:57:18.50	15.79	0.17±0.08	9940±200	7.12±0.28	0.28±0.07
2343867935233173376	J0041−2609	00:41:18.62	−26:09:11.88	19.88	2.73±0.61	13640±770	8.11±0.11	0.68±0.07
5005923029327350656	J0047−3425	00:47:28.14	−34:25:35.47	19.64	2.49±0.47	13600±1850	7.84±0.17	0.52±0.09
2474049699645450368	J0049−0913	00:49:44.65	−09:13:14.23	20.30	1.53±0.81	15350±3660	8.50±0.21	0.93±0.13
2473843786029439104	J0052−0924 ‡	00:52:15.36	−09:24:18.71	15.42	15.69±0.06	13930±1950	7.95±0.16	0.58±0.09
2473096358640407168	J0102−1015	01:02:16.05	−10:15:04.18	16.76	7.08±0.08	18520±1010	7.74±0.18	0.49±0.09

Continued on next page

Table 4.4 – continued from previous page

Gaia Source ID	Object	R.A.	Dec.	Gaia G (mag)	Gaia Parallax (mas)	T_{eff} (K)	$\log g$ (cgs)	M_{WD} ($M_\odot$)
2456134364556362624	J0112−1338 ‡	01:12:15.54	−13:38:02.87	20.17	0.70±0.92	26070±630	7.55±0.09	0.46±0.03
5029203259605424512	J0119−3002	01:19:33.67	−30:02:02.62	19.31	1.31±0.39	13100±980	7.74±0.16	0.47±0.08
5014943044766189312	J0134−3422	01:34:59.92	−34:22:31.87	19.30	4.48±0.32	11840±750	8.41±0.17	0.86±0.11
4969151267391273728	J0158−3430	01:58:11.12	−34:30:40.50	19.41	2.34±0.37	14990±2200	8.41±0.14	0.87±0.09
2461668030485282432	J0204−1024	02:04:10.06	−10:24:36.72	19.60	2.11±0.62	11430±440	7.84±0.18	0.52±0.10
4969649621036866688	J0205−3319	02:05:10.90	−33:19:16.61	19.69	2.36±0.38	13770±1500	8.04±0.17	0.63±0.10
4970933580036041216	J0208−3328 ⋆	02:08:13.49	−33:28:11.46	18.92	1.56±0.25	13530±1420	7.87±0.15	0.54±0.08
4970170445950131456	J0214−3344	02:14:21.85	−33:44:21.44	18.31	−0.13±0.16	12400±440	8.18±0.10	0.72±0.07
5150847728544652416	J0217−1133 ‡	02:17:43.89	−11:33:08.15	17.09	9.67±0.11	15120±2670	8.55±0.17	0.96±0.11
5176077603391562752	J0217−0939	02:17:45.97	−09:39:53.86	19.34	3.18±0.64	13790±1980	8.08±0.23	0.66±0.14

Continued on next page

Table 4.4 – continued from previous page

Gaia Source ID	Object	R.A.	Dec.	Gaia G (mag)	Gaia Parallax (mas)	T_{eff} (K)	$\log g$ (cgs)	M_{WD} ($M_\odot$)
4970619149773451136	J0219−3239	02:19:51.61	−32:39:55.37	20.01	1.73±0.55	14420±1770	8.18±0.12	0.72±0.08
5066933619588166400	J0221−3113	02:21:28.37	−31:13:10.52	19.80	1.47±0.44	15940±750	8.13±0.12	0.69±0.08
5050702285341454336	J0249−3328	02:49:58.92	−33:28:30.22	20.01	2.79±0.50	11930±400	8.02±0.12	0.62±0.08
5072652523161819776	J0256−2632	02:56:39.12	−26:32:34.55	18.15	0.37±0.17	14050±950	7.77±0.12	0.49±0.06
5165709277461403520	J0310−1129	03:10:27.67	−11:29:15.72	20.18	2.23±0.89	13600±1030	7.42±0.19	0.38±0.07
5073564636776148992	J0314−2539	03:14:30.95	−25:39:27.29	19.88	1.72±0.46	13800±1610	7.98±0.15	0.60±0.09
5156216368944753024	J0314−1326	03:14:33.00	−13:26:58.88	20.29	1.12±1.27	12780±1240	7.85±0.32	0.52±0.17
5053174743394426496	J0322−3422	03:22:57.76	−34:22:00.80	19.82	1.52±0.45	13780±720	8.47±0.09	0.91±0.06
5161187535892016768	J0324−1346	03:24:09.35	−13:46:24.31	19.74	−3.25±1.11	15130±810	7.65±0.16	0.45±0.07
5060865792871440384	J0327−2632	03:27:41.16	−26:32:31.56	20.22	1.89±0.61	11270±400	8.25±0.14	0.76±0.09

Continued on next page

Table 4.4 – continued from previous page

Gaia Source ID	Object	R.A.	Dec.	Gaia G (mag)	Gaia Parallax (mas)	T_{eff} (K)	$\log g$ (cgs)	M_{WD} ($M_\odot$)
4863642926160372608	J0343−3137	03:43:25.14	−31:37:35.65	19.89	0.84±0.47	11920±480	7.57±0.22	0.41±0.09
5085310758152519680	J0343−2442	03:43:28.21	−24:42:43.52	19.44	2.22±0.36	12480±410	7.87±0.11	0.53±0.06
5114162179486492800	J0343−1318	03:43:28.70	−13:18:16.00	16.33	10.61±0.08	13780±920	8.03±0.10	0.63±0.06
3194415427145350656	J0351−0927	03:51:24.91	−09:27:42.26	19.65	1.86±0.63	18450±830	7.70±0.15	0.47±0.07
3193341857120018304	J0353−1110 ‡	03:53:26.14	−11:10:47.39	16.08	8.29±0.07	18010±880	8.03±0.15	0.64±0.09
5093664194662891776	J0353−2123	03:53:59.40	−21:23:21.52	19.51	1.23±0.43	13360±1120	7.76±0.12	0.48±0.06
4886897352272683008	J0357−3026	03:57:21.79	−30:26:30.73	19.89	2.69±0.44	14390±1940	8.13±0.14	0.69±0.09
4883110428068169472	J0401−3332	04:01:17.81	−33:32:05.28	19.18	2.92±0.26	12740±500	7.79±0.14	0.49±0.07
5686477223197435776	J1002−1445	10:02:27.13	−14:45:37.76	19.41	3.73±0.96	14080±1310	8.03±0.10	0.63±0.06
5686544568284108416	J1007−1430	10:07:17.01	−14:30:58.36	20.40	3.17±0.90	15300±1090	8.27±0.10	0.78±0.07

Continued on next page

Table 4.4 – continued from previous page

Gaia Source ID	Object	R.A.	Dec.	Gaia G (mag)	Gaia Parallax (mas)	$T_{\rm eff}$ (K)	$\log g$ (cgs)	$M_{\rm WD}$ ($M_\odot$)
3768573016120952832	J1017−0940	10:17:56.48	−09:40:18.41	19.59	3.06±0.79	12450±670	8.22±0.14	0.74±0.09
3779023285732532736	J1018−0524	10:18:12.22	−05:24:47.45	19.86	2.56±1.15	14700±1030	8.02±0.12	0.62±0.07
3768136711868126208	J1021−0946	10:21:12.12	−09:46:09.66	20.30	···	11040±280	8.26±0.11	0.77±0.08
3768242505503031552	J1021−0908 ‡	10:21:22.59	−09:08:38.33	18.83	3.75±0.40	13830±710	8.01±0.07	0.62±0.05
3861429723729285376	J1021+0543	10:21:53.13	+05:43:22.37	19.67	1.36±0.60	9600±50	7.54±0.04	0.40±0.02
3769160528992333824	J1022−0808	10:22:59.07	−08:08:20.22	19.80	4.49±1.77	13030±750	8.21±0.13	0.74±0.09
3781985683590564736	J1023−0251 ‡	10:23:39.00	−02:51:23.24	17.07	3.27±0.16	30630±1170	7.54±0.22	0.46±0.08
3749062659027515904	J1026−1538	10:26:02.02	−15:38:38.29	20.29	···	14330±1350	8.20±0.10	0.73±0.07
3755961063699688448	J1029−1002	10:29:10.41	−10:02:47.83	19.70	3.33±0.59	13490±1570	7.81±0.15	0.51±0.08
3748932298180213504	J1033−1537	10:33:08.66	−15:37:14.20	18.23	3.29±0.26	13380±1310	7.76±0.14	0.48±0.07

Continued on next page

Table 4.4 – continued from previous page

Gaia Source ID	Object	R.A.	Dec.	Gaia G (mag)	Gaia Parallax (mas)	$T_{\rm eff}$ (K)	$\log g$ (cgs)	$M_{\rm WD}$ ($M_\odot$)
3781482309128453760	J1038−0248 ‡	10:38:32.71	−02:48:41.30	17.22	6.66±0.15	14110±1040	8.07±0.08	0.65±0.05
3762701108633074688	J1040−0746 ⋆‡	10:40:26.09	−07:46:14.97	17.76	2.16±0.16	24670±570	7.60±0.09	0.47±0.04
3802511018765753728	J1045−0212	10:45:54.42	−02:12:29.00	19.19	1.98±0.48	14140±1240	8.29±0.13	0.79±0.09
3761504285930683008	J1047−0919	10:47:19.75	−09:19:00.01	19.63	1.97±0.60	11870±350	8.04±0.10	0.63±0.07
3762845930634843264	J1050−0905 ‡	10:50:21.96	−09:05:11.11	17.81	4.99±0.17	14570±710	8.01±0.08	0.62±0.05
3760440267912519936	J1102−0757 ‡	11:02:11.77	−07:57:53.46	17.92	2.93±0.22	28380±560	8.15±0.10	0.73±0.06
3787385900590991232	J1123−0302 ‡	11:23:18.74	−03:02:48.88	17.26	6.68±0.24	13970±1440	8.11±0.14	0.68±0.09
3591995876813375232	J1132−0822 ‡	11:32:09.43	−08:22:47.89	18.40	4.90±0.30	12740±390	7.99±0.09	0.60±0.06
3793382563994044416	J1133−0222	11:33:23.29	−02:22:28.64	20.40	0.02±1.35	11000±410	8.02±0.18	0.62±0.11
3593234201782795008	J1133−0624	11:33:26.97	−06:24:26.24	20.36	2.30±1.23	13980±1270	8.07±0.11	0.65±0.07

Continued on next page

Table 4.4 – continued from previous page

Gaia Source ID	Object	R.A.	Dec.	Gaia G (mag)	Gaia Parallax (mas)	T_{eff} (K)	$\log g$ (cgs)	M_{WD} ($M_\odot$)
3586969459405663744	J1134−1023	11:34:47.03	−10:23:02.26	19.68	1.73±0.62	16000±430	7.86±0.08	0.54±0.05
3560803316046802432	J1134−1454	11:34:57.05	−14:54:59.54	20.20	0.75±0.83	11470±290	8.28±0.09	0.78±0.06
3593790318443372288	J1137−0523 ‡	11:37:36.90	−05:23:16.67	16.81	6.65±0.12	19600±610	8.20±0.09	0.74±0.06
3595269775762905472	J1156−0648 ‡	11:56:31.41	−06:48:20.80	18.05	3.76±0.19	13310±2020	7.68±0.20	0.45±0.09
3594535198915846784	J1204−0737	12:04:48.44	−07:37:21.07	19.41	2.98±0.41	12480±520	8.08±0.12	0.65±0.08
3582049385389446912	J1205−0826	12:05:45.49	−08:26:41.96	19.81	2.62±0.51	13280±500	8.09±0.09	0.66±0.06
3581918887102403200	J1206−0924	12:06:13.70	−09:24:42.52	19.09	2.48±0.33	11590±190	7.77±0.08	0.48±0.05
3596970101775019392	J1213−0518 ‡	12:13:49.16	−05:18:56.50	18.26	4.05±0.21	14190±990	8.25±0.10	0.76±0.07
3682256405538928512	J1250−0330	12:50:49.69	−03:30:20.91	19.57	3.23±0.43	12160±380	8.01±0.10	0.61±0.06
3682458814461982592	J1254−0218 ‡	12:54:58.08	−02:18:37.77	16.65	8.14±0.12	13410±380	8.30±0.06	0.80±0.05

Continued on next page

Table 4.4 – continued from previous page

Gaia Source ID	Object	R.A.	Dec.	Gaia G (mag)	Gaia Parallax (mas)	$T_{\rm eff}$ (K)	$\log g$ (cgs)	$M_{\rm WD}$ ($M_\odot$)
3635681505303143296	J1316−0510	13:16:27.72	−05:10:26.00	15.83	0.09±0.08	13790±1130	8.37±0.15	0.84±0.10
3656994674918366208	J1350−0424	13:50:53.32	−04:24:36.86	19.72	3.03±0.63	12560±430	8.17±0.09	0.71±0.06
3645049580594224512	J1355−0415	13:55:45.55	−04:15:21.26	19.66	4.09±0.95	13560±1620	7.95±0.20	0.58±0.11
6311053875642748928	J1438−1418	14:38:53.93	−14:18:21.17	19.28	3.23±0.42	15960±520	8.17±0.08	0.72±0.06
6281939426215247872	J1444−1827	14:44:03.97	−18:27:09.58	20.08	2.64±0.81	15270±890	8.03±0.13	0.63±0.08
6337488780874439680	J1450−0451	14:50:50.24	−04:51:35.78	20.00	···	13020±690	8.30±0.11	0.79±0.08
6310239721642756224	J1454−1440	14:54:21.85	−14:40:29.24	19.98	3.99±0.92	11550±330	8.25±0.09	0.76±0.06
6310532019936081536	J1454−1418	14:54:27.96	−14:18:16.67	20.16	1.72±1.36	11650±310	7.95±0.11	0.58±0.07
6333254531531385088	J1455−0736	14:55:10.25	−07:36:44.24	19.30	2.82±0.50	12280±310	8.00±0.08	0.61±0.05
6337391027418990464	J1457−0423	14:57:49.40	−04:23:07.19	19.56	0.39±0.49	8750±230	8.53±0.24	0.94±0.15

Continued on next page

Table 4.4 – continued from previous page

Gaia Source ID	Object	R.A.	Dec.	Gaia G (mag)	Gaia Parallax (mas)	T_{eff} (K)	$\log g$ (cgs)	M_{WD} ($M_\odot$)
6310291398688877312	J1459−1433	14:59:28.15	−14:33:26.10	20.05	···	14740±1090	8.06±0.11	0.65±0.07
6257011607827666560	J1501−1913	15:01:37.26	−19:13:09.59	19.21	2.86±0.37	12030±400	7.91±0.12	0.56±0.07
6305223680876589952	J1504−1816	15:04:17.22	−18:16:23.05	19.71	2.58±0.48	11260±290	7.86±0.12	0.53±0.07
6322910390561746560	J1519−0530	15:19:19.89	−05:30:56.84	19.98	2.84±0.92	14110±820	7.71±0.12	0.46±0.06
6258275943120737792	J1520−1725	15:20:47.27	−17:25:23.48	19.42	1.86±0.50	19030±700	7.91±0.12	0.57±0.06
6322818753139011712	J1522−0600	15:22:18.42	−06:00:50.72	20.13	2.24±0.73	11520±300	7.51±0.15	0.39±0.06
6321330392351972992	J1522−0743	15:22:40.59	−07:43:49.19	20.18	···	14710±1720	8.50±0.15	0.93±0.10
6266081754122219776	J1528−1407	15:28:13.98	−14:07:58.19	20.49	−0.28±1.21	13220±790	8.33±0.11	0.81±0.08
6842569307021815552	J2129−1357 ‡	21:29:02.60	−13:57:59.00	16.21	7.24±0.12	24180±620	8.12±0.11	0.70±0.07
6810587606146932096	J2138−2822	21:38:22.55	−28:22:01.27	20.16	−0.82±1.16	11370±620	8.11±0.21	0.67±0.13

Continued on next page

Table 4.4 – continued from previous page

Gaia Source ID	Object	R.A.	Dec.	Gaia G (mag)	Gaia Parallax (mas)	T_{eff} (K)	$\log g$ (cgs)	M_{WD} ($M_\odot$)
6816647220885100928	J2145−2256	21:45:12.49	−22:56:22.74	18.04	0.02±0.22	13240±850	7.99±0.16	0.60±0.10
6617354691037040256	J2149−2945	21:49:47.26	−29:45:43.31	17.62	0.15±0.14	13120±740	7.91±0.15	0.56±0.09
6588218560614027392	J2156−3515	21:56:37.62	−35:15:47.34	20.15	2.16±1.09	11400±560	8.87±0.16	1.14±0.08
6812758591855108736	J2200−2400	22:00:22.24	−24:00:21.17	17.88	−0.04±0.20	12320±1170	8.62±0.20	1.00±0.12
6573507576070298880	J2206−3929	22:06:59.42	−39:29:47.54	19.80	1.71±0.79	14300±1500	8.21±0.12	0.74±0.08
6619862642700459904	J2207−2611	22:07:52.86	−26:11:09.90	19.36	3.17±0.50	11390±670	8.43±0.20	0.88±0.13
6618244814419373184	J2212−2828	22:12:14.57	−28:28:49.40	17.08	0.12±0.11	18060±2250	7.64±0.42	0.45±0.18
2601267970982861952	J2230−1250	22:30:28.84	−12:50:51.32	20.34	3.08±1.98	13300±900	7.83±0.13	0.52±0.07
6600835284744283520	J2238−3241 ‡	22:38:43.07	−32:41:28.54	18.36	0.04±0.25	10970±410	8.51±0.16	0.93±0.11
6623866514292772352	J2239−2436	22:39:30.02	−24:36:39.38	17.77	0.12±0.21	10480±300	7.89±0.19	0.54±0.11

Continued on next page

Table 4.4 – continued from previous page

Gaia Source ID	Object	R.A.	Dec.	Gaia G (mag)	Gaia Parallax (mas)	T_{eff} (K)	$\log g$ (cgs)	M_{WD} ($M_\odot$)
6604376158861666560	J2248−3103	22:48:34.39	−31:03:06.48	19.52	2.57±0.63	14200±2750	7.97±0.24	0.59±0.14
6548178264140855424	J2251−3624	22:51:14.68	−36:24:20.02	19.22	1.69±0.38	12780±660	7.58±0.14	0.42±0.06
6609954810278528128	J2254−2721	22:54:03.94	−27:21:15.59	19.76	2.55±0.64	15440±620	7.17±0.14	0.31±0.03
2603274858876574720	J2256−1319 ‡	22:56:13.00	−13:19:39.00	15.68	10.48±0.09	20690±530	7.90±0.08	0.57±0.05
2396582989434764672	J2256−2224	22:56:44.93	−22:24:33.41	20.31	2.39±0.81	12360±430	8.06±0.11	0.64±0.07
2383060130285253632	J2307−2518	23:07:02.01	−25:18:05.90	18.75	−0.33±0.33	10800±380	8.66±0.17	1.02±0.10
2379359556397873664	J2308−2710 ‡	23:08:52.37	−27:10:29.21	16.07	6.24±0.08	17400±640	7.41±0.13	0.39±0.04
6556568740451265152	J2309−3217	23:09:14.85	−32:17:18.31	19.47	2.38±0.43	13800±1740	7.90±0.14	0.55±0.08
2410524453277760640	J2309−1337	23:09:15.58	−13:37:31.80	19.91	2.61±0.62	12310±460	8.77±0.07	1.09±0.05
2379902710847010688	J2312−2605	23:12:03.50	−26:05:57.41	19.22	3.64±0.42	13380±820	8.58±0.10	0.98±0.07

Continued on next page

Table 4.4 – continued from previous page

Gaia Source ID	Object	R.A.	Dec.	Gaia G (mag)	Gaia Parallax (mas)	$T_{\rm eff}$ (K)	$\log g$ (cgs)	$M_{\rm WD}$ ($M_\odot$)
2409194525244964608	J2325−1312	23:25:18.83	−13:12:44.50	19.72	2.01±0.54	13900±1910	7.86±0.17	0.53±0.09
2381034417549322240	J2330−2449	23:30:50.62	−24:49:52.10	20.01	3.83±0.84	15070±820	7.69±0.15	0.46±0.07
2433615060749989760	J2331−1115 ‡	23:31:10.02	−11:15:42.43	17.40	3.72±0.17	22090±1030	7.99±0.15	0.62±0.08
2331020725978650624	J2334−2819	23:34:07.41	−28:19:19.24	18.24	···	12330±470	8.10±0.11	0.67±0.07
2332573098957941376	J2339−2531 ‡	23:39:48.06	−25:31:18.08	17.06	−0.16±0.20	11750±430	8.13±0.12	0.68±0.08
2387052560084561024	J2340−2345	23:40:46.46	−23:45:53.42	19.86	1.85±0.84	10310±340	8.02±0.23	0.61±0.14
2339360418595723264	J2345−2334	23:45:39.19	−23:34:50.63	19.07	4.03±0.48	12610±780	7.94±0.19	0.57±0.11
2328335718583448064	J2349−2743	23:49:16.24	−27:43:26.18	17.62	0.10±0.13	14590±1120	8.47±0.10	0.91±0.07

Table 4.5:: Table of 29 sdA + ELM candidates observed as a part of our ATLAS+SkyMapper target selection. Targets marked with a ‡ are also included in Gentile Fusillo et al. (2017) catalogue of VST ATLAS white dwarfs candidates.

Gaia Source ID	Object	R.A.	Dec.	Gaia G (mag)	Gaia Parallax (mas)	T_{eff} (K)	log g (cgs)
4684237675440128512	J0019−7620	00:19:45.64	−76:20:50.00	16.67	0.05±0.06	7520±70	5.02±0.20
5006336308261344000	J0049−3354	00:49:30.74	−33:54:04.68	16.57	0.13±0.08	8860±50	5.53±0.09
2470088090531076096	J0107−1042	01:07:12.71	−10:42:35.91	20.14	1.38±0.66	9460±43	6.06±1.34
4957677283735582336	J0155−4148	01:55:34.86	−41:48:18.44	15.75	2.08±0.04	10060±70	5.61±0.06
4942238319415762048	J0155−4708	01:55:53.66	−47:08:22.61	16.93	0.07±0.07	9040±40	5.41±0.08
5063798847514778880	J0239−3157	02:39:20.40	−31:57:06.26	15.70	0.14±0.06	8850±50	5.57±0.08

Continued on next page

Table 4.5 – continued from previous page

Gaia Source ID	Object	R.A.	Dec.	Gaia G (mag)	Gaia Parallax (mas)	T_{eff} (K)	log g (cgs)
5048200350928561792	J0313−3406 ‡	03:13:10.01	−34:06:18.11	17.47	0.04±0.10	7940±50	5.06±0.13
4838360480913152768	J0402−4452	04:02:01.05	−44:52:56.01	14.57	0.27±0.04	9010±20	5.51±0.03
3200233905240195968	J0441−0547	04:41:32.62	−05:47:34.93	18.83	0.31±0.29	8640±80	5.27±0.17
3777278773096451712	J1046−0425	10:46:02.98	−04:25:17.51	20.17	−1.27±2.07	8470±90	5.88±0.18
3801357051247738112	J1051−0347	10:51:27.38	−03:47:09.20	18.95	−0.29±0.32	8960±80	5.49±0.13
3599721286026267264	J1144−0450	11:44:20.31	−04:50:10.39	20.01	1.28±0.73	9290±110	5.83±0.29
3595644434349398272	J1159−0633	11:59:35.70	−06:33:46.98	19.38	0.29±0.59	11960±510	5.41±0.16
3628140710962656512	J1308−0733	13:08:57.86	−07:33:56.63	18.35	0.33±0.18	8590±80	6.15±0.16
3643468379794415104	J1404−0634	14:04:40.81	−06:34:26.62	19.79	1.06±0.92	8880±70	5.52±0.11
3644329881514712576	J1405−0455	14:05:44.40	−04:55:19.85	19.65	−0.50±0.79	8990±120	5.53±0.32

Continued on next page

Table 4.5 – continued from previous page

Gaia Source ID	Object	R.A.	Dec.	Gaia G (mag)	Gaia Parallax (mas)	T_{eff} (K)	log g (cgs)
3641707894175473024	J1425−0508	14:25:55.01	−05:08:08.60	16.39	0.25±0.08	8570±10	5.59±0.02
6281296211912043904	J1455−1858	14:55:32.94	−18:58:01.40	17.58	−0.01±0.25	8760±90	5.93±0.14
6305569103622390528	J1500−1727	15:00:01.98	−17:27:39.13	16.29	0.18±0.10	8560±60	5.79±0.10
6332713533156000384	J1503−0750	15:03:22.21	−07:50:24.68	20.33	−0.30±0.88	8590±110	5.48±0.21
6334668842786315648	J1507−0606	15:07:17.86	−06:06:18.22	20.32	0.51±0.82	7720±120	5.52±0.25
6258208494955477888	J1522−1737	15:22:20.54	−17:37:50.56	20.41	−0.17±0.86	9090±140	6.01±0.29
6844758095371132800	J2135−1137	21:35:47.07	−11:37:54.19	15.76	0.27±0.07	8670±50	5.63±0.08
6592840907497444608	J2145−3135	21:45:01.84	−31:35:57.05	18.53	0.31±0.22	7580±80	5.11±0.20
6810469138063674624	J2151−2645	21:51:41.01	−26:45:03.13	18.71	−0.04±0.25	8670±50	5.91±0.07
6587685125675331840	J2153−3630	21:53:01.62	−36:30:03.92	17.12	0.27±0.19	8760±50	5.35±0.11

Continued on next page

Table 4.5 – continued from previous page

Gaia Source ID	Object	R.A.	Dec.	Gaia G (mag)	Gaia Parallax (mas)	T_{eff} (K)	log g (cgs)
6628443918638517632	J2226−2137	22:26:45.58	−21:37:50.23	17.76	−0.03±0.15	8940±60	5.18±0.14
6624542164187962368	J2238−2333	22:38:49.31	−23:33:08.32	18.54	0.32±0.32	11440±820	6.67±0.33
2334416331419048576	J2354−2706	23:54:29.97	−27:06:26.14	20.12	−1.67±0.93	12220±2330	6.99±0.30

Table 4.6:: Table of 49 White Dwarfs identified through our Gaia parallax target selection. Targets marked with a ⋆ are also included in Pelisoli & Vos (2019) as ELM candidates. Targets marked with a ‡ are also included in Gentile Fusillo et al. (2017) catalogue of VST ATLAS white dwarfs candidates. All targets listed here are present in the Gaia DR2 white dwarf catalogue of Gentile Fusillo et al. (2019).

Gaia Source ID	Object	R.A.	Dec.	Gaia G (mag)	Gaia Parallax (mas)	$T_{\rm eff}$ (K)	$\log g$ (cgs)	$M_{\rm WD}$ ($M_\odot$)
4876689387538123008	J0455−2928 ⋆	04:55:35.93	−29:28:58.74	15.03	10.26±0.03	26130±240	7.73±0.04	0.50±0.03
4800596031773794944	J0518−4336	05:18:26.98	−43:36:18.40	18.09	1.04±0.15	42120±4070	8.61±0.08	1.02±0.05
2967020552620016768	J0545−1902	05:45:45.30	−19:02:45.50	17.34	2.46±0.09	22610±200	7.42±0.03	0.41±0.02
5482174218861274624	J0611−6044	06:11:51.46	−60:44:22.86	17.69	2.99±0.21	19690±230	8.08±0.04	0.67±0.03

Continued on next page

Table 4.6 – continued from previous page

Gaia Source ID	Object	R.A.	Dec.	Gaia G (mag)	Gaia Parallax (mas)	T_{eff} (K)	$\log g$ (cgs)	M_{WD} ($M_\odot$)
5550454165824297856	J0619−4942	06:19:04.95	−49:42:37.20	18.49	1.06±0.15	41850±3170	8.15±0.07	0.76±0.05
5555707774117176192	J0631−4541	06:31:44.74	−45:41:22.20	18.07	2.09±0.14	34780±280	8.27±0.06	0.81±0.04
5484929251404350592	J0652−5630 ⋆	06:52:56.74	−56:30:46.40	18.45	1.70±0.15	27960±270	8.05±0.05	0.67±0.04
5483936186245586432	J0700−5711	07:00:56.49	−57:11:01.60	18.58	1.52±0.17	24390±370	7.67±0.06	0.47±0.03
5281105393618729600	J0711−6727	07:11:01.22	−67:27:25.20	18.23	1.52±0.13	38020±460	8.15±0.07	0.75±0.05
5288476833106664064	J0727−6352	07:27:28.80	−63:52:17.20	18.31	1.63±0.12	37750±460	8.16±0.07	0.76±0.05
5210251837830078208	J0831−7717 ⋆	08:31:14.84	−77:17:37.40	18.07	1.26±0.11	41720±3700	8.18±0.09	0.78±0.06
5761818336913460096	J0847−0424	08:47:47.66	−04:24:48.50	18.38	1.81±0.19	23130±260	7.63±0.04	0.47±0.02
5196645102262353152	J0902−8034 ⋆	09:02:52.09	−80:34:52.80	18.56	1.33±0.15	32410±440	7.64±0.11	0.49±0.04
5660008787157868928	J0950−2511 ⋆	09:50:17.95	−25:11:25.30	15.53	3.16±0.06	36580±230	7.47±0.04	0.44±0.02

Continued on next page

Table 4.6 – continued from previous page

Gaia Source ID	Object	R.A.	Dec.	Gaia G (mag)	Gaia Parallax (mas)	T_{eff} (K)	$\log g$ (cgs)	M_{WD} ($M_\odot$)
5688043614950782848	J0955−1209 ⋆	09:55:58.27	−12:09:37.30	17.89	2.16±0.22	26710±270	8.01±0.04	0.64±0.03
3752200596493839232	J1024−1434 ⋆‡	10:24:32.21	−14:34:20.50	16.84	2.54±0.17	22240±300	7.21±0.04	0.36±0.01
3762701108633074688	J1040−0746 ⋆‡	10:40:26.09	−07:46:14.97	17.76	2.16±0.16	22710±200	7.53±0.03	0.43±0.02
3565938482025538944	J1111−1213 ‡	11:11:14.66	−12:13:11.20	18.43	1.01±0.26	28750±300	7.23±0.05	0.39±0.01
5397661047866038400	J1124−3752	11:24:55.89	−37:52:28.30	18.12	1.92±0.18	34390±300	8.10±0.06	0.71±0.04
3480932145705503616	J1149−2852 ⋆	11:49:51.97	−28:52:39.70	18.17	1.99±0.18	16670±230	7.53±0.04	0.42±0.02
3695067154816052736	J1222−0106	12:22:06.38	−01:06:36.20	18.37	1.84±0.23	28160±510	8.12±0.09	0.71±0.06
3467973099797096192	J1226−3408	12:26:00.06	−34:08:25.10	18.49	1.12±0.32	22590±350	7.33±0.05	0.40±0.02
6156485046406365568	J1235−3745	12:35:44.76	−37:45:00.00	17.27	2.87±0.15	28010±470	7.58±0.08	0.47±0.03
3707477754875428352	J1239+0514	12:39:32.01	+05:14:07.80	18.43	1.47±0.22	45580±1280	7.94±0.18	0.65±0.09

Continued on next page

Table 4.6 – continued from previous page

Gaia Source ID	Object	R.A.	Dec.	Gaia G (mag)	Gaia Parallax (mas)	T_{eff} (K)	$\log g$ (cgs)	M_{WD} ($M_\odot$)
3504361849435922048	J1307−2207 ⋆	13:07:42.65	−22:07:40.70	17.30	2.06±0.12	34120±260	8.00±0.05	0.66±0.04
3624296749592496768	J1312−1025 ‡	13:12:39.30	−10:25:53.30	18.01	1.78±0.19	24200±250	7.85±0.04	0.55±0.03
6183015574790579328	J1319−2844 ⋆	13:19:07.72	−28:44:07.70	18.36	1.35±0.19	33330±290	7.82±0.06	0.57±0.03
3636151129911425408	J1319−0413 ‡	13:19:09.85	−04:13:14.13	17.44	2.40±0.32	11330±120	8.02±0.04	0.61±0.03
3607395533590721024	J1319−1639	13:19:42.20	−16:39:09.20	18.58	1.57±0.24	28320±400	8.32±0.07	0.57±0.03
3610368033211697024	J1338−1211	13:38:59.68	−12:11:04.20	17.68	1.92±0.16	41710±2810	8.21±0.07	0.79±0.05
6115720618448356736	J1349−3652	13:49:42.74	−36:52:31.90	17.75	1.97±0.20	25480±390	7.68±0.06	0.48±0.03
6290699097913837696	J1355−1946	13:55:41.73	−19:46:31.20	17.74	2.45±0.23	31940±260	8.13±0.06	0.73±0.04
6120865237649732352	J1406−3622	14:06:01.84	−36:22:29.70	16.71	3.77±0.08	21900±410	8.07±0.06	0.67±0.04
6122949361939805184	J1411−3434	14:11:28.59	−34:34:41.20	17.28	2.03±0.13	42430±8080	8.38±0.16	0.89±0.10

Continued on next page

Table 4.6 – continued from previous page

Gaia Source ID	Object	R.A.	Dec.	Gaia G (mag)	Gaia Parallax (mas)	T_{eff} (K)	$\log g$ (cgs)	M_{WD} ($M_\odot$)
6283002069842683392	J1426−2006	14:26:25.06	−20:06:30.70	18.54	0.84±0.48	42150±7540	9.13±0.14	1.27±0.07
6324871678787667968	J1436−1106	14:36:13.35	−11:06:48.19	17.79	1.58±0.26	22150±290	7.44±0.04	0.41±0.02
6284835750296054784	J1436−1845	14:38:58.74	−18:45:42.70	16.59	3.08±0.12	42400±5400	8.88±0.08	1.16±0.04
6338239094480660608	J1442−0352 ‡	14:42:55.33	−03:52:10.70	17.27	2.92±0.13	35250±330	8.20±0.07	0.77±0.05
6227876645636436352	J1503−2348 ⋆	15:03:55.16	−23:48:27.70	18.12	1.22±0.19	34550±430	7.96±0.08	0.64±0.05
6318961082233123456	J1507−1028 ⋆	15:07:28.33	−10:28:59.10	18.21	1.03±0.20	31300±230	7.55±0.05	0.46±0.02
6253056939379854976	J1518−2047	15:18:04.69	−20:47:01.80	18.57	1.35±0.78	41780±7810	6.77±0.22	0.28±0.05
6243072519105238272	J1611−2117	16:11:31.51	−21:17:37.60	17.27	2.13±0.14	32050±380	7.29±0.08	0.40±0.03
4334088989163587200	J1645−1127	16:45:37.40	−11:27:54.60	18.09	1.96±0.18	42190±7910	8.76±0.13	1.10±0.07
5766955358317857280	J1650−8614	16:50:45.73	−86:14:35.90	16.52	2.93±0.07	31680±260	7.52±0.05	0.46±0.02

Continued on next page

Table 4.6 – continued from previous page

Gaia Source ID	Object	R.A.	Dec.	Gaia G (mag)	Gaia Parallax (mas)	T_{eff} (K)	$\log g$ (cgs)	M_{WD} ($M_\odot$)
4385335984889341696	J1655+0306 ⋆	16:55:54.57	+03:06:11.40	16.60	2.54±0.08	44410±1130	7.57±0.13	0.50±0.05
4381363208860631296	J1700+0044 ⋆	17:00:08.87	+00:44:36.30	18.45	1.26±0.21	31270±340	8.10±0.07	0.61±0.05
4392410380142049792	J1700+0512 ⋆	17:00:56.61	+05:12:54.60	17.59	1.81±0.12	42080±4150	8.30±0.08	0.85±0.05
4390681746002706176	J1726+0601	17:26:31.37	+06:01:00.90	16.09	3.63±0.10	41960±2870	8.29±0.06	0.84±0.04
4389028630270429440	J1728+0354	17:28:18.00	+03:54:55.30	16.61	3.27±0.09	28500±430	7.46±0.07	0.43±0.03

Table 4.7:: Table of seven sdB stars observed as a part of our Gaia parallax target selection. Atmosphere parameters are based on pure-Hydrogen atmosphere model fits, and should be used with caution. Targets marked with a † are present in the Geier et al. (2019) Gaia hot sub-luminous star catalogue. Targets marked with a ⋆ are present in Pelisoli et al. (2019) as ELM candidates based on Gaia colors.

Gaia Source ID	Object	R.A.	Dec.	Gaia G (mag)	Gaia Parallax (mas)	T_{eff} (K)	log g (cgs)
5453140446099189120	J1054−2941	10:54:53.64	−29:41:10.24	17.01	0.48±0.10	34020±420	5.57±0.09
3548810053666523904	J1137−1447 †⋆	11:37:26.73	−14:47:57.10	16.35	0.86±0.11	29430±230	5.64±0.04
3470421329940244608	J1231−3104 †	12:31:29.71	−31:04:31.20	18.45	1.15±0.28	31120±520	5.79±0.11
6173348947732101504	J1359−3054	13:59:17.78	−30:54:09.61	16.63	0.94±0.22	30810±320	5.55±0.06

Continued on next page

Table 4.7 – continued from previous page

Gaia Source ID	Object	R.A.	Dec.	Gaia G (mag)	Gaia Parallax (mas)	T_{eff} (K)	log g (cgs)
6322166948902534016	J1517−0706 †	15:17:59.87	−07:06:02.80	18.09	0.91±0.27	36580±500	6.06±0.09
6322703991612652160	J1523−0609 †	15:23:51.71	−06:09:35.40	18.59	1.55±0.45	28850±380	5.44±0.06
4353523544382401408	J1648−0447 †⋆	16:48:06.27	−04:47:25.30	15.51	1.30±0.06	33180±170	6.20±0.04

Table 4.8:: Radial velocity data.

Object	HJD (−2450000 d)	v_{helio} (km s^{-1})
J0500−0930	8401.926694	−186.75 ± 13.65
···	8457.747110	61.62 ± 12.35
···	8457.750212	87.93 ± 17.82
···	8457.752365	64.62 ± 11.47
···	8457.754518	74.18 ± 7.99
···	8457.756659	71.84 ± 12.02
···	8457.759159	53.42 ± 9.72
···	8457.763418	61.53 ± 13.60
···	8457.765744	42.45 ± 10.87
···	8457.768071	36.62 ± 11.64
···	8457.770224	26.41 ± 8.28
···	8457.772376	38.68 ± 11.72
···	8457.775386	29.18 ± 15.14
···	8457.777701	25.29 ± 12.01
···	8457.779853	27.02 ± 16.79
···	8457.782006	44.66 ± 21.64
···	8457.784159	28.22 ± 16.39

Continued on next page

Table 4.8 – continued from previous page

HJD	Velocity (−2450000 d)	Error (km s^{-1})
···	8457.787226	9.46 ± 11.72
···	8457.789552	−20.99 ± 17.46
···	8457.792052	−5.07 ± 15.14
···	8457.795073	−12.70 ± 13.12
···	8457.798094	−18.85 ± 15.36
···	8457.803210	−33.28 ± 8.90
···	8457.808140	−26.66 ± 14.57
···	8457.813418	−42.91 ± 11.08
···	8457.818349	−78.66 ± 10.61
···	8457.822585	−76.56 ± 8.71
···	8457.827237	−95.39 ± 8.77
···	8457.830779	−87.40 ± 11.60
···	8457.834321	−100.28 ± 13.18
···	8457.837851	−103.77 ± 9.88
···	8457.841393	−112.61 ± 14.57
···	8457.845941	−129.67 ± 11.71
···	8457.849483	−125.85 ± 10.11
···	8457.853025	−132.19 ± 12.94

Continued on next page

Table 4.8 – continued from previous page

HJD	Velocity (−2450000 d)	Error (km s^{-1})
···	8457.856566	−157.25 ± 10.30
···	8457.860096	−170.16 ± 17.74
···	8457.871103	−170.80 ± 8.32
···	8457.877388	−179.44 ± 7.53
···	8457.881624	−183.02 ± 12.54
···	8457.885675	−191.17 ± 10.47
···	8457.891717	−175.41 ± 13.15
···	8463.732241	−29.33 ± 29.10
···	8463.743653	−113.25 ± 17.41
···	8463.754995	−118.16 ± 13.77
···	8463.766153	−139.52 ± 14.72
···	8463.846244	−153.90 ± 28.09
···	8463.880908	−143.56 ± 14.28
···	8483.649329	−5.27 ± 7.39
···	8487.778842	−70.86 ± 16.18
···	8487.877345	−168.87 ± 16.41
···	8543.539722	−130.75 ± 5.38
···	8544.502663	92.41 ± 6.48

Continued on next page

Table 4.8 – continued from previous page

HJD	Velocity (−2450000 d)	Error (km s^{-1})
···	8544.570195	−43.28 ± 6.47
···	8545.505076	−91.40 ± 11.20
···	8545.587750	46.63 ± 7.20
···	8546.509416	29.89 ± 5.14
···	8546.556205	−100.47 ± 5.65
J0642−5605	8543.572777	5.44 ± 8.51
···	8544.533324	602.87 ± 5.99
···	8544.582158	125.65 ± 6.20
···	8545.542634	−88.83 ± 7.63
···	8545.569443	310.89 ± 6.79
···	8545.599940	585.30 ± 7.48
···	8545.644891	18.54 ± 5.38
···	8545.687739	102.11 ± 18.99
···	8546.521206	599.44 ± 6.90
···	8546.596143	−104.66 ± 7.31
···	8546.597971	−82.35 ± 7.09
···	8546.599798	−62.04 ± 9.20
···	8546.615714	159.24 ± 8.57

Continued on next page

Table 4.8 – continued from previous page

HJD	Velocity (−2450000 d)	Error (km s^{-1})
···	8546.665951	517.46 ± 8.47
J0650−4926	8543.587096	−134.81 ± 8.78
···	8544.540141	355.19 ± 8.86
···	8544.587890	11.27 ± 6.11
···	8545.549203	211.29 ± 11.40
···	8545.576119	405.68 ± 10.41
···	8545.605456	288.43 ± 13.11
···	8545.649962	−148.42 ± 9.08
···	8545.711134	63.90 ± 26.51
···	8546.527364	−138.46 ± 10.98
···	8546.587008	114.24 ± 11.71
···	8546.589183	139.26 ± 10.67
···	8546.591357	207.90 ± 9.54
···	8546.621214	386.67 ± 13.79
J0930−8107	8543.662882	−160.79 ± 12.12
···	8544.545298	−155.73 ± 15.86
···	8544.592581	147.79 ± 12.36
···	8545.556906	65.29 ± 9.17

Continued on next page

Table 4.8 – continued from previous page

HJD	Velocity (−2450000 d)	Error (km s^{-1})
···	8545.581480	166.37 ± 12.71
···	8545.609496	−190.91 ± 12.01
···	8545.654017	192.66 ± 12.16
···	8546.531874	116.24 ± 17.23
···	8546.575733	−134.02 ± 12.31
···	8546.577908	−112.28 ± 12.64
···	8546.580083	−161.69 ± 13.61
···	8546.604104	−110.32 ± 11.41
···	8546.625537	196.95 ± 16.17
···	8546.804837	194.15 ± 14.42
J1236−0444	7835.658070	194.99 ± 20.79
···	7835.682442	199.69 ± 27.99
···	7835.740827	128.05 ± 26.07
···	7835.800865	−1.00 ± 24.97
···	7835.848070	−11.05 ± 29.47
···	7836.703611	5.86 ± 22.03
···	7836.806389	106.27 ± 24.03
···	7836.809267	97.28 ± 23.08

Continued on next page

Table 4.8 – continued from previous page

HJD	Velocity (−2450000 d)	Error (km s^{-1})
···	7836.858969	140.20 ± 25.13
···	8187.657646	225.69 ± 28.23
···	8187.736842	178.40 ± 25.95
···	8189.750132	226.14 ± 19.57
···	8189.823680	142.52 ± 19.38
···	8190.686871	−38.93 ± 26.37
···	8190.751398	−12.03 ± 25.62
···	8191.652700	184.28 ± 27.53
···	8191.722922	240.31 ± 26.46
J1425−0508	7835.716718	−101.51 ± 13.89
···	7835.772831	−35.31 ± 10.99
···	7835.832876	−82.13 ± 12.91
···	7835.896018	−27.08 ± 11.05
···	7835.899585	−23.59 ± 10.82
···	7836.738278	−26.88 ± 11.12
···	7836.840432	6.98 ± 11.65
···	7836.883911	19.45 ± 11.87
···	7836.908636	25.57 ± 11.91

Continued on next page

Table 4.8 – continued from previous page

HJD	Velocity (−2450000 d)	Error (km s^{-1})
···	7929.652855	11.30 ± 12.25
···	7929.656732	6.36 ± 12.58
···	7929.659856	14.39 ± 12.28
···	7929.661766	27.48 ± 13.07
···	8187.770450	−72.60 ± 18.95
···	8187.830644	−62.10 ± 19.55
···	8187.883105	−59.25 ± 18.67
···	8189.673532	38.96 ± 16.27
···	8189.692531	49.73 ± 15.86
···	8189.755714	40.61 ± 16.27
···	8189.828887	79.22 ± 16.51
···	8189.891552	−32.15 ± 18.23
···	8190.719889	−60.65 ± 17.61
···	8190.786916	−50.04 ± 17.79
···	8191.748295	−55.04 ± 19.08
···	8191.831532	−56.06 ± 17.58
J1514−1436	7835.865608	−25.98 ± 10.77
···	7835.906708	−79.80 ± 20.57

Continued on next page

Table 4.8 – continued from previous page

HJD	Velocity (−2450000 d)	Error (km s^{-1})
···	7835.910275	−47.41 ± 16.12
···	7836.746053	222.44 ± 16.32
···	7836.815246	304.37 ± 11.62
···	7836.845061	283.51 ± 17.56
···	7836.889670	277.96 ± 31.33
···	7931.665442	281.13 ± 20.56
···	8187.837286	171.23 ± 21.55
···	8189.705904	309.81 ± 13.32
···	8189.767503	247.97 ± 17.65
···	8189.841205	187.74 ± 14.23
···	8190.779223	192.88 ± 19.40
···	8190.845175	275.57 ± 22.83
···	8191.761294	−52.28 ± 20.39
···	8191.848146	−61.68 ± 23.68

Chapter 5

Using the Zwicky Transient Facility to identify white dwarfs in binaries

5.1 Introduction

While originally designed as photometric surveys to obtain single exposures of the sky in many filters as a reference for astronomers, astronomical survey science has evolved into a massively-growing subfield used to create a movie of the variable sky. The power of large optical photometric surveys has been previously demonstrated through various programs such as the All Sky Automated Survey for SuperNovae (ASAS-SN; Shappee et al., 2014; Kochanek et al., 2017) the Catalina Real-Time Transient Survey (CRTS; Drake et al., 2009, 2014), the European Space Agency's Gaia mission (Gaia Collaboration et al., 2016), the Sloan Digital Sky Survey (SDSS), the Transiting Exoplanet Survey Satellite (TESS; Ricker et al., 2015), the Palomar Transient Factory (PTF; Law et al., 2009), and, more recently, the Zwicky Transient Facility (ZTF; Bellm et al., 2019; Masci et al., 2019), among many others. Similar to ZTF, future large-scale optical photometric surveys, such as BlackGEM (Groot et al., 2019) and the Vera Rubin Observatory's Legacy Survey of Space and Time (LSST), boast large fields of view and massive data production rates that will require computationally advanced data reduction and analysis techniques to efficiently make use of their data. The LSST is expected to generate about 20 terabytes of raw image data every night and is expected to result in a 20 petabyte catalogue of the southern sky. For comparison, ZTF generates approximately 1 terabyte of raw image data

per night (Masci et al., 2019).

Here we present the results of our search for periodic white dwarf variable systems in the public ZTF data archive through the use of the Box-Least Squares (BLS) period finding algorithm. We first discuss our target selection method and BLS period finding algorithm. We then present our list of identified variable systems, followed by a discussion of our follow-up data collection and data analysis.

5.2 Observations and Data Analysis

5.2.1 Zwicky Transient Facility

The Zwicky Transient Facility (ZTF; Bellm et al., 2019; Masci et al., 2019) is a northern-sky optical survey designed to use the Samuel Oschin 48-inch telescope at the Palomar Observatory to obtain multi-epoch images of the sky above -28 degrees declination in three filters with bandpasses unique to the ZTF instrumentation: g-, r-, and i-bands. Each image taken covers 47-square-degrees of the sky with a median depth of $r \sim 20.6$ mag within a single 30-second exposure. The ZTF data archive is broken up into three groups: the public survey (40%), the private collaboration and partnership programs (40%), and additional programs granted by the Caltech Time Allocation Committee (20%). Our work here was completed with access only to the data made publicly available up to ZTF Data Release 4 (DR4; 2020 November), which includes private collaboration and Caltech data from approximately the first 15 months of operation (2019 March $\sim$ June).

ZTF's main program is to image the entire northern sky above -28 degrees declination every three nights in both the ZTF g and ZTF r band. This survey images $15,000 - 20,000$

square-degrees every 3 nights. The ZTF deep-drilling programs continuously image a single field within the Galactic plane for 1.5 h using 30 s exposures in the ZTF r-band to search for asteroids and other moving objects. In addition to finding moving objects, this deep-drilling program provides excellent sampling for short-period variables.

5.2.2 Target Selection

Gentile Fusillo et al. (2019) have compiled a catalogue of white dwarf candidates within the Gaia DR2 data archive based on Gaia absolute magnitudes, Gaia colors, and numerous Gaia data quality flags. The authors estimate that their catalogue is up to 85% complete for white dwarfs brighter than $G = 20$ mag and with $T_{\rm eff} > 7000$ K at Galactic latitudes $|b| > 20°$. Their catalogue contains a total of 486,641 white dwarf candidates labeled with various flags such as colors, parallax, and probability of being a white dwarf. We selected all objects from this catalogue without performing any cuts. While this selection does increase computation time, it also allows us to prevent excluding binary white dwarf systems whose colors may be heavily influenced by their companion stars.

To deal with high proper motion objects and avoid missing a target due to blending of nearby objects, we queried the public ZTF DR4 data archive for all light curves within 5″ of each of these 486,641 white dwarf candidates. We exclude objects with fewer than 27 measurements and those classified as “bad" data by including the flag BAD_CATFLAGS_MASK=32768 to our query. Because the ZTF astrometry algorithm assigns different object IDs to the same object in different filters, and occasionally the same object in the same filter, we combine data for objects within 2.5“ of one another and normalize their magnitudes to their median ZTF g-band magnitude, or their median ZTF r-band

magnitude if the ZTF g-band data was not available. Additionally, by combining these light curves across multiple filters, we have increased the temporal sampling for each light curve, potentially increasing their light curve phase coverage as a result. This query returned a total of 230,870 combined light curves, some of which are of nearby field stars, unrelated to the white dwarfs in our target list. Finally, because we are specifically searching for eclipsing systems, we remove light curves with fewer than seven 4σ or five 5σ deviant points from the light curve's quiescent level, defined as the the object's light curve after performing three iterations of 3σ clipping around its median magnitude value. Our final sample included 2,498 light curves with magnitudes between 12.8 mag and 20.8 mag (median 18.6 mag) and between 88 and 5740 epochs (median 927 epochs).

5.2.3 The Search for Periodicity with the Box-Least Squares Period Finding Algorithm

The Box Least Squares (BLS; Kovács et al., 2002) period finding algorithm is a powerful method with which to identify transits, or other eclipse-like variability, in time series data. To identify variability, the BLS algorithm folds the data through a set of trial periods and fits a step-function to the folded data with various degrees of binning. The combination of trial-frequency, eclipse duration, and eclipse depth that best-fits the phase-folded data is adopted as the best-fitting solution (see Kovács et al., 2002, for an in-depth discussion on the BLS algorithm). Due to the number of free parameters, the BLS algorithm is relatively computationally expensive.

The BLS period finding algorithm has been utilized to identify many scientifically valuable binary systems in time series data. In recent history: Enenstein et al. (2021)

have used the BLS algorithm to identify 46 HW Virginis eclipsing binary systems in the ZTF data archive. van Roestel et al. (2021) have used the BLS algorithm to identify deeply-eclipsing, potentially substellar, companions to white dwarfs in the ZTF data archive. Burdge et al. (2020a) have used BLS, among other more advanced techniques, to identify ultra-compact ($P < 1$ h), double-degenerate, eclipsing white dwarf binary systems within the ZTF data archive that emit powerful gravitational waves detectable by the future LISA mission (Amaro-Seoane et al., 2017).

While the BLS algorithm specializes at identifying eclipse-like variability, such as eclipsing binaries and variability caused by star spots through stellar rotation (see Kilic et al., 2015), it does not perform well for identifying other types of variables that display sinusoidal variations, such as ellipsoidal distortions caused by the tidal interactions between two closely-orbiting bodies, reflection from a hot star off of its cool companion, relativistic beaming (Zucker et al., 2007), and stellar pulsations. For this sinusoidal variability, one must make use of other period finding algorithms such as the Lomb Scargle Periodogram (Lomb, 1976; Scargle, 1982) (see also VanderPlas, 2018) or more advanced techniques such as Conditional Entropy (Graham et al., 2013) and Analysis of Variance (Schwarzenberg-Czerny , 1996).

We made use of the Supercomputing Center for Education and Research (OSCER) at the University of Oklahoma to perform a BLS search on all 2,498 light curves within our sample. We searched for periodic variability along a linear grid of six million evenly-spaced frequency points between periods from five minutes up to 12 hours, excluding 12 hours due to strong period aliasing at this value. The lower-end of our grid focused on identifying short-period double-degenerate binaries emitting powerful gravitational

waves, similar to what was identified in Burdge et al. (2020a), in addition to pulsating and rapidly-rotating single white dwarfs. On the longer end of our search, we focused on identifying double-degenerate white dwarf binaries and white dwarfs with low-mass or sub-stellar companions with long orbital periods. It should be noted that Rappaport et al. (2021) have shown that the minimum orbital period allowed by a hydrogen rich body (including MS stars, brown dwarfs, and gas giant planets) in a binary with a mean-mass white dwarf is $P_{\rm min} \approx 37$ min before the Roche geometry begins to destroy the companion.

5.3 Identified Variable systems

We defined the significance of variability as the power returned from our BLS algorithm for the highest peak divided by the average power across the entire periodogram. Our period search returned 75 potential variables with significance above 3.5 and an additional 734 potential variables with significance below 3.5, but with more than nine 4σ or more than seven 5σ deviant points. We manually checked all 809 potential variables to confirm their nature and recovered 62 clearly variable objects, all but two of which show regular eclipses. This strong bias towards identifying eclipsing systems is no surprise considering that the BLS period finding algorithm specializes in identifying eclipsing binaries, rather than variability caused by other sources. Here we present our results on 50 of these binaries broken into six sections: contact binary, accreting white dwarf binaries, HW Virginis (typically subdwarf B-type stars with M-dwarf companions), short-period binaries, and long-period binaries. We excluded 12 binaries due to low signal-to-noise ratios or due to ongoing follow-up that will be used in future publications.

5.3.1 Contact Binary ZTF J091853.36+350531.95

Our box least squares period finding algorithm identified a single contact binary, ZTF J091853.36+350531.95 (J0918+3505). Recovering even one contact binary through a BLS period-finding algorithm is surprising given that the BLS period finding algorithm specializes in identifying sharp ingress and egress features typically found in eclipsing binaries, rather than the sinusoidally-varying light curve shape of a contact binary.

J0918+3505 was first identified by Drake et al. (2014) as a part of their search for variability within the Catalina Surveys Data Release 1. The original authors obtain a most-probable period of 0.4135642 d with magnitude variations of approximately 0.3 mag, in nearly perfect agreement with our period of 0.4135649 d obtained using the public ZTF light curve. Figure 5.1 displays the public ZTF light curve of J0918+3505, its BLS periodogram, and light curve phase-folded to the most probable frequency, defined as the frequency with the highest BLS power. The results from this binary demonstrates the accuracy and precision of this method for identifying variable systems in archival survey data.

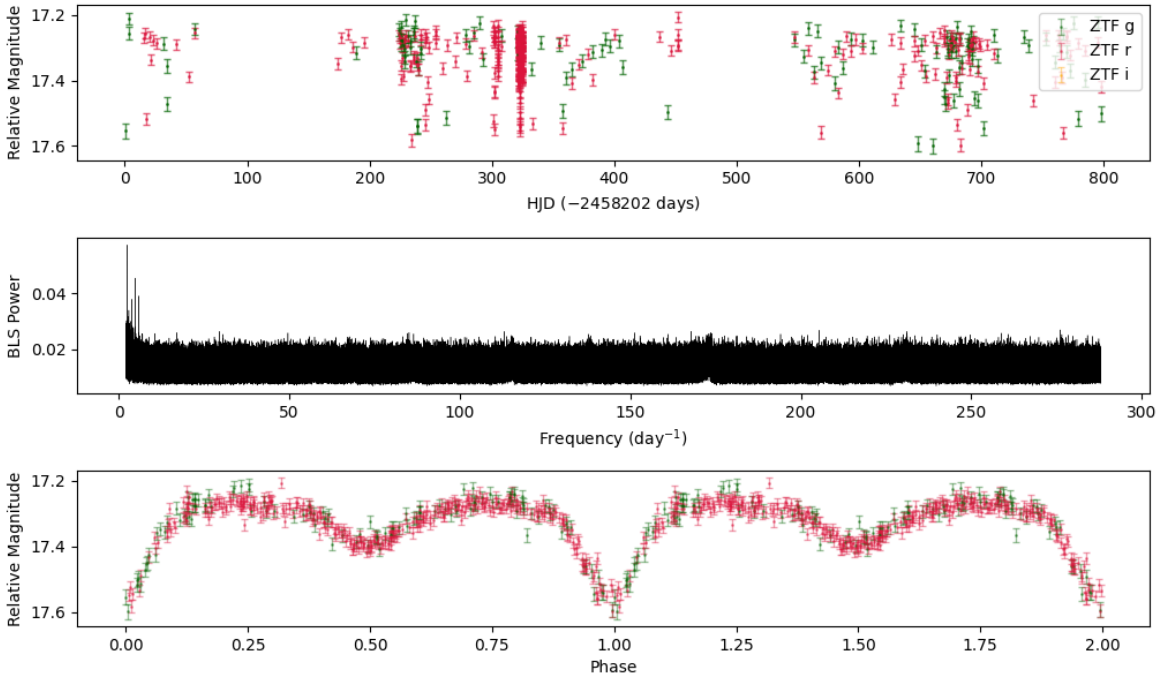

Fig. 5.1.— Top: Public ZTF DR4 light curve of ZTF0918+3505. Middle: BLS periodogram spanning the period range from 5 minutes to just under 12 hours. Bottom: Public ZTF DR4 light curve of ZTF0918+3505 phase folded to the period of the highest peak in the BLS periodogram. Individual data points are colored based on which ZTF filter they were observed with: green points were measured with ZTF g-band filter, red points were measured with ZTF r-band filter, and orange points were measured with the ZTF i-band filter. Filters have been median combined to the median value of the ZTF g-band filter.

5.3.2 Accreting white dwarf binaries

While the Gaia DR2 white dwarf catalogue of Gentile Fusillo et al. (2019) does not specifically aim to identify accreting white dwarf binaries, the authors note some level of contamination by such systems. We find five binary systems containing a white dwarf accreting material from a donor star, all of which are previously known. Four of these systems are short-period cataclysmic variables (CVs), while the fifth is a deeply-eclipsing AM CVn binary. For completeness, and to demonstrate the effectiveness of the BLS algorithm in finding such systems, we present their phase-folded public ZTF DR4 light curves in Figure 5.2. Table 5.1 provides a summary of each of these CVs.

ZTF J093537.4651+161950.8204

ZTF J093537.4651+161950.8204 (J0935+1619) is a spectroscopically confirmed CV with orbital period $P = 92.2$ min and distance $d_\pi = 1.7 \pm 0.6$ kpc. J0935+1619 was first identified by Szkody et al. (2009) as part of an effort to follow-up CVs within SDSS VII. Their analysis shows a strong He II emission relative to Hβ, suggesting that this system is an old nova, rather than a magnetic white dwarf.

ZTF J131223.4866+173659.2754

ZTF J131223.4866+173659.2754 (J1312+1736) is a spectroscopically confirmed eclipsing magnetic CV (HM Herculis type binary; polar) with orbital period $P = 91.9$ min and distance $d_\pi = 0.74 \pm 0.18$ kpc. J1312+1736 was first identified by Vogel et al. (2008) as a serendipitous discovery in their XMM Newton data. Their analysis suggests that the magnetic field strength must be less than $B < 10$ MG and that additional follow-up

observations, including polarimetry, will be required to further constrain the field strength and white dwarf mass.

ZTF J150240.8836+333423.4183

ZTF J150240.8836+333423.4183 (J1502+3334) is a well-studied, spectroscopically confirmed, ultra-short period, eclipsing CV with orbital period $P = 84.8$ min at a distance $d_\pi = 186 \pm 3$ pc. The eclipsing nature of J1502+3334 was first identified by Szkody et al. (2006) as part of an effort to follow-up CVs within SDSS V. Follow-up studies by Savoury et al. (2011) constrain the mass, radius, temperature, and surface gravity of the white dwarf in J1502+3334 to $M = 0.709 \pm 0.004$ $M_\odot$, $R = 0.01145 \pm 0.00005$ $R_\odot$, $T_{\rm eff} = 11,800 \pm 1200$ K, and $\log g = 8.17 \pm 0.01$, respectively.

ZTF J150722.0644+523040.6602

ZTF J150722.0644+523040.6602 (J1507+5230) is a well-studied, spectroscopically confirmed, short-period, eclipsing CV with orbital period of $P = 66.6$ min located at distance $d_\pi = 212 \pm 4$ pc. J1507+5230 was first identified by Szkody et al. (2005) as part of an effort to follow-up CVs within SDSS IV. Follow-up studies by Savoury et al. (2011) constrain the mass, radius, temperature, and surface gravity of J1507+5230 to $M = 0.892 \pm 0.008$ $M_\odot$, $R = 0.00956 \pm 0.00013$ $R_\odot$, $T_{\rm eff} = 11,300 \pm 1000$ K, and $\log g = 8.45 \pm 0.01$, respectively.

ZTF J161133.9644+630831.6925

ZTF J161133.9644+630831.6925 (J1611+6308; Gaia14aae; ASSASN-14cn) is a well-studied deeply-eclipsing AM CVn binary with orbital period of $P = 49.7$ min located at a distance $d_\pi = 257 \pm 8$ pc based on Gaia eDR3 parallax measurements. J1611+6308 was first identified by the Gaia Science Alerts project and by ASAS-SN due to two outbursts that took place on 2014 June 14 and 2014 August 11. Campbell et al. (2015) extensively followed up J1611+6308 using various telescopes and instruments. Through their analysis, the authors were able to constrain the white dwarf temperature to $T_{\rm eff} = 12,900 \pm 200$ K and the component masses to $M_{\rm WD} > 0.78$ M$_\odot$ and $M_{\rm donor} > 0.015$ M$_\odot$.

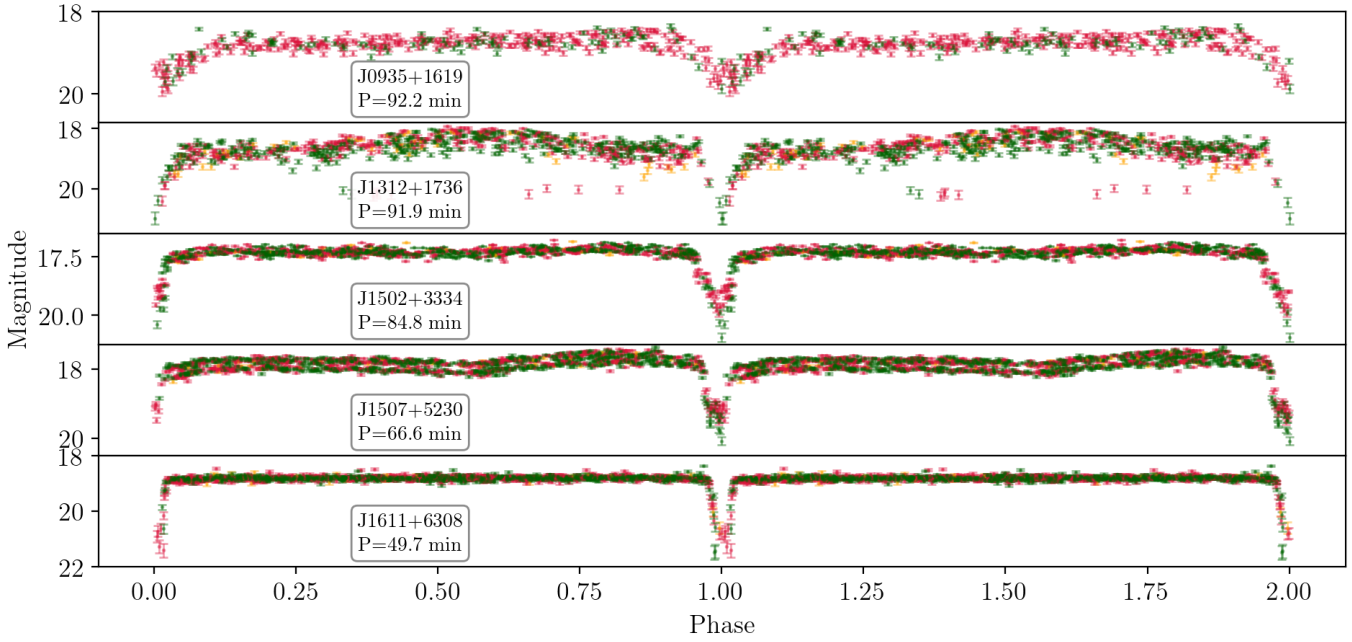

Fig. 5.2.— Public ZTF DR4 light curves for the five, previously known, accreting white dwarf binaries reidentified in this work. Each light curve has been phase-folded to its most probable period, obtained through our BLS variability search. Individual data points are colored based on which ZTF filter they were observed with: green points were measured with ZTF g-band filter, red points were measured with ZTF r-band filter, and orange points were measured with the ZTF i-band filter. Filters have been median combined to the median value of the ZTF g-band filter.

5.3.3 Short period binaries

Our BLS search returned a total of 11, likely white dwarf, eclipsing binaries with orbital periods between 24 minutes and six hours and relatively short eclipse durations. Here we present the public ZTF DR4 light curves for each of these systems phase folded at their most probable periods and provide a summary of each system. Table 5.2 contains a summary of the right ascension, declination, orbital period, distance, and magnitude for each of these eleven binaries. Figures 5.3 & 5.4 shows the public ZTF DR4 light curves for each of these systems, colored by the filter each measurement was taken in.

Of the 11 short-period eclipsing binaries presented here, J0722−1839 (Burdge et al., 2020a) and J1901+5309 (Coughlin et al., 2020), are previously published double white dwarf binaries and strong gravitational wave emitters, showing the effectiveness in our method at identifying eclipsing gravitational wave binaries. The remaining nine binaries are new discoveries, including a new double-lined spectroscopic eclipsing binary J1356+5705 which, with additional follow-up, may provide direct measurements of the masses and radii of the individual stars in the binary.

Of the remaining eight new binaries, five appear to be double degenerate binaries and three are likely not double degenerate binaries based on their eclipse durations. Identifying merging double degenerate binaries is important for constraining the formation rates of post-merger systems observed in the Galaxy today, including supernovae (see Liu et al., 2018) and massive white dwarfs (see Cheng et al., 2020). Eclipsing double-degenerate systems are especially useful since they provide a way to directly measure the individual stellar parameters, providing useful constraints for binary population synthesis studies of

Table 5.1: Gaia eDR3 ID, RA, Dec, distance, and periods for the five, previously known, accreting white dwarf binaries reidentified in this work. Distance values are based on the Gaia eDR3 parallax and its uncertainty. Distances for targets marked with a $^{\diamond}$ use the photo-geometric distances from Bailer-Jones et al. (2021) due to imprecise Gaia eDR3 parallax measurements.

Gaia eDR3 ID	RA (J2000)	Dec (J2000)	Gaia G (mag)	Distance (pc)	Period (min)
619153448780495872$^{\diamond}$	09:35:37.4651	+16:19:50.8204	18.73	1559^{+715}_{-389}	92.2
3937217307886601088	13:12:23.4866	+17:36:59.2754	19.52	740 ± 180	91.9
1289860214647954816	15:02:40.8836	+33:34:23.4183	17.23	186 ± 3	84.8
1593140224924964864	15:07:22.0644	+52:30:40.6602	18.15	212 ± 4	66.6
1629388752470472704	16:11:33.9644	+63:08:31.6925	18.29	257 ± 8	49.7

double degenerate binaries (Maoz et al., 2018). Spectroscopic follow-up observations of the double-degenerate binaries presented here will be useful to properly classify each of these systems and determine their component masses and effective temperatures. Obtaining a well-sampled eclipsing light curves of the newly-discovered double-degenerate binaries will be useful to constrain the individual stellar radii, inclination, and companion effective temperature.

Table 5.2:: Basic system information for the eleven short-period, likely white dwarf, binaries identified in this work. Distance values are based on the Gaia eDR3 parallax and its uncertainty. ZTF0722−1839 and ZTF1901+5309 were first identified by Burdge et al. (2020a) and Coughlin et al. (2020), respectively. Distances for targets marked with a $^{\diamond}$ use the photo-geometric distances from Bailer-Jones et al. (2021) due to imprecise Gaia eDR3 parallax measurements.

Gaia eDR3 ID	RA (J2000)	Dec (J2000)	Gaia G (mag)	Distance (pc)	Period (min)	$T_{\rm eff}$ (K)	$\log g$
2931430078489330944$^{\diamond}$	07:22:21.4792	-18:39:30.4186	19.05	902^{+178}_{-109}	23.7	···	···
3056132667218411776	07:40:32.7265	-05:45:21.7818	16.70	1235 ± 286	≈ 183.6	···	···
1079882115405261568	11:10:16.7524	+74:45:59.8720	18.62	500 ± 40	86.8	···	···

Continued on next page

Table 5.2 – continued from previous page

Gaia eDR3 ID	RA (J2000)	Dec (J2000)	Gaia G (mag)	Distance (pc)	Period (min)	$T_{\rm eff}$ (K)	$\log g$
1657868410028294784	13:56:26.7065	+57:05:45.2620	18.95	360 ± 20	91.9	25400 ± 200	6.94 ± 0.02
1410739870171621504	16:37:43.4898	+49:17:40.4086	19.34	200 ± 10	61.5	···	···
4569543730600175744	17:30:21.1198	+23:55:40.3919	18.87	370 ± 20	290.5	···	···
4550559356677735040	17:37:56.7846	+18:14:03.5758	19.21	580 ± 70	360.9	···	···
1418364678367782016	17:47:47.2775	+55:29:17.8595	19.15	433 ± 41	92.0	···	···
1656197800893107712	17:58:12.8607	+76:42:16.7465	18.96	620.4 ± 70	94.6	···	···
2134541781964072320	19:01:25.4238	+53:09:29.4163	18.04	910 ± 70	40.6	28000 ± 500	7.6 ± 0.3
2183626416274746496	20:36:01.6713	+55:06:48.7526	19.66	1650 ± 960	117.4	···	···

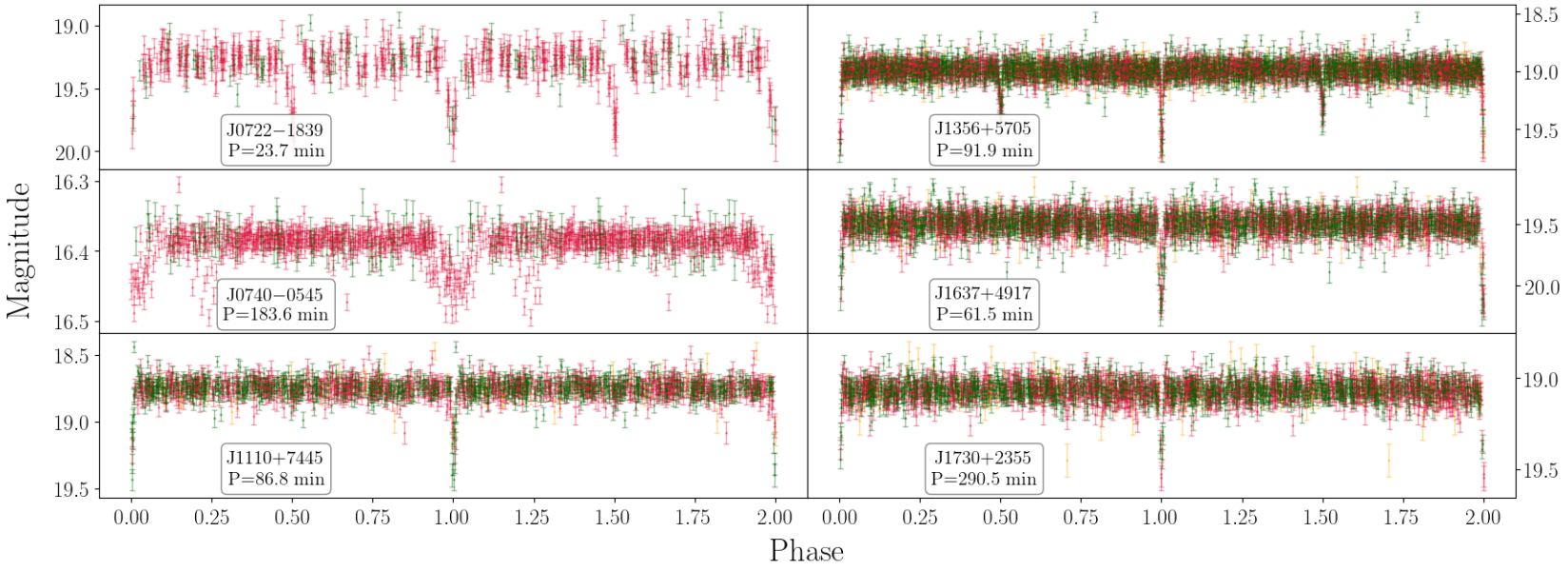

Fig. 5.3.— Public ZTF DR4 light curves for the six of the short-period binaries identified in this work. Light curves are phase folded to their most probable periods obtained through our BLS variability search. Individual data points are colored based on which ZTF filter they were observed with: green points were measured with ZTF g-band filter, red points were measured with ZTF r-band filter, and orange points were measured with the ZTF i-band filter. Filters have been median combined to the median value of the ZTF g-band filter.

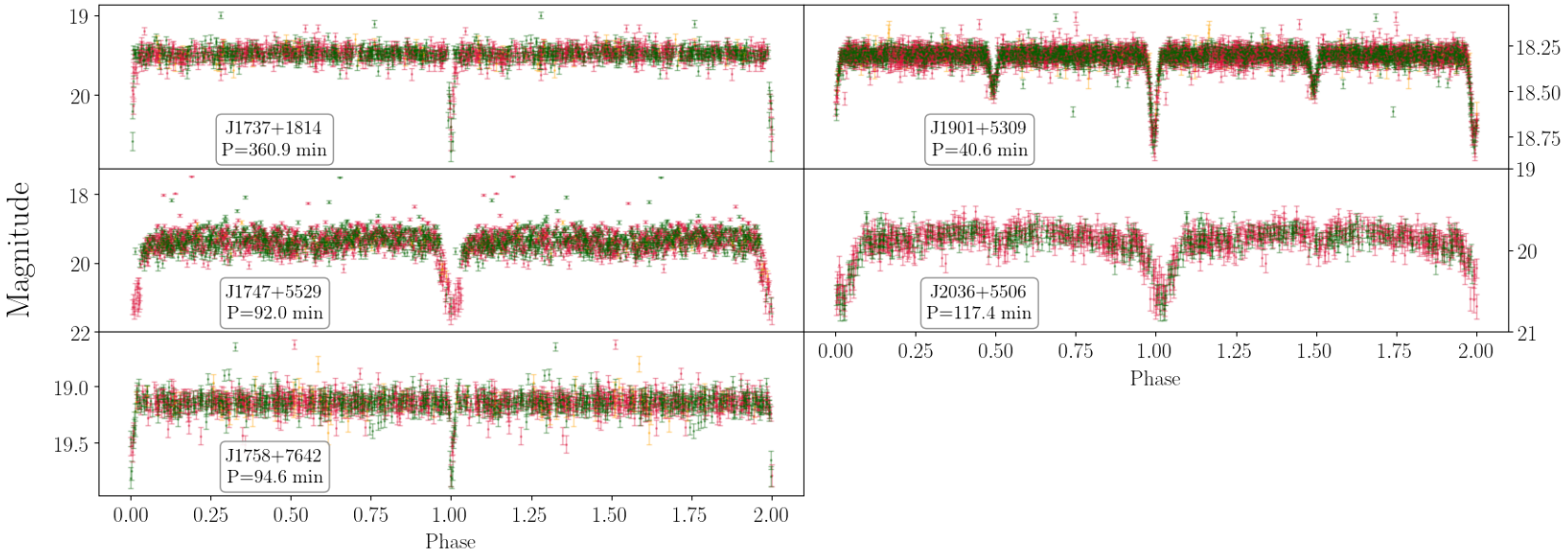

Fig. 5.4.— Public ZTF DR4 light curves for the five of the short-period binaries identified in this work. Light curves are phase folded to their most probable periods obtained through our BLS variability search. Individual data points are colored based on which ZTF filter they were observed with: green points were measured with ZTF g-band filter, red points were measured with ZTF r-band filter, and orange points were measured with the ZTF i-band filter. Filters have been median combined to the median value of the ZTF g-band filter.

ZTF J072221.48−183930.42

ZTF J072221.48−183930.42 (J0722−1839) was first identified by Burdge et al. (2020a) in their search for gravitational wave binaries with periods less than one hour in ZTF. The authors show that J0722−1839 is an eclipsing double degenerate white dwarf binary with orbital period of $P = 23.70$ min at an inclination of $i = 89.66 \pm 0.22°$. J0722−1839 contains two low-mass white dwarfs with similar masses and radii. The white dwarfs are described by the following parameters: $M_1 = 0.38 \pm 0.04$ $M_\odot$, $M_2 = 0.33 \pm 0.03$ $M_\odot$, $R_1 = 0.0224^{+0.0004}_{-0.0002}$ $R_\odot$, $R_2 = 0.0249^{+0.0001}_{-0.0003}$ $R_\odot$.

The public ZTF DR4 light curve for J0722−1839 returns $P_0 = 11.85$ min as the most probable period for this system. Given the similar primary and secondary eclipse depths in this system, our BLS algorithm found a period that is half the true period in this system of $P = 23.70$ min. Identifying gravitational wave binaries, such as J0722−1839, is crucial for characterizing the gravitational wave foreground before the launch of LISA. J0722−1839 will serve as a strong LISA gravitational wave verification binary.

ZTF J074032.7265−054521.7818

ZTF J074032.7265−054521.7818 (J0740−0545) is a previously unidentified short-period eclipsing binary with an orbital period $P \approx 183.6$ min at a distance of $d_\pi = 1235 \pm 286$ pc based on Gaia eDR3 parallax measurements. We estimated the eclipse duration (ingress to egress) as $\Delta T \approx 29$ min. Based on this eclipse duration, the system likely contains a main sequence star. Unfortunately, due to the poor eclipse sampling in any individual ZTF filter, we are unable to properly analyze the system's parameters through light curve fitting. Optical spectroscopic follow-up will be useful to constrain the surface gravity

and temperature of the primary white dwarf. Time-series spectroscopy will then provide the minimum companion mass and orbital separation. Additionally, high signal-to-noise eclipsing photometry, when combined with light curve fitting and the spectroscopic temperature solution, will provide direct constraints on the temperature of the secondary and the inclination of the binary.

ZTF J111016.7524+744559.8720

ZTF J111016.7524+744559.8720 (J1110+7445) is a previously unidentified short-period eclipsing binary with orbital period $P = 86.8$ min at a distance of $d_\pi = 500 \pm 40$ pc based on Gaia eDR3 parallax measurements. Given the total eclipse duration of $\Delta T \approx 80$ s, J1110+7445 must be a double degenerate binary. J1110+7445 would benefit greatly from follow-up time-series spectroscopy.

ZTF J135626.71+570545.26

ZTF J135626.71+570545.26 (J1356+5705) was first identified in the ZTF data archive by the Caltech group including Dr. Thomas Prince. As principal investigator for the observations, Dr. Prince and collaborators obtained 13 follow-up spectra of J1356+5705 as a part of program ID C281 on UT 2019 March 04 using the Keck Low Resolution Imaging Spectrometer (LRIS) with the 600/4000 grism and the 1.0 arcsec slit. We downloaded the raw archival data with their associated calibration files and perform standard data reduction using IRAF. We flux calibrated the data using a Feige34 standard star observation taken on the same night with the same instrument setup. While our BLS periodogram analysis returns a most probable period of $P = 46.0$ min, the fit to our radial

velocity measurements for the 13 LRIS spectra show that the period is roughly twice this value, suggesting that the ZTF light curve detects both the primary and secondary eclipses at similar depths, confusing them for a single eclipse at half the true orbital period. Inspection of the LRIS blue and red spectra show the weak double-lined nature of this system. Due to the low resolution of this Keck LRIS data, we are unable to measure the radial motion of each star through their unresolved Balmer lines.

We created a zero-velocity summed spectrum using the IRAF task SUMSPEC and perform model atmosphere fitting to this summed spectrum with a grid of pure hydrogen DA white dwarf models. Our best fit model atmosphere has effective temperature $T_{\rm eff} = 25,400 \pm 200$ K and surface gravity $\log g = 6.94 \pm 0.02$. We note that the weakly-seen double-lined optical spectrum acts to increase the width of the lines when combined, thus causing our fit to overestimate the surface gravity of the primary. Given the similar luminosities of the two stars in the binary, as seen in the eclipsing light curve, a proper model atmosphere fit including the light from both stars will be necessary to obtain the correct atmospheric parameters for this binary. We present the summed blue-optical LRIS spectrum and best-fit single-star model overplotted onto the Balmer lines in Figure 5.5.

J1356+5705 was independently identified by Keller et al. (2021) using a similar box least squares approach to the ZTF data archive. Their BLS period finding algorithm returned a best-fit period of $P = 46.0$ min due to the similar eclipse depths confusing their algorithm.

ZTF J163743.4898+491740.4086

ZTF J163743.4898+491740.4086 (J1637+4917) is a previously unidentified short-period eclipsing binary with orbital period $P_0 = 61.5$ min at a distance $d_\pi = 200 \pm 10$ pc based on Gaia eDR3 parallax measurements. Our BLS algorithm returned a strong period alias at twice the orbital period. When phase-folded to this new period, the light curve shows primary and secondary eclipses of similar depths of $\Delta m \approx 0.6$ mag. Due to the eclipse duration of $\Delta T \approx 81$ s ($\Delta T \approx 51$ s if folded to twice the most probable period), J1637+4917 must be a double degenerate binary and may contain two similar-luminosity white dwarfs, similar to J0722−1839 (Burdge et al., 2020a), although on a much longer orbital period.

Spectroscopic follow-up observations may reveal a double-lined spectrum that can be used to constrain the individual radial velocities for each star in the binary, providing precise constraints on their masses, temperatures, and orbital separation. J1637+4917 was independently identified by Keller et al. (2021) using a similar box least squares approach to the ZTF data archive.

ZTF J173021.1198+235540.3919

ZTF J173021.1198+235540.3919 (J1730+2355) is a previously unidentified eclipsing binary with orbital period $P = 290.5$ min at a distance $d_\pi = 370 \pm 20$ pc based on Gaia eDR3 parallax measurements. J1730+2355 has eclipse duration $\Delta T \approx 270$ s.

ZTF J173756.7846+181403.5758

ZTF J173756.7846+181403.5758 (J1737+1814) is a previously unidentified eclipsing binary with orbital period $P = 360.9$ min at a distance $d_\pi = 580 \pm 70$ pc based on Gaia eDR3 parallax measurements. J1737+1814 has eclipse duration $\Delta T \approx 420$ s.

ZTF J174747.2775+552917.8595

ZTF J174747.2775+552917.8595 (J1747+5529) is a previously unidentified short-period eclipsing binary with orbital period $P = 92.0$ min at a distance $d_\pi = 433 \pm 41$ pc based on Gaia eDR3 parallax measurements. Given the shape and duration of the eclipse ($\Delta T \approx 490$ s), J1747+5529 is likely not a double degenerate binary. J1747+5529 was independently identified by Keller et al. (2021) using a similar box least squares approach to the ZTF data archive.

ZTF J175812.8607+764216.7465

ZTF J175812.8607+764216.7465 (J1758+7642) is short-period eclipsing binary with orbital period $P = 94.6$ min at a distance $d_\pi = 620.4 \pm 70$ pc based on Gaia eDR3 parallax measurements. J1758+7642 has eclipse duration $\Delta T \approx 94$ s and is likely a double degenerate binary. J1758+7642 was independently identified by Keller et al. (2021) using a similar box least squares approach to the ZTF data archive.

ZTF J190125.4238+530929.4163

ZTF J190125.4238+530929.4163 (J1901+5309) was first identified by Coughlin et al. (2020) in their search using Pan-STARRS colors to identify variable white dwarf binaries

in ZTF. The authors demonstrated that J1901+5309 is a short-period, eclipsing, double white dwarf binary with a most probable period of $P = 40.6$ min, obtained through a conditional entropy period search of the ZTF light curve, making J1901+5309 a strong gravitational wave binary. Their detailed analysis showed that J1901+5309 contains two white dwarfs with temperatures $T_{\rm eff,1} = 28,000 \pm 500$ K and $T_{\rm eff,2} = 17,600 \pm 400$ K at inclination $i = 86.2^{+0.6\circ}_{-0.2}$. Our BLS search recovers J1901+5309 with a period identical to the original authors'.

ZTF J203601.6713+550648.7526

ZTF J203601.6713+550648.7526 (J2036+5506) is a short-period eclipsing binary with orbital period $P = 117.4$ min at a distance $d_\pi = 1.65 \pm 0.96$ kpc. The public ZTF DR4 light curve shows a reflection effect and a relatively shallow secondary eclipse. Given the shape of the light curve and the duration of the eclipse ($\Delta T \approx 970$ s), J2036+5506 must contain a main sequence companion. J2036+5506 was independently identified by Keller et al. (2021) using a similar box least squares approach to the ZTF data archive.

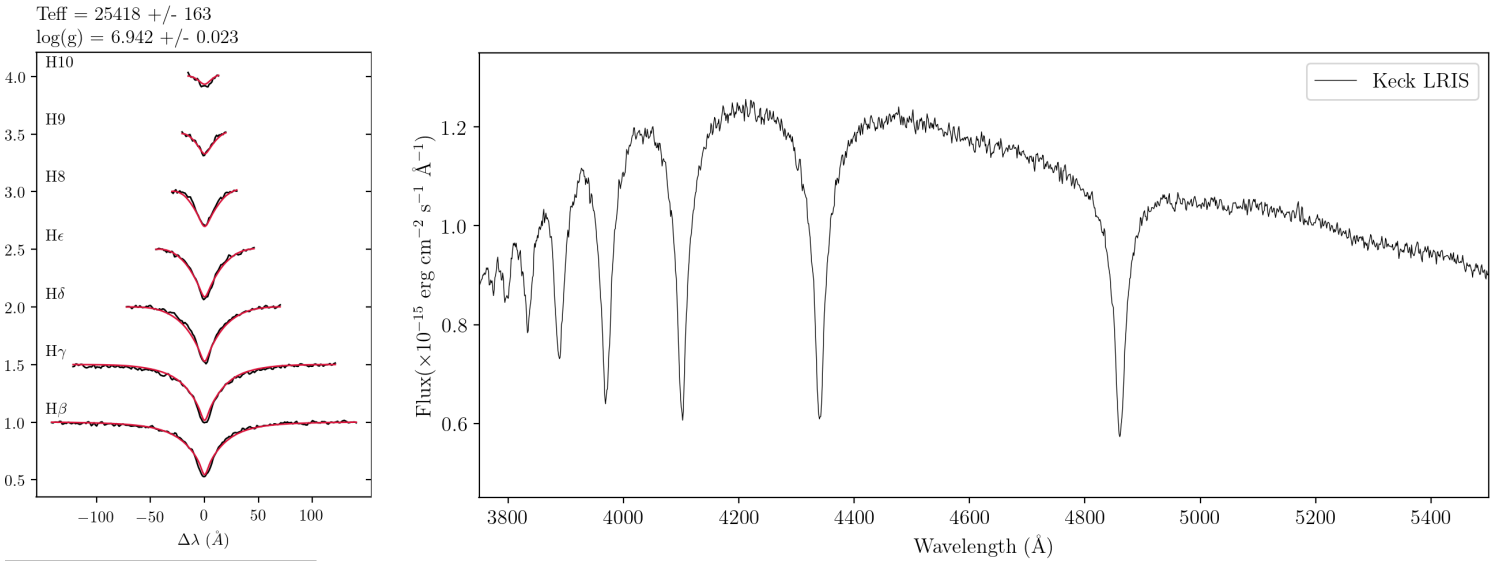

Fig. 5.5.— Left: The best-fitting model atmosphere to the Balmer lines of J1356+5705. Model atmosphere parameters $T_{\rm eff}$ and $\log g$ are displayed above the plot. Right: Summed Keck LRIS optical spectrum of J1356+5705.

5.3.4 Long period binaries

Our BLS search returned 14, likely main sequence, eclipsing binaries with periods between $P = 5.2$ h and $P = 38.5$ h. Because our period search was limited to only 12 h, many of these binaries were discovered due to their period aliases with $P < 12$ h. For these targets we manually adjust the period range and rerun our BLS algorithm to identify the true period. Table 5.3 contains a summary of the right ascension, declination, orbital period, distance, and magnitude for each of these 14 binaries. Figures 5.6 & 5.7 shows the public ZTF DR4 light curves for each of these systems, colored by the filter each measurement was taken in. Out of our 14 long-period binaries, 11 are new discoveries.

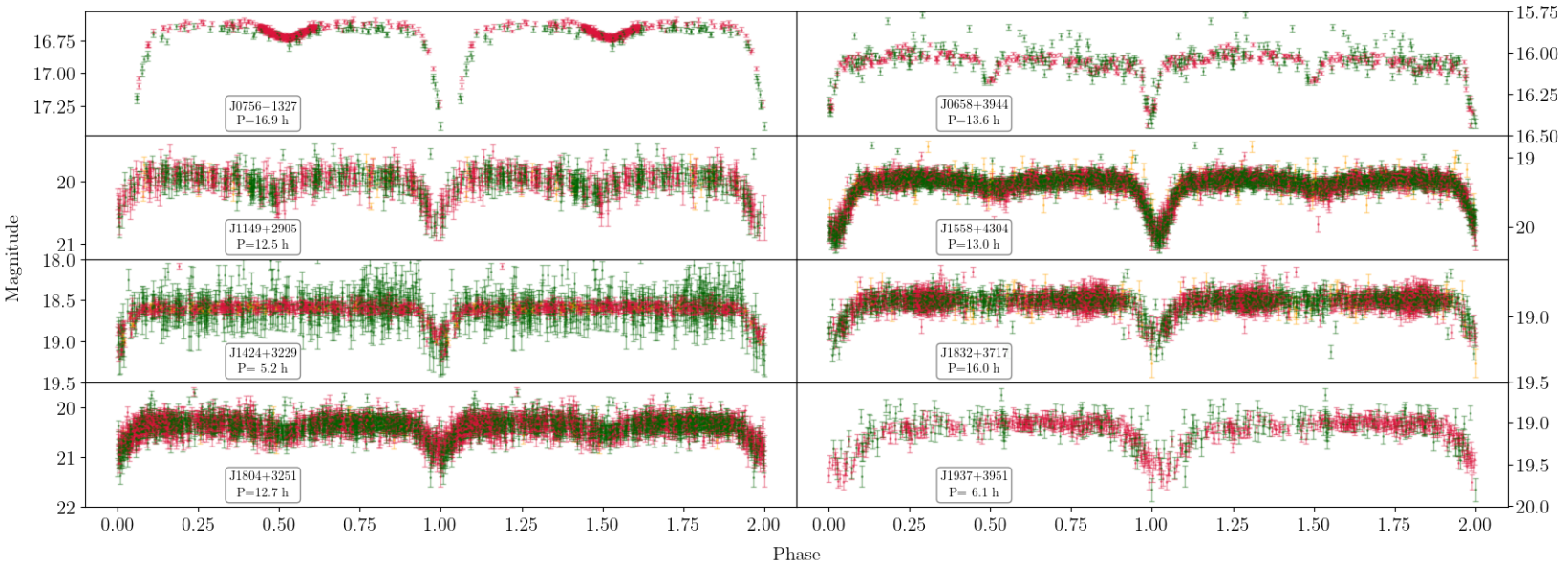

Fig. 5.6.— ZTF public DR4 light curves for eight of the long-period eclipsing binaries identified in this work. Each light curve has been phase-folded to its most probable period, obtained through our BLS variability search. Individual data points are colored based on which ZTF filter they were observed with: green points were measured with ZTF g-band filter, red points were measured with ZTF r-band filter, and orange points were measured with the ZTF i-band filter. Filters have been median combined to the median value of the ZTF g-band filter.

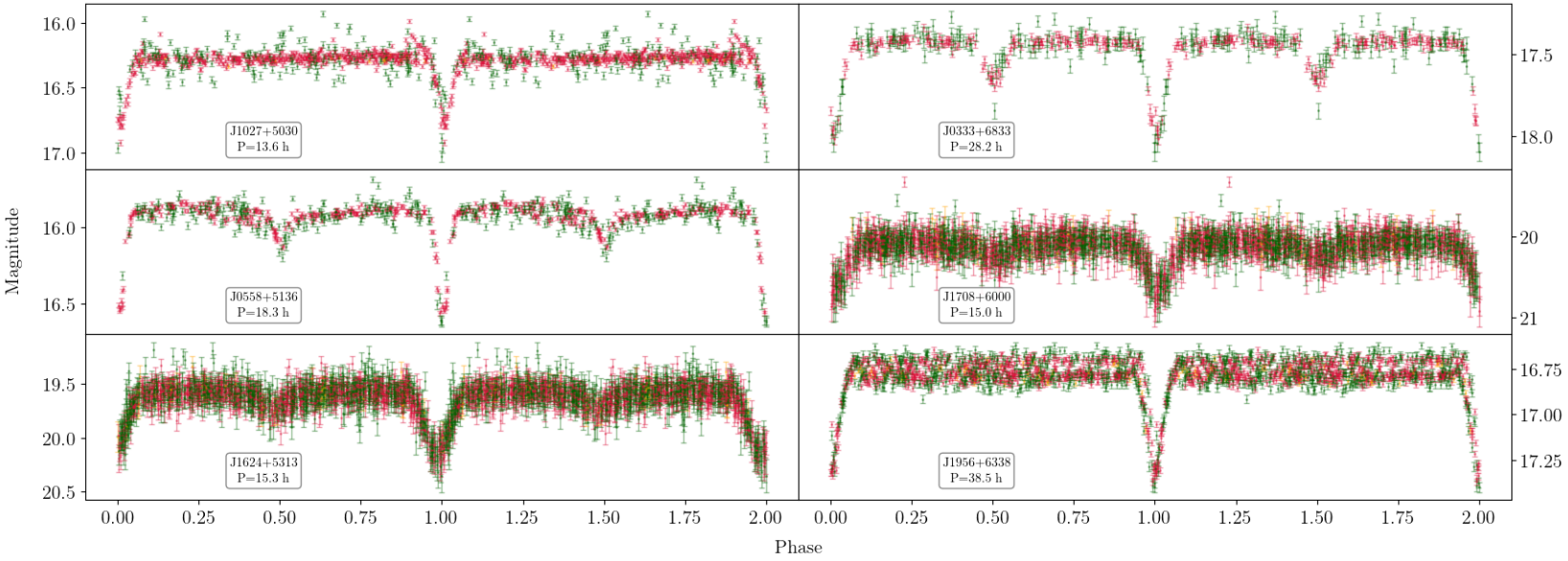

Fig. 5.7.— ZTF public DR4 light curves for six of the long-period eclipsing binaries identified in this work. Light curves are folded to the most probable period obtained from our BLS algorithm. Each data point is colored based on which ZTF filter it was measured in: green points were measured in ZTF g-band, red points were measured in ZTF r-band, and orange points were measured in ZTF i-band.

ZTF J033323.2480+683319.7087

ZTF J033323.2480+683319.7087 (J0333+6833) is an eclipsing binary with an orbital period of $P = 423.15$ min. J0333+6833 was identified as a target within 5 arcsec of a white dwarf candidate within the Gentille Fusillo Gaia DR2 white dwarf catalogue (Gentile Fusillo et al., 2019). Based on Gaia eDR3 parallax measurements, J0333+6833 is at a distance of $d_\pi = 4.5 \pm 1.5$ kpc, while the nearby white dwarf is at a distance of $d_\pi = 113 \pm 4$ pc. These systems are not physically associated.

ZTF J055805.5578+513640.3204

ZTF J055805.5578+513640.3204 (J0558+5136) is a previously known Algol-type eclipsing binary discovered serendipitously while observing comet C/2006 OF2 (Elenin, 2009) with reported orbital period $P = 0.7625$ d (1098 min), in good agreement with our period obtained through BLS period analysis of $P_{ZTF} = 1097.9$ min.

ZTF J065838.8266+394455.7615

ZTF J065838.8266+394455.7615 (J0658+3944) is an Algol-type detached eclipsing binary originally identified by Drake et al. (2014) in their search for variable stars in Catalina surveys. J0658+3944 has a reported orbital period $P = 0.566324$ d (815.5 min), in perfect agreement with the period we obtain from the public ZTF data.

ZTF J075637.2874−132704.2714

ZTF J075637.2874−132704.2714 (J0756−1327) is an eclipsing binary with orbital period $P = 1016.7$ min at a distance $d_\pi = 5.9 \pm 2.0$ kpc.

Table 5.3: Gaia eDR3 Source ID, RA, Dec, distance, and periods for the 14 long-period, likely main sequence, eclipsing binaries identified in this work. Distance values are based on the Gaia eDR3 parallax and its uncertainty. J0558+5136 and J0658+3944 were first identified by Elenin (2009) and Drake et al. (2014). J0333+6833 and J1956+6338 were identified in our sample due to their proximity to nearby white dwarf candidates.

Gaia eDR3 ID	RA (J2000)	Dec (J2000)	Gaia G (mag)	Distance (pc)	Period (h)
494346715682365696	03:33:23.2480	+68:33:19.7087	17.46	4500 ± 1500	28.1
214738885809120256	05:58:05.5578	+51:36:40.3204	15.81	351 ± 5	18.3
950418645619875840	06:58:38.8266	+39:44:55.7615	15.59	149.4 ± 0.9	13.6
3035603999154879872	07:56:37.2874	-13:27:04.2714	16.61	5880 ± 1971	16.9
847322662964518400	10:27:43.5483	+50:30:59.0274	18.34	147 ± 3	13.6
4019913570274894848	11:49:07.8352	+29:05:12.4877	19.93	2800 ± 5000	12.5
1477919863129680896	14:24:46.3107	+32:29:25.6898	16.61	393 ± 19	5.2
1384415294059868544	15:58:24.7432	+43:04:07.4597	19.25	1700 ± 700	13.0
1425229028243292672	16:24:31.4130	+53:13:07.9561	19.57	1650 ± 610	15.3
1437501089838298496	17:08:47.6216	+60:00:11.8750	20.05	···	15.0
4603585989283645696	18:04:02.2624	+32:51:50.0292	20.25	1100 ± 500	12.7
2096210259701981696	18:32:04.6693	+37:17:35.0443	18.76	4600 ± 2900	16.0
2076464409550919040	19:37:14.0969	+39:51:10.1419	20.37	1270 ± 950	6.1
2241311988884528512	19:56:06.3171	+63:38:40.7011	16.89	2660 ± 380	38.5

ZTF J102743.5483+503059.0274

ZTF J102743.5483+503059.0274 (J1027+5030) is an eclipsing binary with orbital period $P = 813.1$ min at a distance $d_\pi = 147 \pm 3$ pc based on Gaia eDR3 parallax measurements.

ZTF J114907.8352+290512.4877

ZTF J114907.8352+290512.4877 (J1149+2905) is a faint ($G = 19.93$ mag) eclipsing binary with an orbital period $P = 749.4$ min. Due to the imprecise Gaia eDR3 parallax measurements, we used the photo-geometric distance from Bailer-Jones et al. (2021) $d = 1424^{+797}_{-525}$ pc.

ZTF J142446.3107+322925.6898

ZTF J142446.3107+322925.6898 (J1424+3229) is likely an eclipsing main sequence binary with orbital period $P = 314.9$ min. J1424+3229 was identified in our search for variable white dwarfs within ZTF due to its proximity to a nearby ($\Delta d < 5$ arcsec) spectroscopically confirmed DB white dwarf (Gaia eDR3 ID 1477919927548534784; SDSS J142446.25+322930.2). J1424+3229 lies at a distance of $d_\pi = 319 \pm 19$ pc based on Gaia eDR3 parallax measurements and has Gaia eDR3 proper motion measurements $\mu_\alpha = -15.86 \pm 0.10$ mas yr^{-1} and $\mu_\delta = -11.19 \pm 0.11$ mas yr^{-1}. The nearby DB white dwarf has a Gaia G magnitude of $G = 19.1$ mag, parallax-distance of $d_\pi = 389 \pm 31$ pc, and proper motion $\mu_\alpha = -16.31 \pm 0.16$ mas yr^{-1} and $\mu_\delta = -11.09 \pm 0.18$ mas yr^{-1}. Given the precision of the Gaia eDR3 astrometry, based on these parallax-distances, it is unlikely that these objects are associated. However, considering their similar proper motions, this system warrants further study.

ZTF J155824.7432+430407.4597

ZTF J155824.7432+430407.4597 (J1558+4304) is an eclipsing horizontal branch star with orbital period $P = 781.2$ min. J1558+4304 was classified as a blue horizontal branch star in SDSS by Sirko et al. (2004). Harrigan et al. (2010) estimate the surface gravity of ZTF J1558+4304 using SDSS spectroscopy to be $\log g = 3.39$.

ZTF J162431.4130+531307.9561

ZTF J162431.4130+531307.9561 (J1624+5313) is an eclipsing binary with orbital period $P = 918.5$ min and Gaia eDR3 distance $d_\pi = 1.6 \pm 0.6$ kpc.

ZTF J170847.6216+600011.8750

ZTF J170847.6216+600011.8750 (J1708+6000) is a faint ($G = 20.05$ mag) eclipsing binary with orbital period $P = 899.7$ min. Due to the faintness of this target, the Gaia eDR3 parallax is unreliable with value $\pi = -0.2 \pm 0.3$ mas.

ZTF J180402.2624+325150.0292

ZTF J180402.2624+325150.0292 (J1804+3251) is a faint ($G = 20.25$ mag) eclipsing binary with orbital period $P = 759.4$ min at a distance $d_\pi = 1.1 \pm 0.5$ kpc.

ZTF J183204.6693+371735.0443

ZTF J183204.6693+371735.0443 (J1832+3717) is an eclipsing binary with orbital period $P = 957.2$ min at a distance $d_\pi = 4.6 \pm 2.9$ kpc.

ZTF J193714.0969+395110.1419

ZTF J193714.0969+395110.1419 (J1937+3951) is faint (G = 20.37 mag) eclipsing binary with orbital period P = 365.1 mag at a distance d_π = 1.27 ± 0.95 kpc.

ZTF J195606.3171+633840.7011

ZTF J195606.3171+633840.7011 (J1956+6338) is an eclipsing binary with an orbital period of P = 2310.7 min at a distance d_π = 2.7 ± 0.4 kpc. J1956+6338 was identified in our search for variability due to its proximity to a nearby (Δd < 5 arcsec) white dwarf candidate (Gaia eDR3 ID 2241311988881895552). The nearby white dwarf candidate is located at a distance d_π = 571 ± 144 pc. It is unlikely that these objects are physically associated.

5.3.5 Hot Subdwarf Binaries

Our BLS search returned ten eclipsing binaries that show a deep primary eclipse, a relatively shallow secondary eclipse, and a strong reflection effect with orbital periods ranging from 2.2 h to 8.8 h, characteristic of a binary containing a hot O-type or B-type subdwarf primary star with a cool, sometimes substellar, companion. Subdwarf B-type stars are typically $M \approx 0.5$ $M_\odot$ Helium-burning stars with thin hydrogen layers. Due to the thin hydrogen layer of these subdwarf stars, common envelope evolution with a binary companion is thought to be the most-probable evolutionary channel for short-period hot subdwarf binaries. These eclipsing hot subdwarf binaries systems are known as HW Virginis type binaries and are the focus of the Eclipsing Reflection Effect Binaries from Optical Surveys (EREBOS) project (Schaffenroth et al., 2019), which brought the

number of known and characterized HW Vir binaries to over 160 from the previously known 36 discovered in the Optical Gravitational Lensing Experiment (OGLE) project (Pietrukowicz et al., 2013; Soszyński et al., 2015).

Given the small sample size of known and characterized HW Vir binaries, identifying more eclipsing subdwarf binaries allows for the study of this common envelope phase. Such studies provide clues for understanding the minimum mass required for a nearby companion to strip the pre-subdwarf giant of its hydrogen envelope without merging with its core. Soker (1998) studied the effects of substellar bodies on common-envelope evolution, potentially leading to short-period subdwarf binaries with substellar companions such as those identified by Schaffenroth et al. (2014).

Out of our ten HW Vir-type binaries, seven appear in the hot subluminous star catalogue of Geier et al. (2019). Similar to our search, Enenstein et al. (2021) have performed a BLS search on the ZTF data archive based on their target selection from the hot subluminous star catalogue of Geier et al. (2019). The authors perform a BLS search for periods between $P_{\rm min}$ = 1 h and $P_{\rm max}$ = 10 d and recover 46 HW Virginis type binaries with a mean period P = 3.8 h, 26 of which appear to be new discoveries. We crossmatched our ten binaries found through our search for eclipsing white dwarfs with the Galactic coordinate plot provided in Enenstein et al. (2021) and find that half were independently discovered by Enenstein et al. (2021), two of which are previously known HW Virginis binaries. Thus four of our ten binaries are new discoveries, not yet published elsewhere. We present the phase-folded public ZTF DR4 light curves for our ten binaries in Figure 5.8.

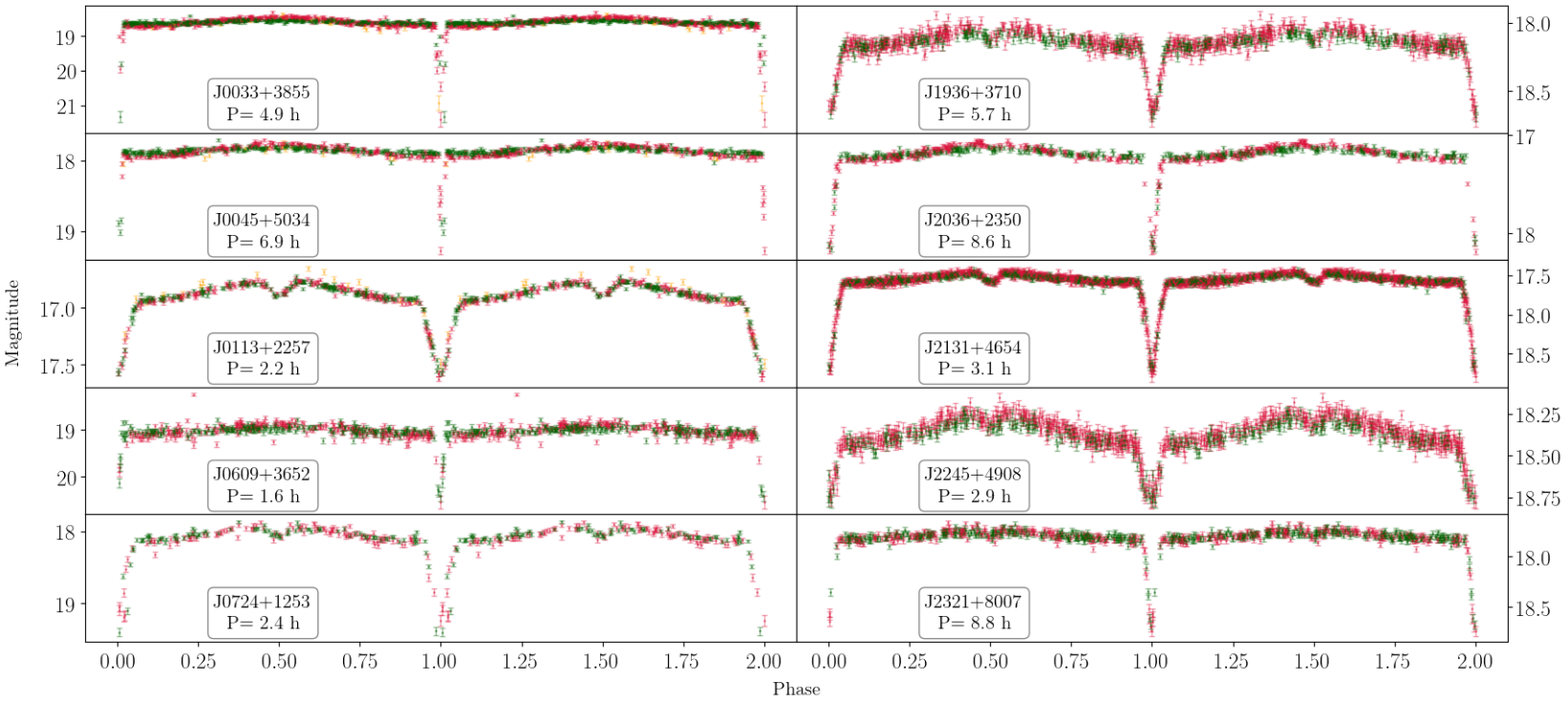

Fig. 5.8.— Phase folded public ZTF DR4 light curves to ten eclipsing subdwarf binaries identified in this work. Data points are colored based on which ZTF filter they were measured in. J0724+1253 and J0113+2257 were first identified in Schindewolf et al. (2015) and Kao et al. (2016), respectively.

We performed light curve fitting on the ZTF r-band data using JKTEBOP for seven of these ten binaries that showed well-sampled ZTF r-band light curves. We fitted for the sum and ratio of the fractional component radii, defined as the stellar radii divided by the binary semi-major axis ($r = R/a$), the system inclination, the orbital period, the mid-eclipse timing, and the strength of the reflected light as a fraction of total system light. Here we present our light curve fitting results to these seven binaries. Interestingly, one of our binaries (J2036+2350) returns a best-fitting model light curve suggesting that the fainter secondary star is 1.5 times larger than the brighter primary.

ZTF J011339.09+225739.12

ZTF J011339.09+225739.12 (J0113+2257; PTF1 J011339.09+225739.10) was first identified by Kao et al. (2016) as a part of a search for variability in the Palomar Transient Factory data archive. Their analysis suggested that this system contains a subdwarf B (sdB) star with an M dwarf companion. Through model atmosphere fitting, the authors showed that the subdwarf has atmospheric parameters $T_{\rm eff} = 29,980$ K and $\log g = 5.69$. They obtained a most probable orbital period of $P = 2.24$ h (134.4 min) based on the modulation caused by the measured reflection effect. Gaia parallax places this system at a distance of $d_\pi = 2.4 \pm 0.4$ kpc. J0113+2257 is a part of the Geier et al. (2019) hot subluminous star catalogue.

Our analysis of the ZTF r-band light curve suggested that this system's components can be described by the its fractional component radii $r_B + r_A = 0.451 \pm 0.005$, $r_B/r_A = 0.79 \pm 0.02$, inclination $i = 81.1 \pm 0.4^\circ$, fraction of reflected light compared to total system light $A_{\rm secondary} = 0.103 \pm 0.002$ and orbital period $P = 134.45710 \pm 0.00002$ min

(2.24 h). We measured the mid-eclipsing timing within our fitted model to be $T_0 = 2458423.76151^{+0.00003}_{-0.00004}$ HJD. Additional spectroscopic follow-up will allow constraints to the mass of the primary through spectroscopic analysis and the mass and temperature of the companion through radial velocity variations and the combined spectroscopic temperature and measured reflection effect.

ZTF J072455.75+125300.36

ZTF J072455.75+125300.36 (J0724+1253; PTF1 J072455.75+125300.3) was first identified by Schindewolf et al. (2015). Their photometric and spectroscopic observations showed that this system contains sdB primary with an M-dwarf companion with an orbital period of $P = 0.09980$ d (143.7 min), inclined at $i = 83.56 \pm 0.30°$. They performed spectroscopic model fitting and obtained best-fitting atmospheric parameters $T_{\rm eff} = 33,900 \pm 350$ K, $\log g = 5.74 \pm 0.08$, and $\log n_{\rm He}/n_{\rm H} = -2.02 \pm 0.07$ for the sdB. Light curve modeling allowed the authors to constrain the parameters of the secondary M-dwarf to $M_2 = 0.155 \pm 0.020$ $M_\odot$, $R_2 = 0.165 \pm 0.015$ $R_\odot$, and $T_{\rm eff,2} = 3300 \pm 300$ K. Our fits to the ZTF r-band light curve agree within 1σ of the published values of Schindewolf et al. (2015) (see Table 5.4). J0724+1254 is a part of the Geier et al. (2019) hot subluminous star catalogue.

ZTF J203627.7345+235022.5994

ZTF J203627.7345+235022.5994 (J2036+2350) is an eclipsing binary with an orbital period $P = 518$ min at a distance of $d_\pi = 2.4 \pm 0.4$ kpc based on Gaia eDR3 parallax measurements. We perform light curve fitting to the ZTF r-band light curve of J2036+2350

using JKTEBOP and obtain estimates for its inclination ($i = 83.2^{+0.5\circ}_{-0.4}$), reflected light contribution ($Refl = 8.2 \pm 0.1\%$), and sum ($r_B + r_A = 0.232 \pm 0.004$) and ratio ($r_B/r_A = 1.504^{+0.2}_{-0.1}$) of fractional radii. Interestingly, this system's best-fit light curve suggests the fainter secondary is 1.5 times larger than the brighter primary star. Given its distance, this system is unlikely to be a white dwarf binary.

ZTF J213141.4392+465430.0224

ZTF J213141.4392+465430.0224 (J2131+4654) is an eclipsing HW Virginis type binary with an orbital period $P = 187.15$ min at a distance $d_\pi = 2.5 \pm 0.5$ kpc. Perhaps due to its companion contributing a non-insignificant amount of light to the system, J2131+4654 is not listed in the Gaia DR2 catalogue of hot subluminous stars of Geier et al. (2019). We obtained two optical spectrum of J2131+4654 using the MMT blue channel spectrograph on UT 2019 June 08 and one optical spectrum on UT 2019 June 09 using the 832 lines mm^{-1} grating and 1.5 arcsec slit. Between these three optical spectra, we measured radial velocities of $K = -58 \pm 15$ km s^{-1},$K = -1 \pm 14$ km s^{-1}, and $K = -78 \pm 16$ km s^{-1} separated by 78 minutes and 1443 minutes, respectively. Figure 5.9 displays the combined optical spectrum for J2131+4654. In addition to the broad Balmer lines, strong Helium absorption features are also present. J2131+4654 is not found in the Geier et al. (2019) hot subluminous star catalogue.

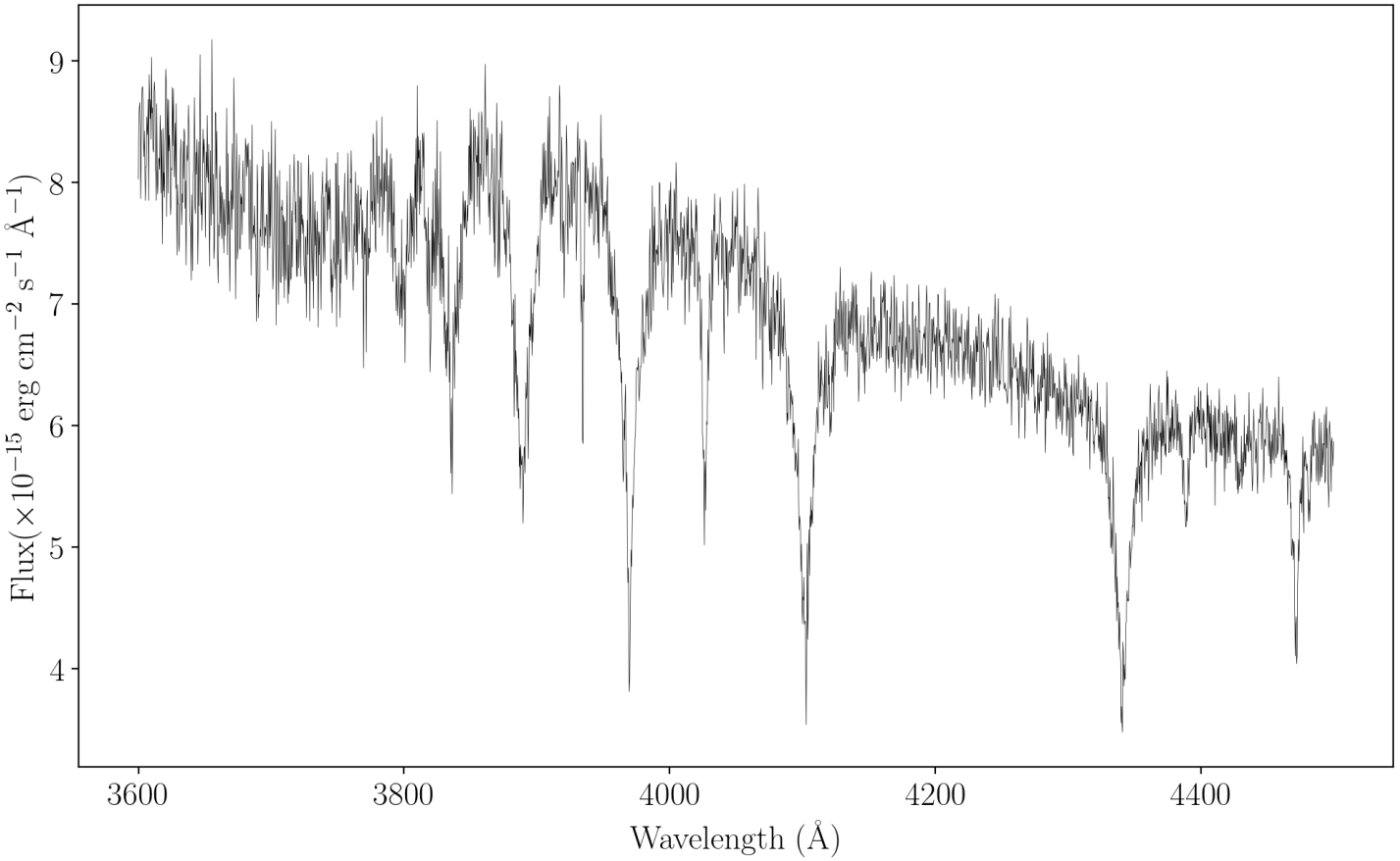

Fig. 5.9.— Combined MMT 6.5-meter optical spectrum of J2131+4654.

In addition to these four previously mentioned binaries, we present the results of our ZTF r-band light curve analysis to the remaining seven binaries in Table 5.4. Figure 5.10 shows the best-fitting model light curve overplotted onto the ZTF r-band light curve for each binary fitted here.

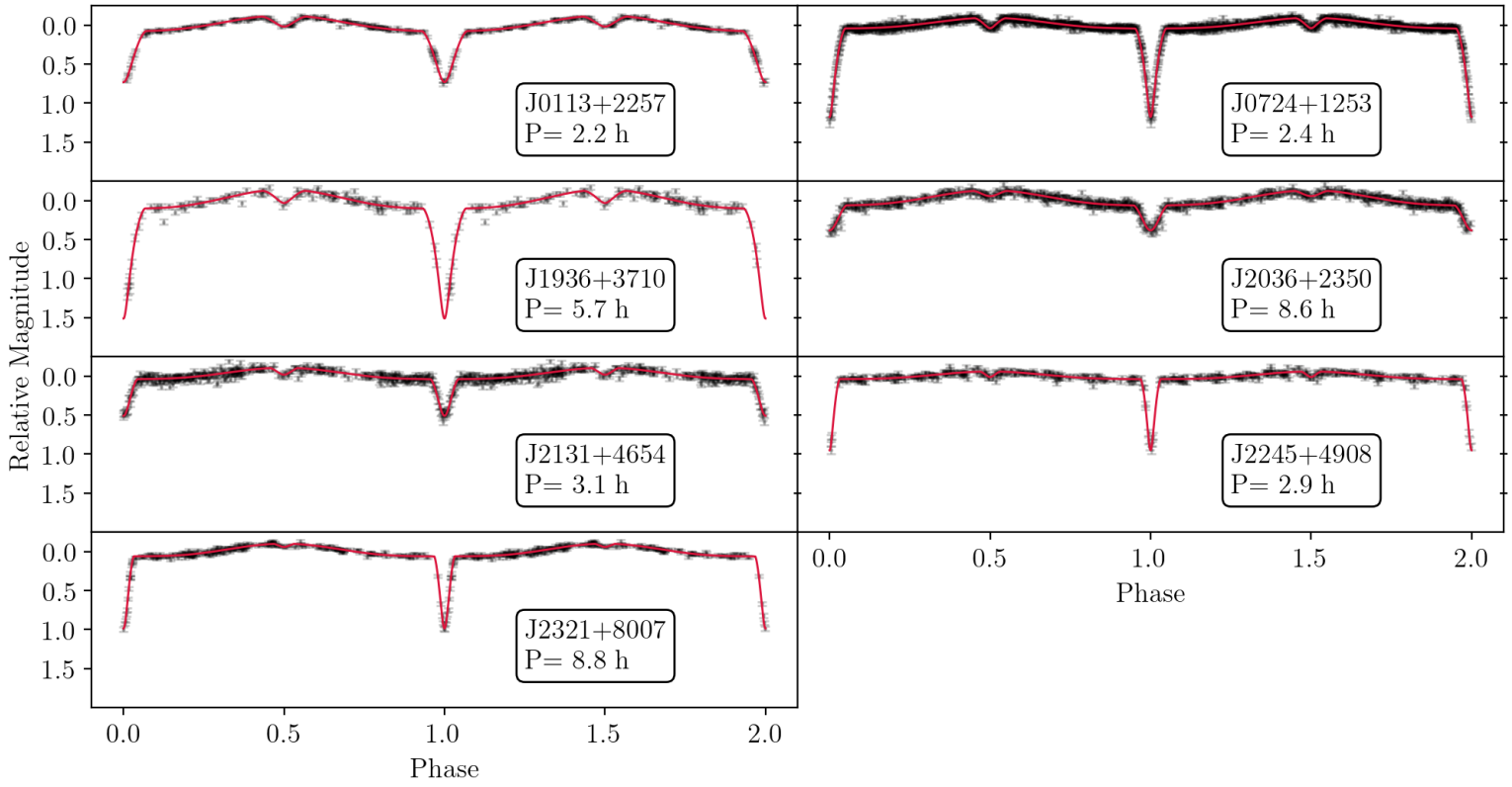

Fig. 5.10.— Phase folded ZTF DR4 *r*-band light curves to seven of the ten eclipsing subdwarf binaries identified in this work. The best-fitting model (red) is overplotted onto the phase-folded ZTF *r*-band light curve (black) for each binary.

Table 5.4:: Median values to the distributions for each of our fitted parameters to the ZTF r-band light curves of the ten eclipsing sdB+M binaries identified in this work. The 1σ lower and upper parameter bounds are reported as the 15.87 and 84.13 percentiles of each distribution. Targets marked with a † were identified in previous work. Targets marked with a ‡ are present in the Geier et al. (2019) catalogue of hot subluminous stars.

Gaia eDR3 ID	R.A.	Dec.	$\frac{R_B+R_A}{a}$	$\frac{R_B}{R_A}$	Inclination (°)	Reflection (‰)
3805609416774247 68‡	00:33:52.6266	+38:55:29.6670	···	···	···	···
414813439007636352	00:45:02.3617	+50:34:08.2794	···	···	···	···
2791084432881749760†‡	01:13:39.0901	+22:57:39.1176	0.451 ± 0.005	0.79 ± 0.02	81.1 ± 0.4	10.3 ± 0.2
3453995450857025664‡	06:09:14.3856	+36:52:02.8351	···	···	···	···

Continued on next page

Table 5.4 – continued from previous page

Gaia eDR3 ID	R.A.	Dec.	$\frac{R_B+R_A}{a}$	$\frac{R_B}{R_A}$	Inclination (°)	Reflection (%)
3163190946185170816†‡	07:24:55.7500	+12:53:00.3644	0.42 ± 0.01	$1.01^{+0.05}_{-0.04}$	84.6 ± 0.9	12.6 ± 0.4
2048949573450878336†‡	19:36:04.8805	+37:10:17.2348	0.298 ± 0.008	$0.748^{+0.05}_{-0.04}$	$82.7^{+0.6}_{-0.7}$	7.3 ± 0.2
1819387836386252672	20:36:27.7345	+23:50:22.5994	0.232 ± 0.004	$1.504^{+0.2}_{-0.1}$	$83.2^{+0.5}_{-0.6}$	8.2 ± 0.1
1978219536621659136	21:31:41.4392	+46:54:30.0224	0.303 ± 0.002	0.81 ± 0.02	$87.5^{+0.6}_{-0.5}$	6.7 ± 0.1
1988448022719912960†‡	22:45:47.3689	+49:08:24.6865	0.39 ± 0.01	$0.79^{+0.05}_{-0.04}$	77.5 ± 0.7	10.0 ± 0.2
2283172389416472320†‡	23:21:02.5469	+80:07:29.5028	$0.205^{+0.006}_{-0.007}$	$0.87^{+0.07}_{-0.06}$	86.7 ± 0.6	4.7 ± 0.1

5.3.6 Deeply-Eclipsing White Dwarf Systems

In an attempt to identify white dwarfs with substellar companions that survived common envelope evolution, our BLS search identified nine deeply-eclipsing systems that show eclipse depths near or beyond the ZTF detection limit in one or more filters. We follow-up four of these binaries with periods less than $P = 3$ h to estimate the companion masses and radii. Based on their orbital periods, eclipse durations, SEDs, and our follow-up analysis of four of these systems, the deeply eclipsing binaries identified here likely contain white dwarfs with low mass M-dwarf companions. The public ZTF DR4 light curves to these nine binaries, phase-folded to their most probable orbital periods obtained from our BLS search, are presented in Figures 5.11 & 5.12. Table 5.5 presents the basic astrometry for each of these nine binaries. Among these nine binaries, ZTF J110805.3890+652211.4407 (J1108+6522) was first identified by Silvestri et al. (2006) (see also Rowan et al., 2019) as an eclipsing DA white dwarf in a binary with a main sequence star of spectral class M6. Here we report on our photometric and spectroscopic follow-up analysis to four of these binaries.

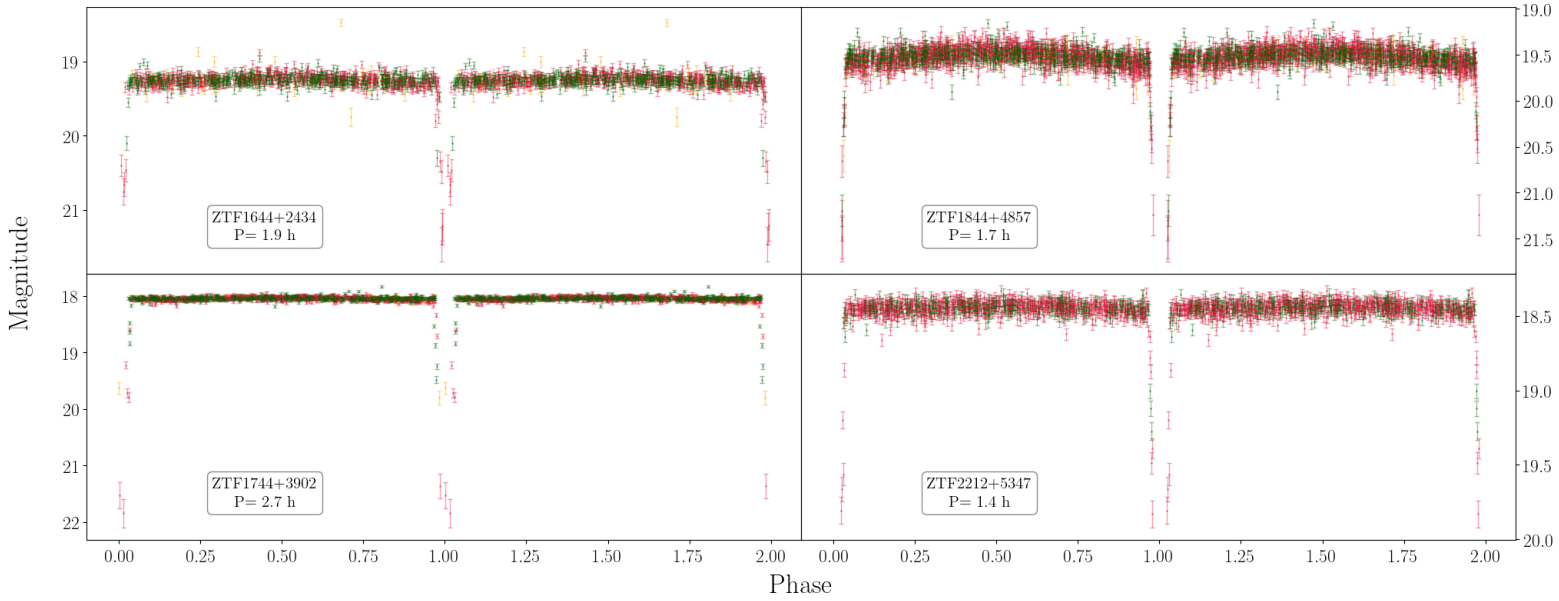

Fig. 5.11.— ZTF public DR4 light curves for four of the long-period eclipsing binaries identified in this work. Each light curve has been phase-folded to its most probable period, obtained through our BLS variability search. Individual data points are colored based on which ZTF filter they were observed with: green points were measured with ZTF g-band filter, red points were measured with ZTF r-band filter, and orange points were measured with the ZTF i-band filter. Filters have been median combined to the median value of the ZTF g-band filter.

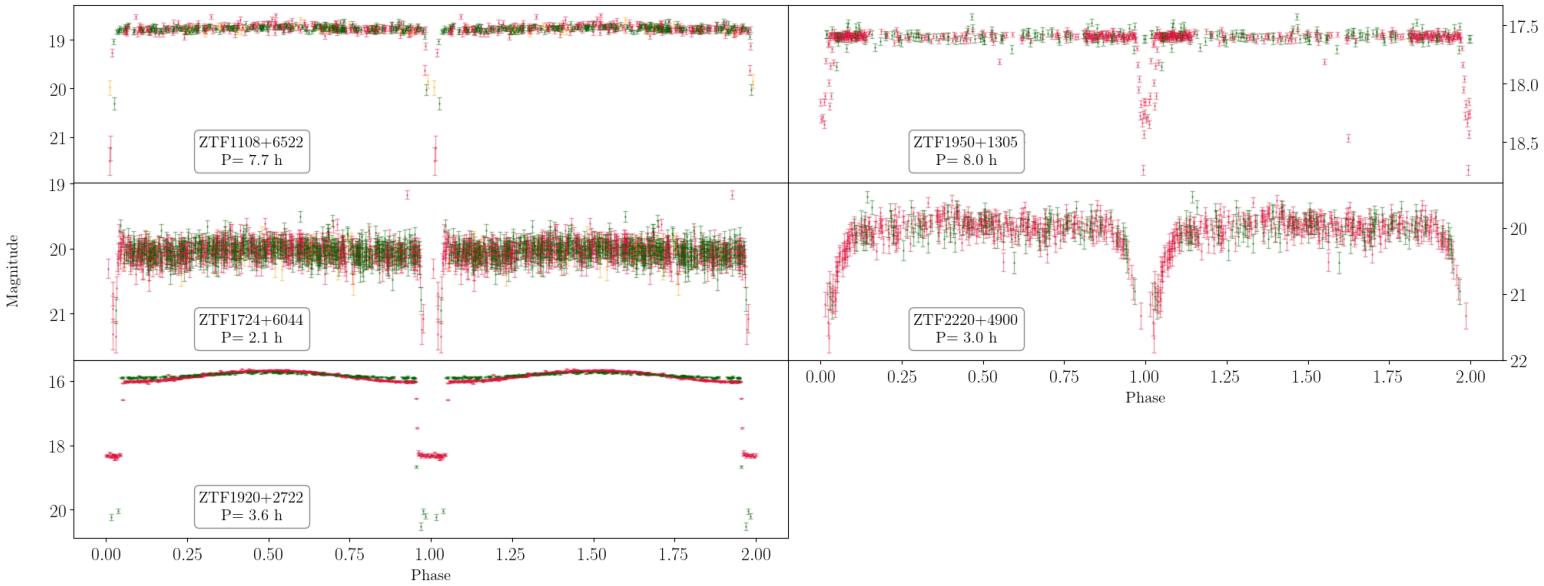

Fig. 5.12.— ZTF public DR4 light curves for five of the long-period eclipsing binaries identified in this work. Each light curve has been phase-folded to its most probable period, obtained through our BLS variability search. Individual data points are colored based on which ZTF filter they were observed with: green points were measured with ZTF g-band filter, red points were measured with ZTF r-band filter, and orange points were measured with the ZTF i-band filter. Filters have been median combined to the median value of the ZTF g-band filter.

Table 5.5:: Basic system information for the nine deeply-eclipsing, likely white dwarf + main sequence, binaries identified in this work. Distance values are based on the Gaia eDR3 parallax and its uncertainty. J1108+6522 was previously identified by Silvestri et al. (2006).

Gaia eDR3 ID	R.A.	Dec.	Gaia G (mag)	Distance (pc)	Period (h)
2004624931143291648	22:12:26.9672	+53:47:50.6967	18.28	195 ± 4	1.40
2119978952315202176	18:44:34.3978	+48:57:36.5063	19.29	794 ± 133	1.74
1300187622427241856	16:44:41.1946	+24:34:28.2112	19.09	412 ± 38	1.92
1438919253678919040	17:24:00.0555	+60:44:51.8788	20.03	689 ± 221	2.13
1343069434903597952	17:44:24.7141	+39:02:15.6653	17.84	242 ± 5	2.70
1999661044159004288	22:20:13.9165	+49:00:06.0340	19.84	967 ± 416	3.04

Continued on next page

Table 5.5 – continued from previous page

Gaia eDR3 ID	R.A.	Dec.	Gaia G (mag)	Distance (pc)	Period (h)
2025873096433233664	19:20:14.1409	+27:22:18.0903	15.56	192 ± 1	3.58
1055977736185041024	11:08:05.3890	+65:22:11.4407	18.50	519 ± 42	7.70
4305212584032932352	19:50:24.4076	+13:06:45.4761	17.72	···	8.02

ZTF J164441.1946+243428.2112

ZTF J164441.1946+243428.2112 (J1644+2434) is an eclipsing white dwarf with a low-mass stellar companion on an orbital period of $P = 1.922$ h. While the eclipse depth is unmeasured in the ZTF g-band, the ZTF r-band light curve shows an eclipse depth of about 1.5 mag, suggesting that the companion is a low-mass stellar object, rather than a substellar object such as a brown dwarf. Figure 5.13 (top-left) displays the SED of J1644+2434, which shows an excess of flux in the Pan-STARRS i-, z-, and y-bands and WISE $W1$ and $W2$ bands. We fit the de-reddened optical component of this SED with single-star pure-hydrogen white dwarf models and obtain a primary mass $M_1 = 0.551$ M$_\odot$, effective temperature $T_{\rm eff} = 14,300$ K, and surface gravity $\log g = 7.89$. We extracted the companion's contribution from this SED and use Baraffe et al. (2015) low-mass M-dwarf stellar models to estimate the mass of the secondary to be $M_2 \approx 0.1$ M$_\odot$. Based on Gaia eDR3 parallax measurements, this system is at a distance of $d_\pi = 412 \pm 38$ pc.

We obtained APO 3.5-meter BG40 broadband photometry of ZTF J1644+2434 on UT 2021 April 03 and UT 2021 April 04 covering one primary eclipse on each night. We performed data reduction and circular aperture photometry, with variable aperture size based on the average FWHM of each image, using IRAF. We combined the two APO light curves and fit the combined light curve using JKTEBOP to obtain estimates for the system component radii and orbital inclination. We used quadratic limb darkening values from Claret et al. (2020) for a $\log g = 8.0$, $T_{\rm eff} = 14,000$ K DA white dwarf primary. We present the best-fitting model light curve parameters in Table 5.6 and display the parameter distributions and best-fitting light curve overplotted onto our APO BG40 light curve in Figure 5.14.

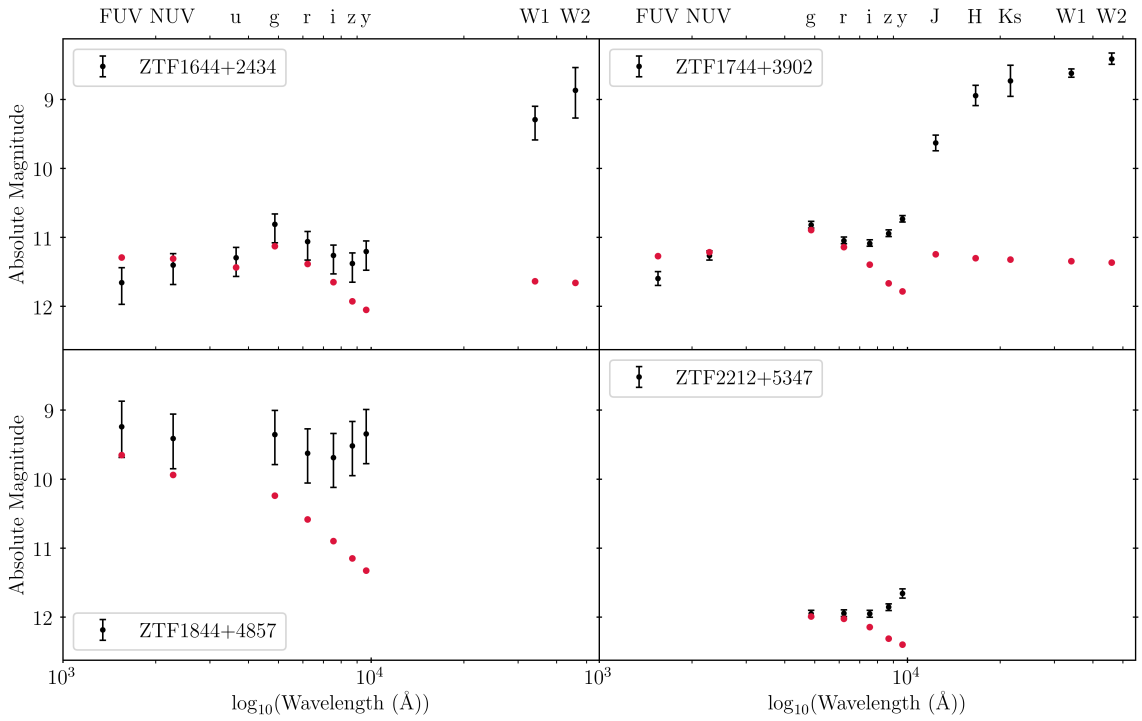

Fig. 5.13.— Spectral energy distributions for the four deeply-eclipsing white dwarf binaries followed-up in this work. Black points represent observed, extinction-corrected. absolute magnitudes. We use the photogeometric distances of Bailer-Jones et al. (2021) to calculate the absolute magnitude values. Red points represent the best-fit, pure-hydrogen, atmospheres model SED for a single white dwarf. Each object shows an excess of flux in redder filters, suggesting a low-mass stellar companion, rather than a massive substellar companion. GALEX UV, SDSS u, and Pan-STARRS $grizy$ photometry use the AB-magnitude system while the redder 2MASS J,H,K_S and WISE W1 and W2 are in the Vega-magnitude system.

Table 5.6: Median values to the distributions for each of our fitted parameters to the APO BG40 broadband, r-band, and i-band light curves for the four deeply-eclipsing white dwarf + main sequence binaries identified in this work. The 1σ lower and upper parameter bounds are reported as the 15.87 and 84.13 percentiles of each distribution. Inclination for J2212+5347 was constrained using a method similar to Parsons et al. (2017a). See text for details.

Gaia eDR3 ID	RA (J2000)	Dec (J2000)	$\frac{R_B+R_A}{a}$	$\frac{R_B}{R_A}$	Incl (°)	R_A ($R_\odot$)	R_B ($R_\odot$)
1300187622427241856	16:44:41.1946	+24:34:28.2112	0.26 ± 0.02	8.1 ± 2.1	$78.7^{+2.1}_{-1.8}$	···	···
1343069434903597952	17:44:24.7141	+39:02:15.6653	0.253 ± 0.002	12.3 ± 0.2	81.8 ± 0.2	···	···
2119978952315202176	18:44:34.3978	+48:57:36.5063	0.306 ± 0.03	$7.8^{+2.1}_{-1.8}$	78.0 ± 2.5	···	···
2004624931143291648	22:12:26.9672	+53:47:50.6967	0.28 ± 0.02	$6.3^{+1.3}_{-1.0}$	$79.4^{+1.5}_{-1.7}$	0.019 ± 0.009	0.12 ± 0.01

We obtained APO 3.5-meter optical spectroscopy follow-up of ZTF J1644+2434 on UT 2021 April 09 using Dual Imaging Spectrograph (DIS) with the low resolution R400 (2.31 Å px^{-1}) and B300 (1.83 Å px^{-1}) gratings and the 1.5 arcsec slit. Figure 5.15 displays our single APO blue-optical spectrum for ZTF J1644+2434 using an exposure time of 1800 s. We performed model atmosphere fits to this spectrum using a grid of pure hydrogen white dwarf model atmospheres and obtain best-fitting parameters $\log g = 7.89 \pm 0.14$ and $T_{\rm eff} = 14,900 \pm 700$ K, in agreement with our photometric fit. Our best-fitting model is presented in Figure 5.16. Using the photometric mass and radius obtained through eclipse light curve fitting, we estimate its radius to be $R_1 = 0.015 \pm 0.002$ $R_\odot$. This value agrees nearly perfectly with the evolutionary models for thick hydrogen layer ($q_{\rm H} = 10^{-4}$) DA white dwarf evolutionary sequences[1] of Bédard et al. (2020) for a 0.55 $M_\odot$ DA white dwarf with $T_{\rm eff} = 14,831$ K and $\log g = 7.89$ at $R_1 = 0.015$ $R_\odot$.

J1644+2434 was simultaneously identified by Keller et al. (2021) in their BLS search for short period white dwarf binaries in the public ZTF data release 3 archive. The authors' analysis suggests that J1644+2434 contains a low-luminosity companion on an orbital period of $P = 115.35$ min.

[1]https://www.astro.umontreal.ca/~bergeron/CoolingModels/

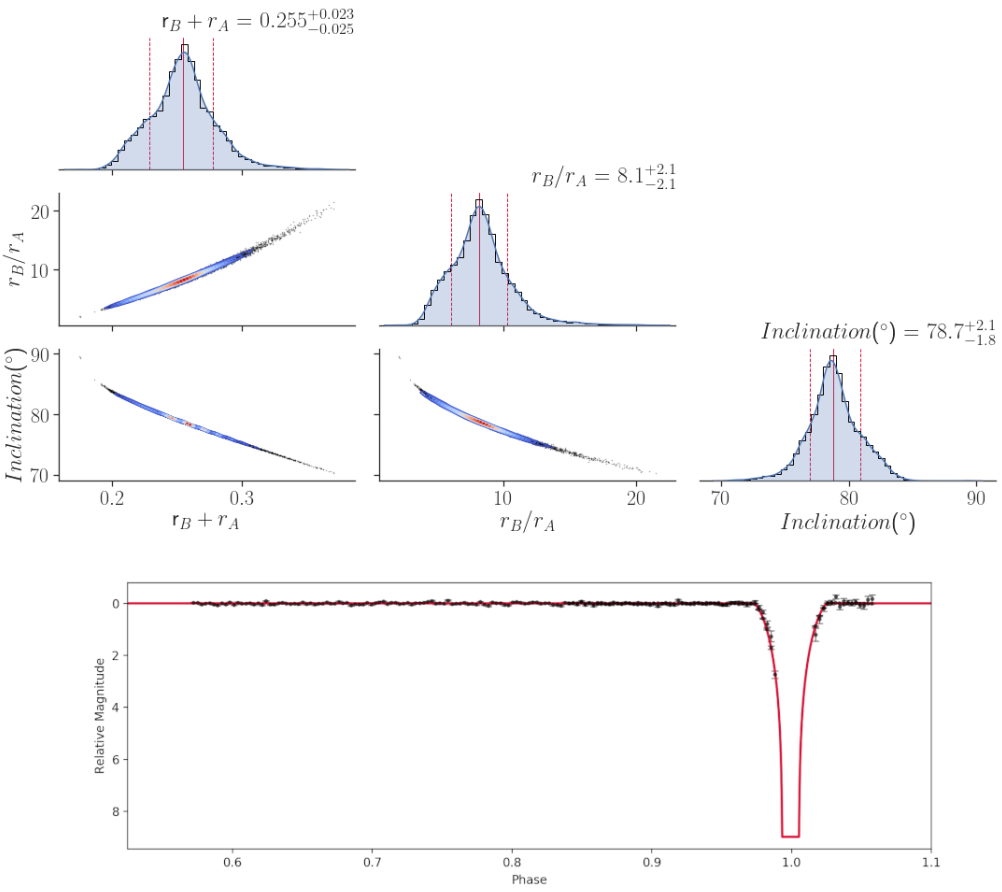

Fig. 5.14.— Top: Corner plot showing the 1-D parameter distributions for our 10,000 Monte Carlo fits to the APO BG40 light curve of J1644+2434 on the diagonal and the 2-D distributions on the off-diagonal. Bottom: APO BG40 light curve for J1644+2434 (black) with the best-fit model overplotted in red.

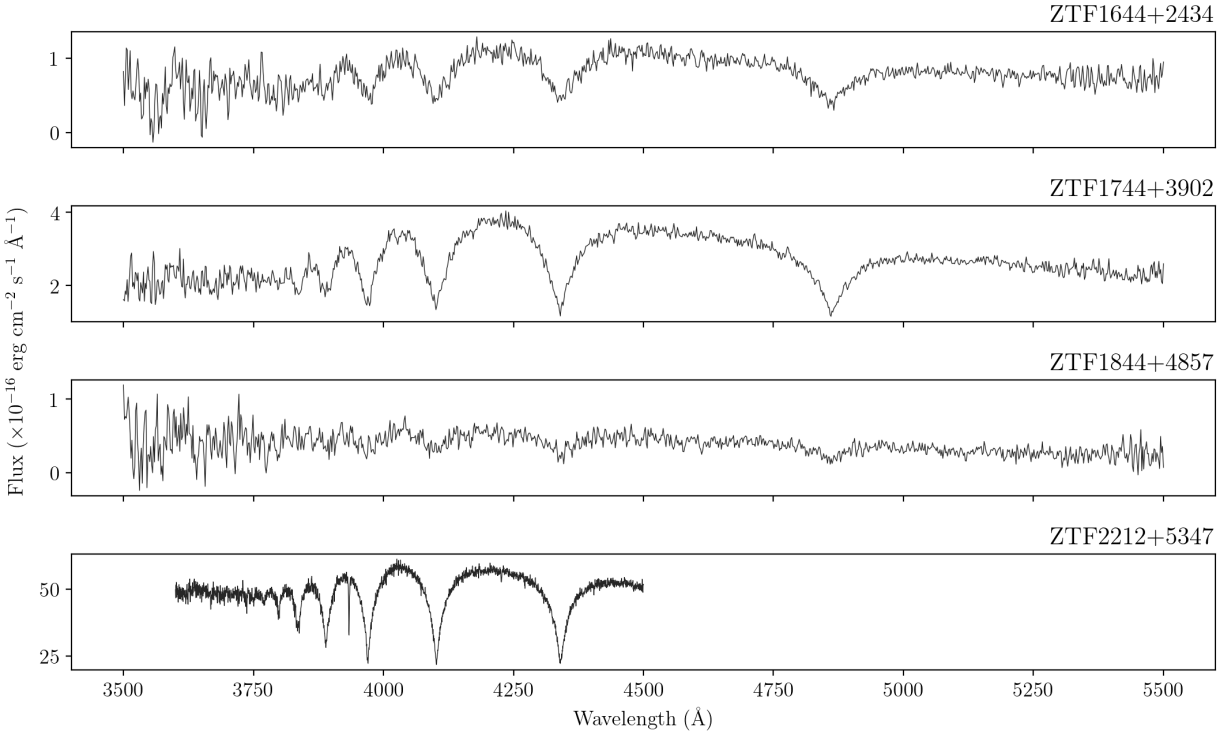

Fig. 5.15.— Follow-up optical spectra for four of the deeply-eclipsing white dwarf binaries identified in this work. Optical spectra for J1644+2434, J1744+3902, and J1844+4857 were obtained using the APO 3.5-meter telescope's Dual Image Spectrometer (DIS). The optical spectrum for J2212+5347 was obtained with the MMT 6.5-meter telescope's blue channel spectrograph.

ZTF J174424.7141+390215.6653

ZTF J174424.7141+390215.6653 (J1744+3902) is a white dwarf in a binary with a low mass main sequence companion with an orbital period of $P = 2.700$ h. The ZTF light curve shows ≈ 2 mag deep eclipses in the ZTF i-band light curve, ≈ 3.5 mag deep eclipses in the ZTF r-band, and unmeasured eclipse depth in the ZTF g-band. Figure 5.13 (top-right) displays the SED of J1744+3902. The SED shows a clear flux excess in the Pan-STARRS $i-$, $z-$, and $y-$bands, the 2MASS J, H, and K_s bands, and the WISE $W1$ and $W2$ bands. We fit the optical component of the SED to J1744+3902 and obtained $M_1 = 0.429$ M$_\odot$, $T_{\rm eff} = 13,500$ K, and $\log g = 7.65$ as best-fit parameters. Based on Gaia eDR3 parallax measurements, J1744+3902 is at a distance of $d = 242 \pm 5$ pc.

We obtained APO 3.5-meter SDSS $r-$band photometry of J1744+3902 on UT 2021 April 03 and UT 2021 April 04 and i-band photometry on UT 2021 April 09, with each night covering one primary eclipse. We fit the light curves for each filter separately using JKTEBOP and obtain estimates on the component radii and orbital inclination. We used quadratic limb darkening coefficients from Claret et al. (2020) for a $\log g = 7.75$, $T_{\rm eff} = 13,500$ K DA white dwarf. Our best-fitting sum of radii and inclination agree within 1σ between the two filters with average values of $r_B + r_A = 0.252 \pm 0.002$ and $i = 81.8 \pm 0.2°$. However, the best-fitting ratio of the radii do not agree across filters with median-distribution values of $(r_B/r_A)_{rband} = 12.3 \pm 0.2$ and $(r_B/r_A)_{iband} = 13.1 \pm 0.2$. This discrepancy is likely due to the low signal-to-noise photometry during the eclipse caused by the high background levels on the night of the observations, causing the fitting algorithm to under-estimate the true eclipse depths between the two filters. Best-fit model

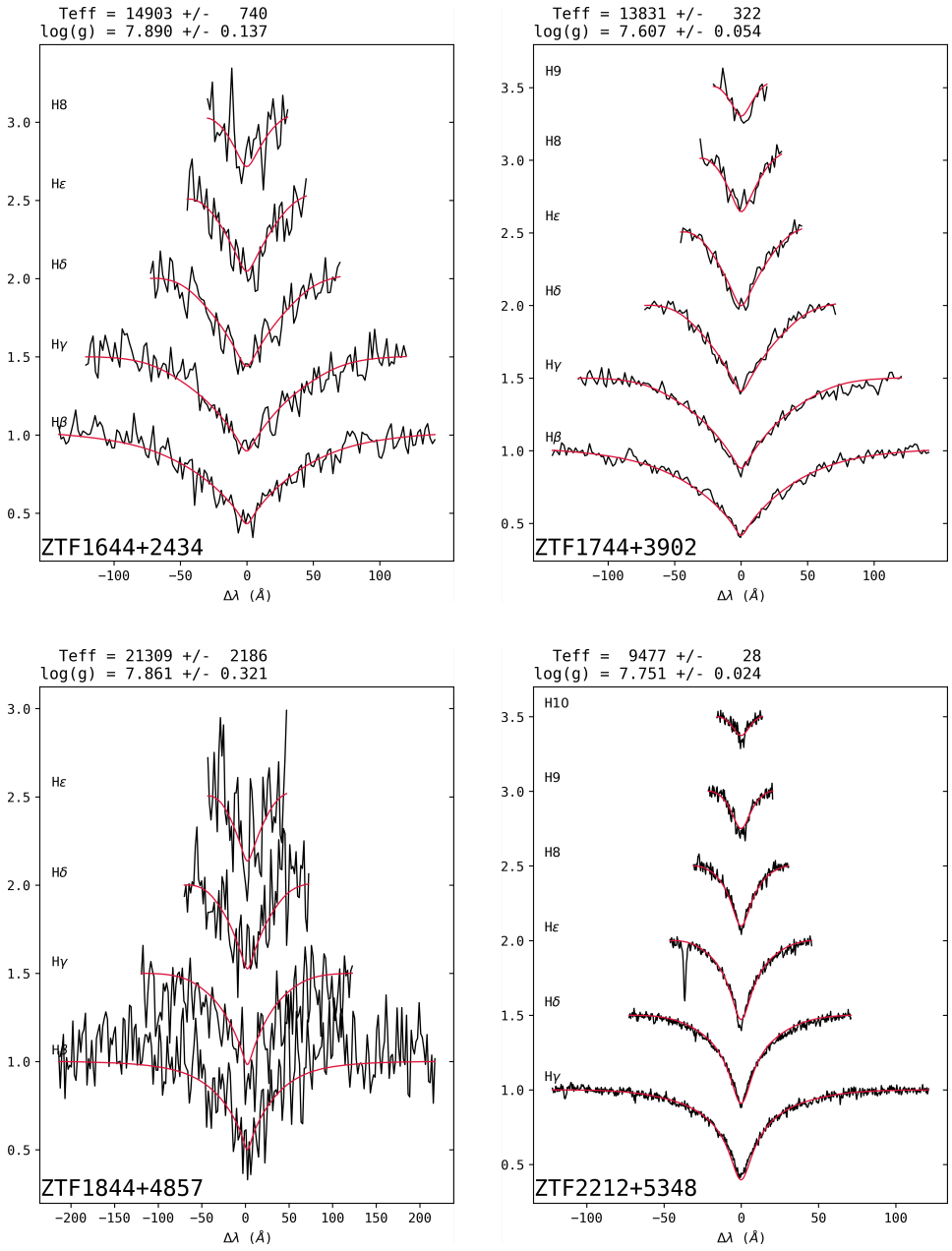

Fig. 5.16.— Model atmosphere fits to four of the deeply-eclipsing white dwarf binaries followed-up in this work.

parameter distributions and the phase-folded light curves for the APO r- and i-bands are presented in Figures 5.17 & 5.18, respectively.

We obtained APO 3.5-meter spectroscopic follow-up of J1744+3902 on UT 2021 April 09 using DIS with the low resolution R400 and B300 gratings and the 1.5 arcsec slit. Our spectroscopic follow-up consisted of a single 30-minute exposure. We reduced the data using standard procedures with IRAF. The blue-optical spectrum for J1744+3902 is presented in Figure 5.15. We performed model atmosphere fitting using a grid of pure hydrogen white dwarf model atmospheres and obtain best-fit model atmosphere parameters of $\log g = 7.61 \pm 0.05$ and $T_{\rm eff} = 13,800 \pm 300$ K, in agreement with our photometric fits. Our best-fitting atmosphere model is overplotted onto the Balmer lines of our APO spectrum in Figure 5.16. We used these parameters to estimate the primary radius as $R_1 = 0.018 \pm 0.001$ $R_\odot$, roughly in agreement with the radius for from Bédard et al. (2020) of $R_1 = 0.017$ $R_\odot$ for a 0.45 $M_\odot$, $T_{\rm eff} = 13780$ K and $\log g = 7.69$ DA white dwarf.

ZTF J184434.3978+485736.5063

ZTF J184434.3978+485736.5063 (J1844+4857) is a white dwarf in a binary with a low-mass main sequence companion with an orbital period of $P = 1.744$ h. The true depth of the eclipse is undetected in all filters due to the magnitude limit of the ZTF instruments. We present the SED of J1844+4857 in Figure 5.13 (bottom-left), which shows a clear excess in the Pan-STARRS $grizy$ filters. We fit the optical component of the SED to J1844+4857 and obtain $M_1 = 0.452$ M$_\odot$, $T_{\rm eff} = 18,800$ K, and $\log g = 7.66$ as best-fit parameters. Based on Gaia eDR3 parallax measurements, this system is at a distance of $d = 794 \pm 133$ pc.

We obtained APO 3.5-meter BG40 broadband photometry of J1844+4857 on UT 2021 April 04 covering two consecutive primary eclipses with 20-second back-to-back exposures using the Agile high-speed photometer. We use JKTEBOP to fit the light curve and obtain estimates for the radii and orbital inclination. We present our resulting parameter distributions and best-fitting model light curve in Figure 5.19 and list our best-fitting model parameters in Table 5.6. However, because we do not detect the bottom of the eclipse in our fitted light curve, our estimates for the radii and inclination are based only on the eclipse duration and the shapes of the ingress and egress. Therefore, these parameters act as a lower limit to the true values.

We obtained APO 3.5-meter spectroscopic follow-up of J1844+4857 on UT 2021 April 09 using DIS with low resolution R400 and B300 gratings and the 1.5 arcsec slit. However, due to inclement weather, our exposure was cut short, and the signal to noise ratio suffered greatly. Further attempts to follow-up this target have failed due to

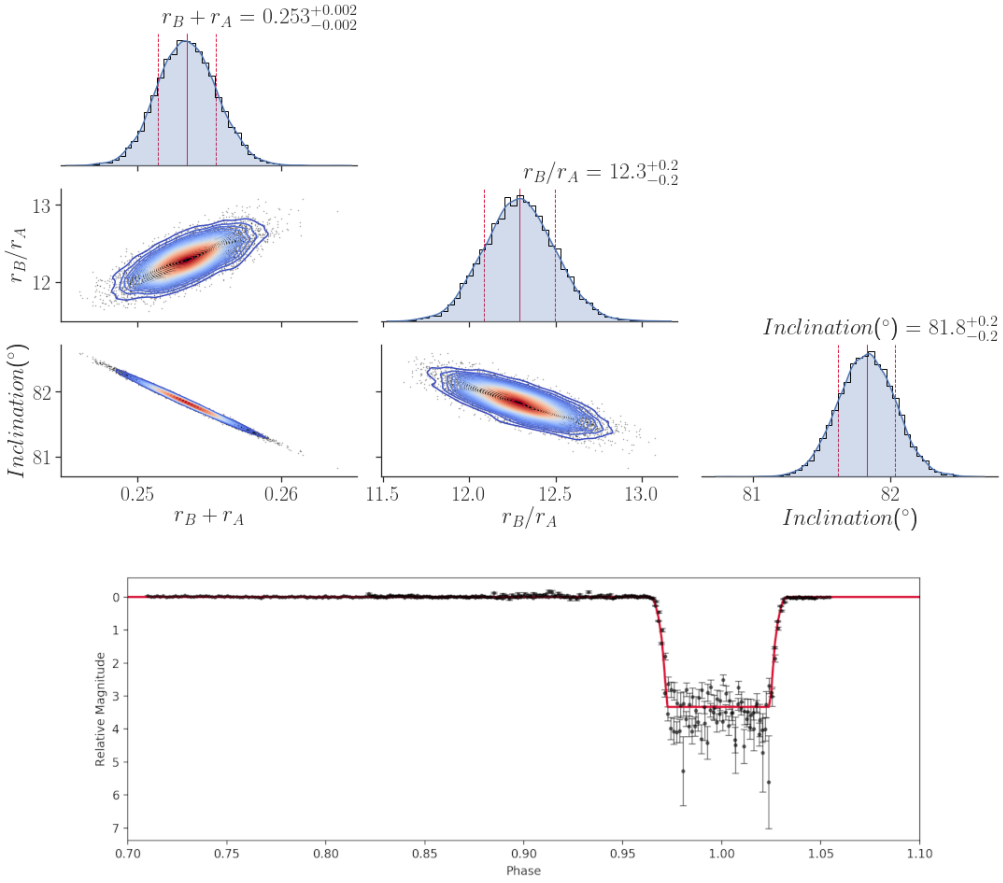

Fig. 5.17.— Top: Corner plot showing the 1-D parameter distributions for our 10,000 Monte Carlo fits to the APO r-band light curve for J1744+3902 on the diagonal and the 2-D distributions in the off-diagonal. Bottom: APO r-band light curve for J1744+3902 (black) with the best-fit model overplotted in red.

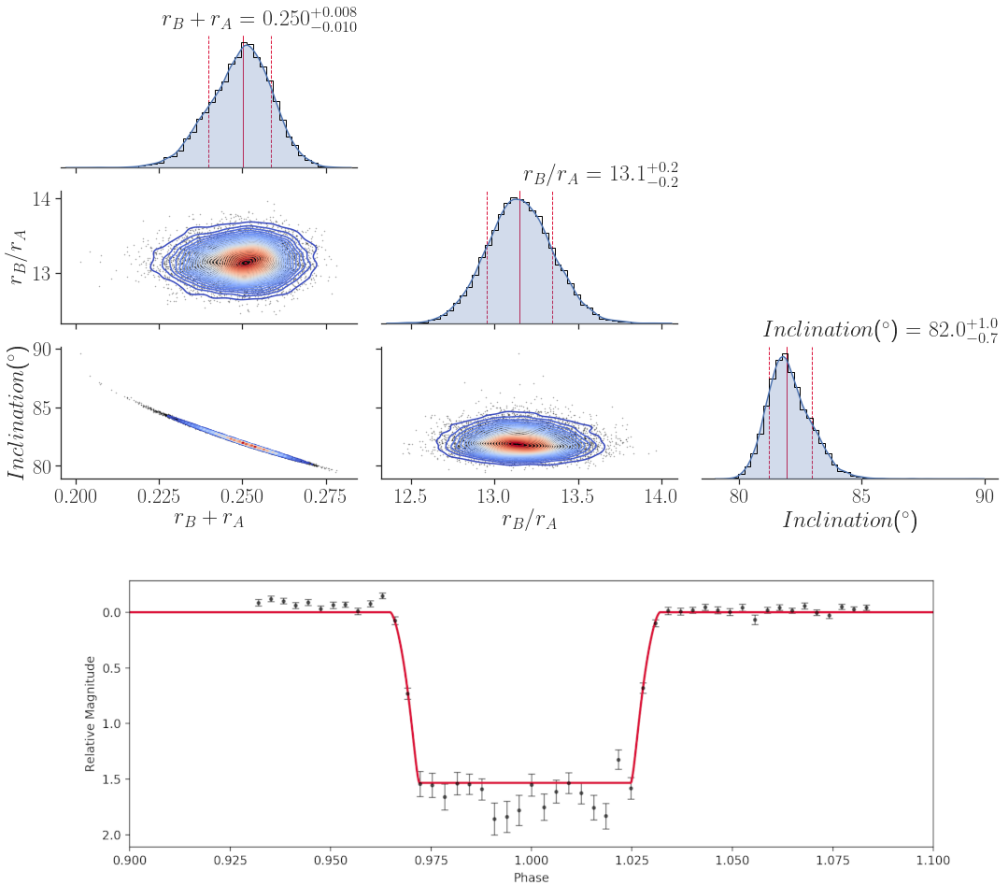

Fig. 5.18.— Top: Corner plot showing the 1-D parameter distributions for our 10,000 Monte Carlo fits to the APO *i*-band light curve for J1744+3902 on the diagonal and the 2-D distributions on the off-diagonal Bottom: APO *i*-band light curve for J1744+3902 (black) with the best-fit model overplotted in red.

inclement weather. Our APO blue-optical spectrum for J1844+4857 can be seen in Figure 5.15. We performed model atmosphere fitting using a grid of pure hydrogen white dwarf model atmospheres to obtain best-fit model atmosphere parameters of $\log g = 7.61 \pm 0.05$ and $T_{\rm eff} = 19,300 \pm 1600$ K. Our spectroscopic surface gravity agrees within 1σ of the photometric value. However, due to the low signal-to-noise level of our spectrum, we adopted the photometric solution as the correct solution. Using the photometric solution, we estimated the radius of the primary to be $R_1 = 0.017$ R$_\odot$, in agreement with the value from Bédard et al. (2020) evolutionary tracks of $R_1 = 0.0174$ R$_\odot$. We are currently working to obtain a high-quality optical spectrum to better constrain these parameters through spectroscopic analysis.

J1844+4857 was simultaneously identified by Keller et al. (2021) in their BLS search for short period white dwarf binaries in the public ZTF data release 3 archive. Their analysis showed that J1844+4857 has an orbital period of $P = 104.64$ min and an eclipse duration of 0.08 phase. The authors also suggested that the system contains a white dwarf with a main sequence companion.

ZTF J221226.9672+534750.6967

ZTF J221226.9672+534750.6967 (J2212+5347) is a white dwarf in a binary with a low-mass main sequence companion. J2212+5347 shows primary eclipse depths of > 1.5mag in the ZTF g- and r-bands with an orbital period of $P = 1.400$ h. The true depth of the eclipse is undetected due to the magnitude limit of the ZTF instrument. Figure 5.13 (bottom-right) shows the Pan-STARRS $grizy$ SED for J2212+5347. We fit this SED and obtain $M_1 = 0.439$ $M_\odot$, $T_{\rm eff} = 9430$ K, and $\log g = 7.70$ as best-fit parameters. The redder Pan-STARRS $i-$, $z-$, and $y-$band photometry shows a clear flux excess deviation from the single white dwarf models, suggesting the presence of a low mass main sequence star companion. Based on Gaia eDR3 parallax measurements, this system is at a distance of $d = 195 \pm 4$ pc.

We obtained 27 optical spectra of J2212+5347 between UT 2020 Dec 09 and Dec 16 using the 6.5-meter MMT telescope's blue channel spectrograph with the 1.25″ slit and 832 lines mm^{-1} grating. We created a barycentric-corrected zero-velocity summed spectrum by co-adding the 27 optical spectra with the SUMSPEC task within IRAF based on a zero-velocity low-mass white dwarf template spectrum. Figure 5.15 displays our summed spectrum of J2212+5347. We fit the combined spectrum with a grid of DA white dwarf models and obtain best-fit atmospheric parameters $T_{\rm eff} = 9480 \pm 30$ K and $\log g = 7.75$. Because cool white dwarfs fit with 1D model atmospheres return surface gravity values that are systematically too high (see Tremblay et al., 2011b), we applied a 3D correction to our best-fit solution and obtain the corrected values $T_{\rm eff} = 9420 \pm 30$ K and $\log g = 7.57 \pm 0.02$ corresponding to a primary white dwarf

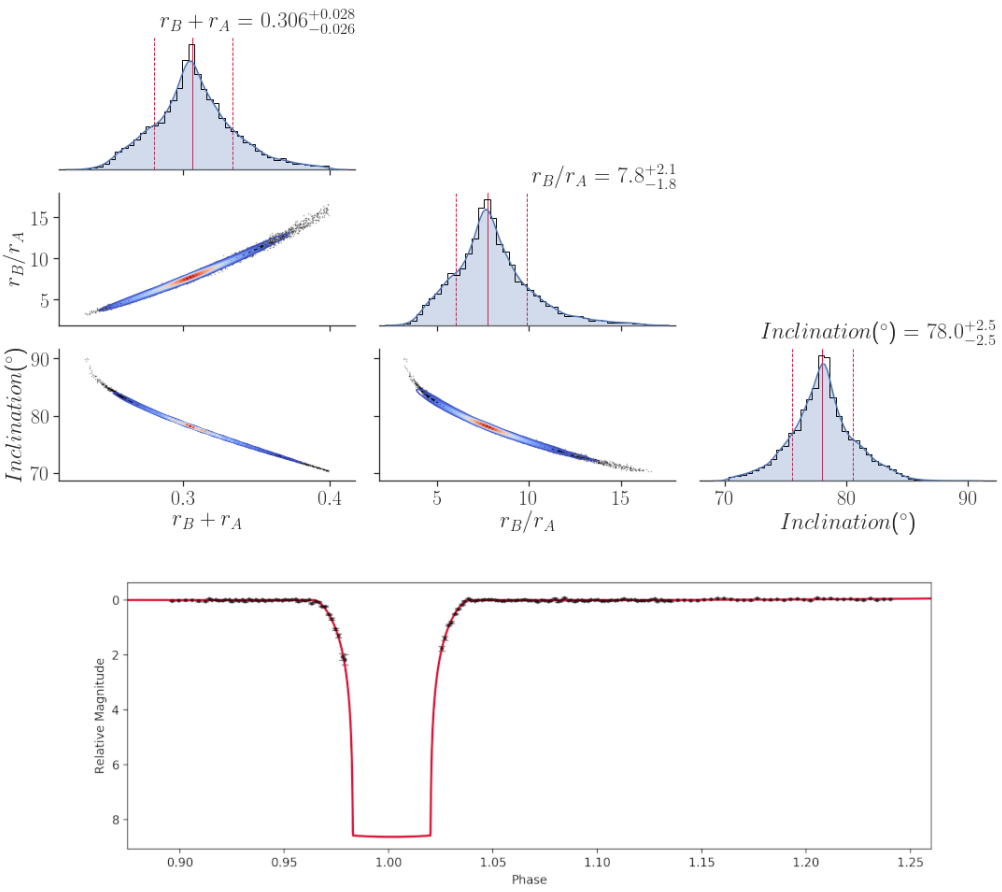

Fig. 5.19.— Top: Corner plot showing the 1-D parameter distributions for our 10,000 Monte Carlo fits to the APO BG40 light curve for J1844+4857 on the diagonal and the 2-D distributions on the off-diagonals. Bottom: APO BG40 broadband light curve for J1844+4857 (black) with the best-fit model overplotted in red.

mass of $M_{\rm WD} = 0.39 \pm 0.01$ M$_\odot$, based on C/O-core DA white dwarf cooling sequences of Fontaine et al. (2001). Given the low mass of this white dwarf, it is likely that the core of J2212+5347 contains a large fraction of Helium. Therefore, we also used the Althaus et al. (2013) He-core white dwarf models with our 3D correction and obtain as best fit corrected parameters $M_{\rm WD} = 0.40 \pm 0.02M_\odot$, $R_{\rm WD} = 0.017$, $L/L_\odot = -2.699$, and $d = 195$ pc. Remarkably, the distance derived from helium core white dwarf models exactly matches the distance derived from Gaia eDR3 parallax measurements.

We fit the radial velocity variations of J2212+5347 and applied the binary mass function to determine the minimum companion mass based on our estimated primary white dwarf mass. Our best-fit orbit to the radial velocity measurements returned a velocity semi-amplitude of $K = 82.5 \pm 4.2$ km s^{-1} on a period of $P = 1.4000 \pm 0.0001$ h with systemic velocity $\gamma = -33 \pm 3$ km s^{-1}. This velocity semi-amplitude suggests a minimum companion mass of $M_{2,\rm min} = 99 \pm 6$ M$_{\rm Jupiter}$ with an orbital inclination of $i = 90°$. This minimum mass is well above the upper mass limit expected for sub-stellar objects of around $M \approx 73 \sim 81$ M$_{\rm Jupiter}$ (Dieterich et al., 2014). Figure 5.20 shows the fit to our 27 radial velocity measurements for J2212+5347. A list of our radial velocity measurements is available in table 5.7.

Table 5.7:: List of radial velocity measurements for J2212+5347 obtained using the MMT 6.5-meter telescope's blue channel spectrograph.

HJD (−2450000 days)	Velocity (km s^{-1})	Error (km s^{-1})
9192.641711	-75.47	13.98
9192.646743	-114.66	16.15
9192.651777	-99.90	13.68
9192.656807	-105.96	14.24
9192.661835	-52.60	17.92
9192.666860	-8.11	16.05
9192.671886	-2.83	18.13
9192.676913	24.14	17.06
9192.682285	16.91	19.68
9192.688723	-8.18	16.37
9192.696543	-44.29	23.46
9195.652166	46.51	12.50
9195.659970	48.98	14.81
9195.668124	67.02	50.40
9198.644382	-30.09	29.73

Continued on next page

Table 5.7 – continued from previous page

HJD (−2450000 days)	Velocity (km s^{-1})	Error (km s^{-1})
9198.652949	-76.97	25.88
9199.597496	-113.44	14.12
9199.603251	-70.99	13.93
9199.608980	4.67	15.24
9199.614717	39.12	14.62
9199.620450	60.72	12.85
9199.626181	20.96	17.38
9199.631917	-0.69	12.54
9199.637655	-34.63	19.78
9199.643389	-100.21	14.21
9199.649134	-120.65	13.23
9199.654876	-104.55	14.16

We obtained APO 3.5-meter follow-up photometry on UT 2020 December 07 using the high-speed photometer, Agile, with the BG40 broadband filter. We obtained 380 minutes of back-to-back exposures in rapidly-varying sky conditions. Due to the sky conditions, our image PSF size varied from $\mathrm{FWHM_{PSF}} = 3.1 - 8.0$ px. We perform forced aperture photometry based on the average FWHM of each image using IRAF and

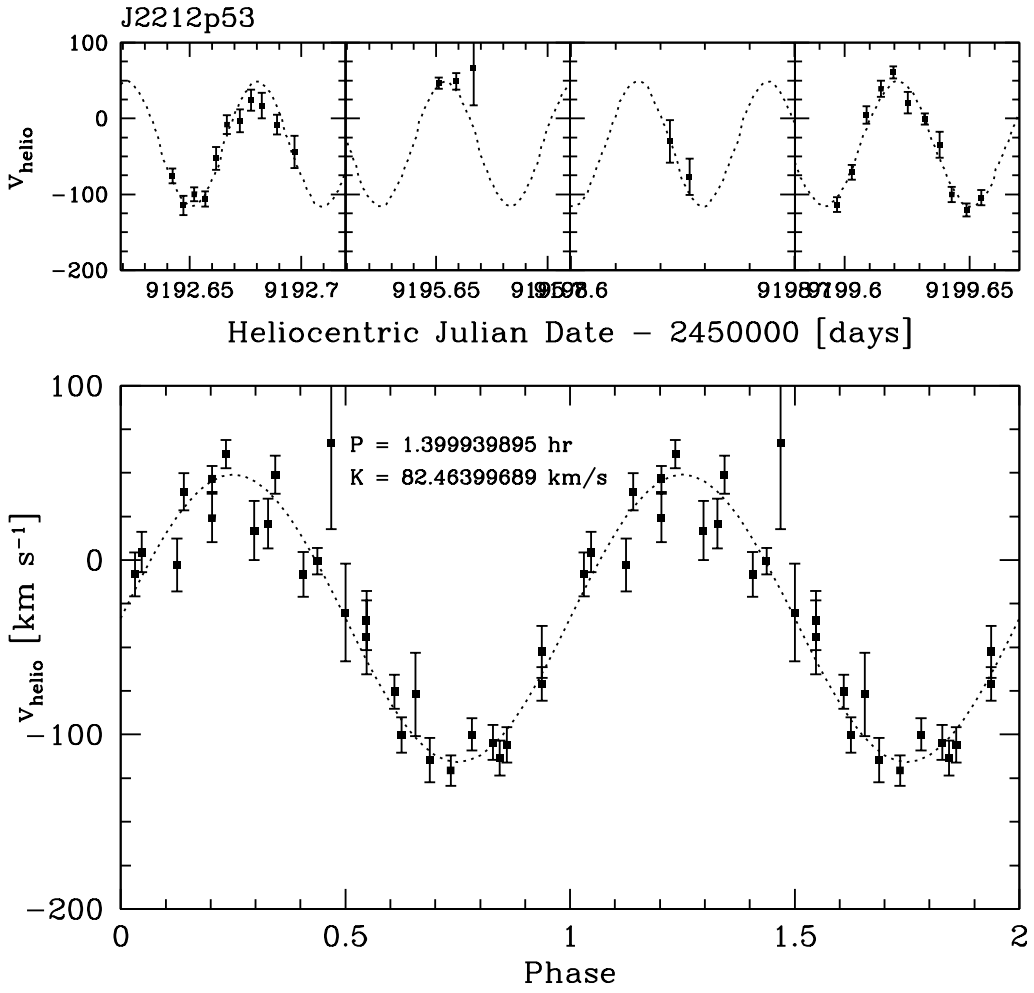

Fig. 5.20.— Orbital fit to J2212+5347.

fit the resulting light curve using JKTEBOP. We used Claret et al. (2020) quadratic limb darkening coefficients for a $\log g = 7.5$, $T_{\rm eff} = 9500$ K DA white dwarf and Claret et al. (2020) quadratic limb darkening for a $\log g = 3.5$, $T_{\rm eff} = 1600$ K companion, corrected to the BG40 bandpass using equation 3 of Hallakoun et al. (2016).

We followed a similar iterative procedure as found in Parsons et al. (2017b) to determine the best-fitting inclination and system component radii. In short: we performed 10,000 MC fits fitting for the sum and ratio of the fractional component radii while iterating the fixed inclination between 77 degrees and 90 degrees in steps of 1 degree. We used the binary mass function to determine the companion mass based from our MMT radial velocity measurements for each inclination. We then used Kepler's third law to determine the orbital semi-major axis, and thus the physical radii of the stars. We then compared these masses and radii to the low mass models of Baraffe et al. (2015) to determine the true inclination. Figure 5.22 shows the results of our JKTEBOP MC analysis at different inclinations plotted on a mass-radius plot. We overplotted the Baraffe et al. (2015) models for different system ages and see that, for the best-fitting radii obtain through our fits, the inclination must be $i \approx 80°$, regardless of system age. We then performed one final iteration of this procedure with this new, fixed, inclination to determine the companion's mass and radius.

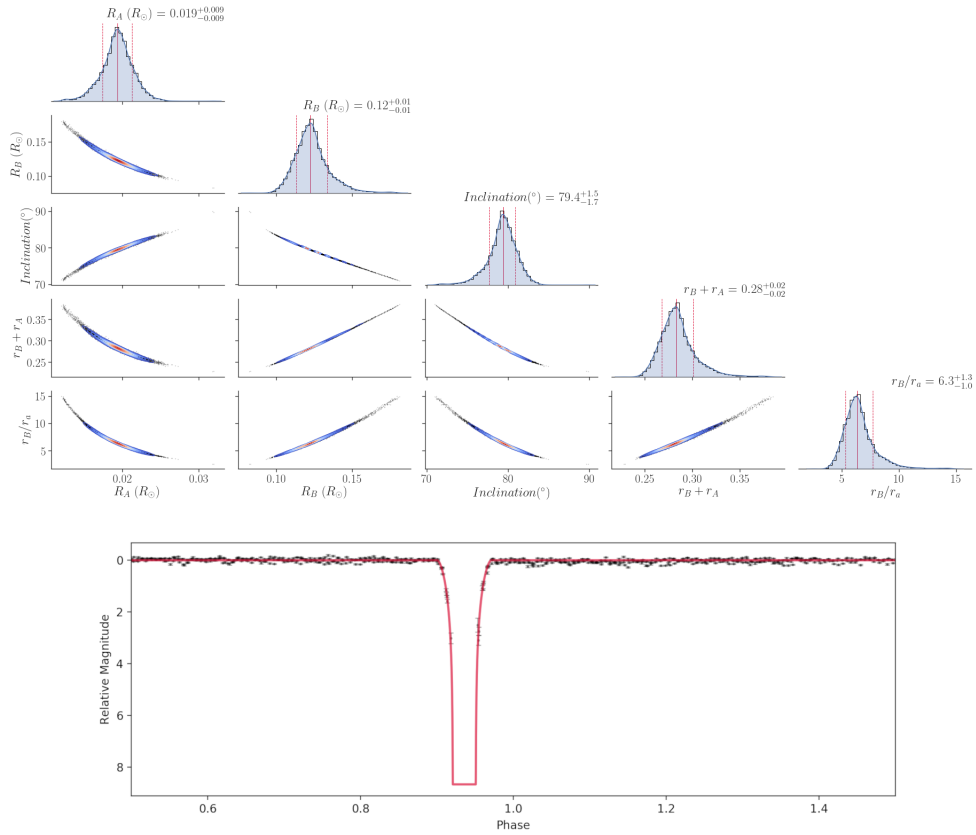

Fig. 5.21.— Top: Corner plot showing the 1D Monte Carlo parameter distributions for the APO BG40 light curve for J2212+5347 on the diagonal with 2D distributions in the off-diagonal Bottom: APO BG40 light curve for J2212+5347 (black) with the best-fit model overplotted in red.

5.4 Summary

We presented the results of our box least squares variability search on the public ZTF data release 4 archival data for white dwarfs within Gaia DR2. We presented the light curves for 50 variable binary systems, including one contact binary, five accreting binaries, 10 subdwarf binaries, 11 likely white dwarf binaries, 14 likely main sequence binaries, and nine white dwarf binaries with low-mass main sequence companions. Our search demonstrated the effectiveness of the box-least squares algorithm for identifying eclipsing binary systems in bulk light curve data, but simultaneously demonstrated the inefficiency for identifying other types of variability.

Our broad search made use of the entire Gaia DR2 white dwarf catalogue of Gentile Fusillo et al. (2019) without any attempt to remove contaminants so it is no surprise that we find a high degree of non-white dwarf contamination. Gentile Fusillo et al. (2021) has since compiled an updated catalogue of white dwarfs within Gaia's early Data Release 3, making use of the improved astrometry that this new data release provides. Their new catalogue contains nearly 1,280,266 white dwarf candidates with 359,073 high confidence ($P_{WD} > 0.75$) white dwarfs. We plan to make use of this new catalogue of white dwarfs in a future search for variability.

Future work making use of the other period-finding algorithms such as the Lomb Scargle periodogram, conditional entropy, and analysis of variance will be necessary to identify sinusoidally variable systems. While large survey astronomy programs such as ZTF allow for quick and efficient identification of scientifically valuable astrophysical phenomena, additional follow-up including spectroscopy or multi-bandpass photometry

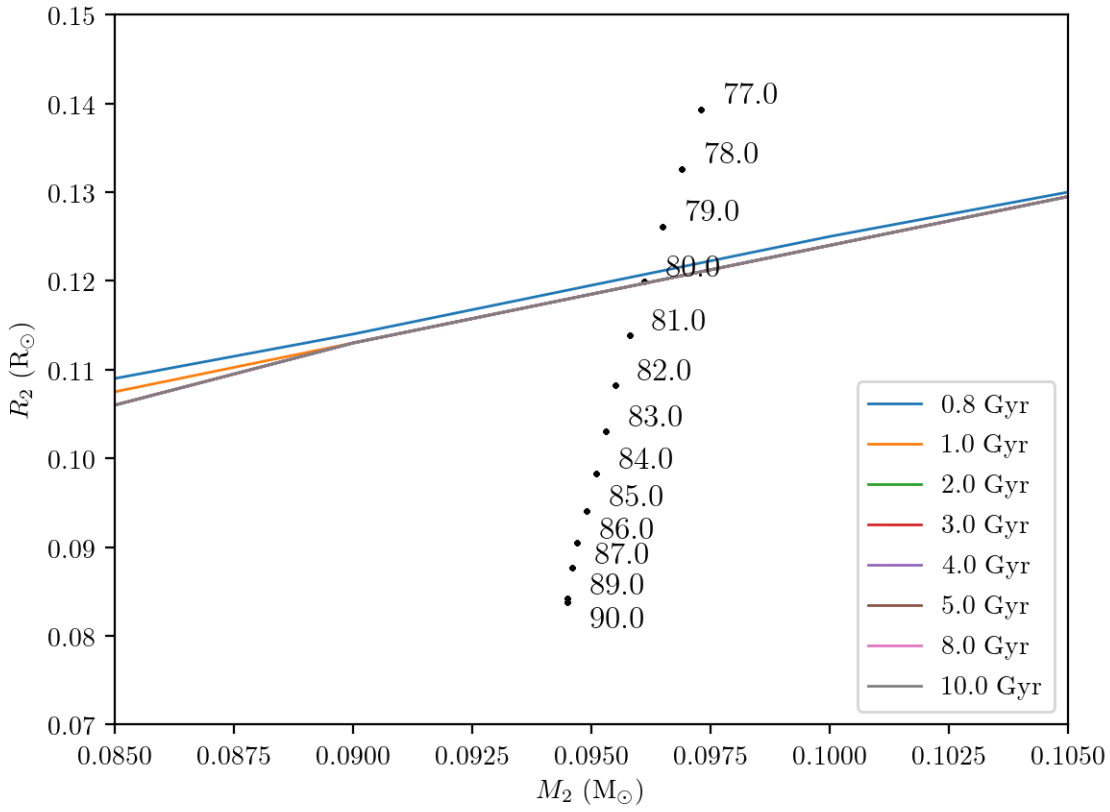

Fig. 5.22.— Companion radius vs. mass plot for J2212+5347. The black data points mark the best-fitting JKTEBOP model light curve parameters to the APO BG40 light curve of J2212+5347 for a fixed inclination. We overplotted the low-mass stellar models of Baraffe et al. (2015) for varying system ages to determine which inclination to adopt.

is almost always necessary to fully constrain the properties of these systems.

The results ZTF has yielded so far in the Northern sky have provided valuable insight into the results we expect for future Southern sky surveys, such as BlackGEM and the Vera Rubin Observatory LSST program. Advanced identification and analysis techniques developed throughout ZTF will remain useful for future large astronomical survey programs.

5.5 Acknowledgements

This work was supported in part by the NSF under grant AST-1906379. This research is based in part on observations obtained with the Apache Point Observatory 3.5-meter telescope, which is owned and operated by the Astrophysical Research Consortium

This research made use of Astropy,[2] a community-developed core Python package for Astronomy (Astropy Collaboration et al., 2013, 2018).

This research has made use of the Keck Observatory Archive (KOA), which is operated by the W. M. Keck Observatory and the NASA Exoplanet Science Institute (NExScI), under contract with the National Aeronautics and Space Administration.

[2]http://www.astropy.org

Chapter 6

Chapter Summaries and Future Works

This dissertation has presented new follow-up observations of low mass white dwarfs and identified new, and re-identified previously known, exotic variables in astronomical survey data. Here I present a summary of the results from each chapter of this dissertation.

6.1 Chapter 3 Summary

In Chapter 3 I presented our detailed study of the compact, double-degenerate, eclipsing low-mass white dwarf binary SDSS J082239.54+304857.19 with an orbital period P = 40.5 min. J0822+3048 was identified in our ELM Survey SDSS target selection through spectroscopic fitting. Our original spectroscopic follow-up and eclipse-discovery publication used multi-epoch optical spectroscopy to confirm the presence of a companion. Our single epoch of follow-up photometry then confirmed the presence of eclipses. However, due to the incredibly short eclipse duration in the eclipse-discovery data set, we were unable to precisely constrain the stellar radii or the secondary white dwarf's temperature.

Our work presented in Chapter 3 made use of two additional epochs of APO 3.5-meter photometry with a nearly one-year baseline to constrain the radius of both white dwarfs, providing verification for the theoretical white dwarf mass-radius relation for He- and CO-core white dwarf models. We then used simultaneous multi-band photometry from the Gemini North 8.1-meter telescope to estimate the temperature of the secondary white dwarf to be $T_{eff,2}$ = 5200 ± 100 K, in contrast with the temperature of the primary white

dwarf $T_{eff,1} = 13,920 \pm 255$ K. Our precise eclipse timing measurements from our our two new epochs present a unique opportunity to directly measure the orbital decay of this system caused by emission gravitational waves. While our ≈ 1 yr baseline is not sufficient to measure the orbital decay of this system, we estimated that a 3σ-significant measurement of the orbital decay due to gravitational waves will be possible in 2023. Deviations from our predicted value may be used to estimate the contribution from tidal interactions to the orbital decay, although a significantly longer baseline would be required to accurately measure the contribution from tides on this binary's orbital decay (see Burdge et al., 2019c).

6.2 Chapter 4 Summary

In Chapter 4 we expanded the completed ELM Survey into the southern sky through use of the ATLAS and SkyMapper photometric surveys and Gaia DR2 parallax measurements to perform a large, targeted, spectroscopic survey of low mass white dwarf candidates in the southern sky using the SOAR 4.1-meter telescope. We obtained optical spectra of over 530 unique objects and performed spectroscopic fitting on each spectrum to determine the surface gravity and effective temperatures for each object. Objects consistent with low mass white dwarfs were followed up further with time-series spectroscopy to measure radial velocity variations indicative of a companion, which were used to estimate minimum companion masses and merger timescales.

As the first part of an extended spectroscopic survey for ELM white dwarfs in the southern sky, this ELM Survey South has introduced nine new ELM white dwarfs and 26

new low mass white dwarfs in the southern sky, a significant addition to the completed ELM Survey's sample of 98 white dwarf binaries including 62 ELM white dwarfs. While the ELM Survey South is just beginning, our results from ATLAS DR2, SkyMapper DR1, and Gaia DR2 yielded a large sample of southern-sky white dwarf binaries. Direct comparison with the results from the completed ELM Survey, including kinematics and distribution, will require a larger, more complete, sample of low mass white dwarfs in the southern sky. Future ELM South publications will take advantage of improved ATLAS and SkyMapper photometry as well as improved Gaia astrometry in eDR3 to create a more effective target selection strategy.

Among our nine new ELM white dwarfs, we identify the closest and brightest known ELM white dwarf at the time of original publication, J0500−0930 ($d \approx 72$ pc). The orbit of J0500−0930, determined through our time-series spectroscopic follow-up, is confirmed in the public TESS light curve data through photometric variation with amplitude $A = 0.074^{+0.008}_{-0.007}$%, roughly consistent with the expected variability caused by relativistic beaming, diluted by nearby stars in the relatively large (≈ 21 arcsec) pixels of TESS.

6.3 Chapter 5 Summary

In Chapter 5 we began an expanded search for white dwarf binaries using the public data archive to the Zwicky Transient Facility Data Release 4. We construct a list of 2,498 potential variables from a catalogue of 486,641 white dwarf candidates in Gaia DR2 (Gentile Fusillo et al., 2019). Through a box-least squares period-finding analysis, we

identify 62 clearly-variable systems showing eclipse-like variability. Our 62 variables include one known contact binary, four known deeply-eclipsing cataclysmic variables, one known eclipsing AM CVn binary, 11 compact double white dwarf binaries with periods as low as $P \approx 24$ min (including nine new discoveries), 10 eclipsing subdwarf binaries (including eight new discoveries), nine deeply-eclipsing white dwarf binaries with low-mass main sequence companions, and 14 likely sequence binaries including two previously known Algol-type variables.

We fitted the light curves to seven of our new HW Vir-type binaries which returned well-sampled ZTF r-band light curves and estimate the orbital inclination, reflected light contribution, and fractional radii of the stars within the binary. Having a large sample of well-constrained post-common envelope binaries containing low-mass companions is important to determining the lower mass limit for envelope ejection during the common-envelope phase of pre-white dwarf evolution. Our sample of 10 HW Vir binaries introduced four new discoveries to the sample of $\lesssim 200$ HW Vir-type binaries known. Spectroscopic follow-up of the seven fitted systems presented here will be necessary to constrain the individual masses, temperatures, radii, and evolutionary history of these systems.

We obtained follow-up photometry and spectroscopy of four deeply-eclipsing white dwarf binaries with periods less than $P = 3$ h. Their orbital periods, eclipse depths, and eclipse durations suggested the possibility for substellar companions, which are exceptionally rare given that planetary companions are expected to be destroyed in common-envelope evolution depending on their masses and distance from their host star. Optical-IR SEDs for these binaries show significant IR excess, suggesting low-mass main

sequence companions. Our follow-up analysis for each system is consistent with white dwarf primary stars and low mass ($M \approx 0.1$ M$_\odot$) main sequence companions.

Among our short-period white dwarf binaries, we identify J1356+5705 with a period of $P = 46.0$ min based on the ZTF light curve. Archival Keck LRIS spectroscopy radial velocity measurements place the true period at $P \approx 92$ min, revealing that the orbital period is twice the value obtained from our BLS period search. Inspection of the Keck LRIS blue-optical spectra show evidence that this system is a double-lined eclipsing binary. However, due to the low resolution of the Keck LRIS data, we are unable to fit an orbit to each component's Balmer lines individually. Given the faintness of J1356+5705 (*Gaia* G = 18.95 mag), follow-up high-resolution time-series spectroscopy with an 8-10 meter class telescope will be needed to individually resolve the Balmer lines for each star and perform a simultaneous analysis of each star in the binary.

Our search showed the effectiveness for finding eclipsing binaries in public astronomical survey data. However, because our period finding algorithm is designed to identify only eclipse-like variability, we do not recover other sources of variability, such as relativistic beaming or tidal distortions. These sinusoidally-varying variables are considerably more common considering that they are not as inclination-restricted as eclipses. To identify more common types of variability, we are currently using the Lomb Scargle periodogram to identify sinusoidally varying systems in the ZTF public data archive.

As more survey data is obtained and released, the temporal and phase sampling for variable systems will increase, thus allowing for the discovery of more exotic, and longer-period, variables. With the release of Gaia eDR3, Gentile Fusillo et al. (2021) have

released an updated white dwarf catalogue containing 1,280,266 white dwarf, including nearly 360,000 high-confidence white dwarf candidates with improved selection criteria. Future work making use of this improved Gaia eDR3 white dwarf sample in combination with current and future large-scale astronomical sky surveys will have a significant impact on the field of compact white dwarf binaries as post-common envelope systems and strong mHz frequency gravitational wave sources. Burdge et al. (2020a) have used the entire ZTF data archive and have clearly shown the effectiveness for identifying these ultra-compact white dwarf binaries in large-scale astronomical surveys.

The methods presented in Chapter 5 on identifying white dwarf binaries in ZTF are directly applicable to identifying white dwarf binaries in future large-scale astronomical surveys in the southern hemisphere, including BlackGEM ($\approx$ 2021) and the Vera Rubin Observatory LSST program ($\approx$ 2023). Variability searches using data from these upcoming large-scale surveys will be used as an effective target selection method for the ELM Survey South in combination with the photometric & astrometric target selection methods with ATLAS, SkyMapper, and Gaia.

References

Althaus, L. G., Miller Bertolami, M. M., & Córsico, A. H. 2013, A&A, 557, A19. doi:10.1051/0004-6361/201321868

Amaro-Seoane, P., Audley, H., Babak, S., et al. 2017, arXiv:1702.00786

Astropy Collaboration, Robitaille, T. P., Tollerud, E. J., et al. 2013, A&A, 558, A33

Astropy Collaboration, Price-Whelan, A. M., Sipőcz, B. M., et al. 2018, AJ, 156, 123

Bailer-Jones, C. A. L., Rybizki, J., Fouesneau, M., et al. 2021, AJ, 161, 147. doi:10.3847/1538-3881/abd806

Baraffe, I., Homeier, D., Allard, F., et al. 2015, A&A, 577, A42. doi:10.1051/0004-6361/201425481

Bédard, A., Bergeron, P., Brassard, P., et al. 2020, ApJ, 901, 93. doi:10.3847/1538-4357/abafbe

Bellm, E. C., Kulkarni, S. R., Graham, M. J., et al. 2019, PASP, 131, 018002. doi:10.1088/1538-3873/aaecbe

Bessell, M., Bloxham, G., Schmidt, B., et al. 2011, PASP, 123, 789

Benacquista M. J., 2011, ApJL, 740, L54

Bergeron, P., Saffer, R. A., & Liebert, J. 1992, ApJ, 394, 228. doi:10.1086/171575

Bergeron, P., Wesemael, F., Lamontagne, R., et al. 1995, ApJ, 449, 258. doi:10.1086/176053

Brown, W. R., Geller, M. J., Kenyon, S. J., et al. 2006a, ApJ, 640, L35. doi:10.1086/503279

Brown, W. R., Geller, M. J., Kenyon, S. J., et al. 2006b, ApJ, 647, 303. doi:10.1086/505165

Brown, W. R., Kilic, M., Allende Prieto, C., et al. 2010, ApJ, 723, 1072

Brown, W. R., Kilic, M., Hermes, J. J., et al. 2011, ApJ, 737, L23

Brown, W. R., Kilic, M., Allende Prieto, C., et al. 2012, ApJ, 744, 142. doi:10.1088/0004-637X/744/2/142

Brown, W. R., Geller, M. J., & Kenyon, S. J. 2014, ApJ, 787, 89

Brown, W. R., Gianninas, A., Kilic, M., et al. 2016a, ApJ, 818, 155

Brown, W. R., Kilic, M., Kenyon, S. J., et al. 2016b, ApJ, 824, 46

Brown, W. R., Kilic, M., Kosakowski, A., et al. 2017, ApJ, 847, 10. doi:10.3847/1538-4357/aa8724

Brown, W. R., Kilic, M., & Gianninas, A. 2017b, ApJ, 839, 23

Brown W. R., Kilic M., Kosakowski A., Andrews J. J., Heinke C. O., Agüeros M. A., Camilo F., et al., 2020a, ApJ, 889, 49

Brown, W. R., Kilic, M., Kosakowski, A., et al. 2020b, ApJ, 889, 1

Burdge, K. B., Coughlin, M. W., Fuller, J., et al. 2019a, Nature, 571, 528

Burdge, K. B., Yan, L., Prince, T., et al. 2019b, The Astronomer's Telegram, 12959, 1

Burdge K. B., Fuller J., Phinney E. S., van Roestel J., Claret A., Cukanovaite E., Gentile Fusillo N. P., et al., 2019c, ApJL, 886, L12

Burdge, K. B., Prince, T. A., Fuller, J., et al. 2020a, ApJ, 905, 32. doi:10.3847/1538-4357/abc261

Burdge K. B., Coughlin M. W., Fuller J., Kaplan D. L., Kulkarni S. R., Marsh T. R., Prince T. A., et al., 2020b, arXiv, arXiv:2010.03555

Campbell, H. C., Marsh, T. R., Fraser, M., et al. 2015, MNRAS, 452, 1060. doi:10.1093/mnras/stv1224

Canton, P. A., Williams, K., Gianninas, A., et al. 2019, American Astronomical Society Meeting Abstracts #233

Chandrasekhar, S. 1931, ApJ, 74, 81. doi:10.1086/143324

Cheng, S., Cummings, J. D., Ménard, B., et al. 2020, ApJ, 891, 160. doi:10.3847/1538-4357/ab733c

Claret A., Cukanovaite E., Burdge K., Tremblay P.-E., Parsons S., Marsh T. R., 2020, A&A, 634, A93

Clemens, J. C., Crain, J. A., & Anderson, R. 2004, Proc. SPIE, 331

Coughlin M. W., Burdge K., Phinney E. S., van Roestel J., Bellm E. C., Dekany R. G., Delacroix A., et al., 2020, MNRAS, 494, L91

Cummings, J. D., Kalirai, J. S., Tremblay, P.-E., et al. 2018, ApJ, 866, 21. doi:10.3847/1538-4357/aadfd6

Dieterich, S. B., Henry, T. J., Jao, W.-C., et al. 2014, AJ, 147, 94. doi:10.1088/0004-6256/147/5/94

Drake, A. J., Djorgovski, S. J., Mahabal, A., et al. 2009, ApJ, 696, 870

Drake A. J., Beshore E., Catelan M., Djorgovski S. G., Graham M. J., Kleinman S. J., Larson S., et al., 2010, arXiv, arXiv:1009.3048

Drake, A. J., Graham, M. J., Djorgovski, S. G., et al. 2014, ApJS, 213, 9. doi:10.1088/0067-0049/213/1/9

Drake, A. J., Djorgovski, S. G., Catelan, M., et al. 2017, MNRAS, 469, 3688

Daou, D., Wesemael, F., Bergeron, P., et al. 1990, ApJ, 364, 242. doi:10.1086/169407

Dufour, P., Blouin, S., Coutu, S., et al. 2017, 20th European White Dwarf Workshop, 509, 3

Eastman J., Siverd R., Gaudi B. S., 2010, PASP, 122, 935

Elenin, L. 2009, Peremennye Zvezdy Prilozhenie, 9, 16

Enenstein, J., Burdge, K., & Prince, T. 2021, Research Notes of the American Astronomical Society, 5, 90. doi:10.3847/2515-5172/abf4d3

Feinstein, A. D., Montet, B. T., Foreman-Mackey, D., et al. 2019, PASP, 131, 094502

Fontaine G., Brassard P., Bergeron P., 2001, PASP, 113, 409

Fuller J., Lai D., 2013, MNRAS, 430, 274. doi:10.1093/mnras/sts606

Gaia Collaboration, Prusti, T., de Bruijne, J. H. J., et al. 2016, A&A, 595, A1. doi:10.1051/0004-6361/201629272

Geier, S., Raddi, R., Gentile Fusillo, N. P., et al. 2019, A&A, 621, A38. doi:10.1051/0004-6361/201834236

Gentile Fusillo, N. P., Tremblay, P.-E., Gänsicke, B. T., et al. 2019, MNRAS, 482, 4570

Gentile Fusillo, N. P., Tremblay, P.-E., Gänsicke, B. T., et al. 2019, MNRAS, 482, 4570

Gentile Fusillo, N. P., Tremblay, P.-E., Cukanovaite, E., et al. 2021, arXiv:2106.07669

Gianninas, A., Bergeron, P., & Ruiz, M. T. 2011, ApJ, 743, 138

Gianninas A., Strickland B. D., Kilic M., Bergeron P., 2013, ApJ, 766, 3

Gianninas, A., Dufour, P., Kilic, M., et al. 2014, ApJ, 794, 35

Geier, S., Raddi, R., Gentile Fusillo, N. P., et al. 2019, A&A, 621, A38

Graham, M. J., Drake, A. J., Djorgovski, S. G., et al. 2013, MNRAS, 434, 2629. doi:10.1093/mnras/stt1206

Gronow, S., Collins, C. E., Sim, S. A., et al. 2021, A&A, 649, A155. doi:10.1051/0004-6361/202039954

Groot, P., Bloemen, S., & Jonker, P. 2019, The La Silla Observatory - From the Inauguration to the Future, 33. doi:10.5281/zenodo.3471366

Hallakoun N., Maoz D., Kilic M., Mazeh T., Gianninas A., Agol E., Bell K. J., et al., 2016, MNRAS, 458, 845

Hansen, B. M. S., Kalirai, J. S., Anderson, J., et al. 2013, Nature, 500, 51. doi:10.1038/nature12334

Harrigan, M. J., Newberg, H. J., Newberg, L. A., et al. 2010, MNRAS, 405, 1796. doi:10.1111/j.1365-2966.2010.16552.x

Hermes J. J., Kilic M., Brown W. R., Winget D. E., Allende Prieto C., Gianninas A., Mukadam A. S., et al., 2012, ApJL, 757, L21

Istrate A. G., Marchant P., Tauris T. M., Langer N., Stancliffe R. J., Grassitelli L., 2016, A&A, 595, A35

Ivezić, Ž., Kahn, S. M., Tyson, J. A., et al. 2019, ApJ, 873, 111. doi:10.3847/1538-4357/ab042c

Justham, S., Wolf, C., Podsiadlowski, P., et al. 2009, A&A, 493, 1081

Kalirai, J. S., Hansen, B. M. S., Kelson, D. D., et al. 2008, ApJ, 676, 594. doi:10.1086/527028

Kalirai, J. S. 2012, Nature, 486, 90. doi:10.1038/nature11062

Kaplan, D. L., Marsh, T. R., Walker, A. N., et al. 2014, ApJ, 780, 167

Kao, W., Kaplan, D. L., Prince, T. A., et al. 2016, MNRAS, 461, 2747. doi:10.1093/mnras/stw1434

Keller, P. M., Breedt, E., Hodgkin, S., et al. 2021, arXiv:2105.14028

Kenyon, S. J., & Garcia, M. R. 1986, AJ, 91, 125

Kepler, S. O., Pelisoli, I., Koester, D., et al. 2016, MNRAS, 455, 3413

Kilic, M., Stanek, K. Z., & Pinsonneault, M. H. 2007, ApJ, 671, 761

Kilic, M., Brown, W. R., Allende Prieto, C., et al. 2010, ApJ, 716, 122. doi:10.1088/0004-637X/716/1/122

Kilic, M., Brown, W. R., Allende Prieto, C., et al. 2011, ApJ, 727, 3

Kilic M., Hermes J. J., Gianninas A., Brown W. R., Heinke C. O., Agüeros M. A., Chote P., et al., 2014a, MNRAS, 438, L26

Kilic, M., Brown, W. R., Gianninas, A., et al. 2014b, MNRAS, 444, L1

Kilic, M., Gianninas, A., Bell, K. J., et al. 2015, ApJ, 814, L31. doi:10.1088/2041-8205/814/2/L31

Kilic, M., Bergeron, P., Dame, K., et al. 2019, MNRAS, 482, 965. doi:10.1093/mnras/sty2755

Kilic, M., Bergeron, P., Kosakowski, A., et al. 2020, ApJ, 898, 84. doi:10.3847/1538-4357/ab9b8d

Kochanek, C. S., Shappee, B. J., Stanek, K. Z., et al. 2017, PASP, 129, 104502

Korol, V., Rossi, E. M., Groot, P. J., et al. 2017, MNRAS, 470, 1894

Kosakowski A., Kilic M., Brown W. R., Gianninas A., 2020a, ApJ, 894, 53

Kosakowski, Alekzander, Kilic, Mukremin, Brown, Warren, & Gianninas, Alexandros. (2020b). The ELM Survey South I [Data set]. Zenodo. http://doi.org/10.5281/zenodo.3635104

Korol, V., Rossi, E. M., & Barausse, E. 2019, MNRAS, 483, 5518. doi:10.1093/mnras/sty3440

Kovács G., Zucker, S., & Mazeh, T., 2002, A&A, 391, 369-377

Kremer, K., Breivik, K., Larson, S. L., et al. 2017, ApJ, 846, 95

Kurtz, M. J. & Mink, D. J. 1998, PASP, 110, 934. doi:10.1086/316207

Lamberts, A., Blunt, S., Littenberg, T. B., et al. 2019, MNRAS, 490, 5888

Landau, L. D., & Lifshitz, E. M., 1958, The Classical Theory of Fields, (Oxford: Oxford Pergamon Press)

Lauffer, G. R., Romero, A. D., & Kepler, S. O. 2018, MNRAS, 480, 1547

Law, N. M., Kulkarni, S. R., Dekany, R. G., et al. 2009, PASP, 121, 1395. doi:10.1086/648598

Li, Z., Chen, X., Chen, H.-L., et al. 2019, ApJ, 871, 148

Liu, D., Wang, B., & Han, Z. 2018, MNRAS, 473, 5352. doi:10.1093/mnras/stx2756

Liebert, J., Dahn, C. C., & Monet, D. G. 1988, ApJ, 332, 891. doi:10.1086/166699

Liebert, J., Bergeron, P., & Holberg, J. B. 2005, ApJS, 156, 47. doi:10.1086/425738

Lindegren, L., Hernández, J., Bombrun, A., et al. 2018, A&A, 616, A2

Lomb, N. R. 1976, Ap&SS, 39, 447. doi:10.1007/BF00648343

Marsh, T. R., Nelemans, G., & Steeghs, D. 2004, MNRAS, 350, 113

Masci, F. J., Laher, R. R., Rusholme, B., et al. 2019, PASP, 131, 018003. doi:10.1088/1538-3873/aae8ac

Maoz, D., Hallakoun, N., & Badenes, C. 2018, MNRAS, 476, 2584. doi:10.1093/mnras/sty339

Mukadam A. S., Owen R., Mannery E., MacDonald N., Williams B., Stauffer F., Miller C., 2011, PASP, 123, 1423

Nomoto, K. & Iben, I. 1985, ApJ, 297, 531. doi:10.1086/163547

Nelemans, G., Yungelson, L. R., & Portegies Zwart, S. F. 2001, A&A, 375, 890

Nissanke, S., Vallisneri, M., Nelemans, G., et al. 2012, ApJ, 758, 131

Nomoto, K. 1982a, ApJ, 253, 798. doi:10.1086/159682

Nomoto, K. 1982b, ApJ, 257, 780. doi:10.1086/160031

Nomoto, K. 1984, ApJ, 277, 791. doi:10.1086/161749

Nomoto, K. 1986, Progress in Particle and Nuclear Physics, 17, 249. doi:10.1016/0146-6410(86)90020-7

Parsons S. G., Marsh T. R., Gänsicke B. T., Drake A. J., Koester D., 2011, ApJL, 735, L30

Parsons S. G., Gänsicke B. T., Marsh T. R., et al. 2017, MNRAS, 471, 4473

Parsons S. G., Hermes, J. J., Marsh T. R., et al. 2017, MNRAS, 470, 976. doi:10.1093/mnras/stx1610

Pelisoli, I., Kepler, S. O., & Koester, D. 2018a, MNRAS, 475, 2480

Pelisoli, I., Kepler, S. O., Koester, D., et al. 2018b, MNRAS, 478, 867

Pelisoli, I., Bell, K. J., Kepler, S. O., et al. 2019, MNRAS, 482, 3831

Pelisoli, I., & Vos, J. 2019, MNRAS, 488, 2892

Pietrukowicz, P., Mróz, P., Soszyński, I., et al. 2013, Acta Astron., 63, 115

Piro A. L., 2011, ApJL, 740, L53

Press, William H. Numerical Recipes in C++: The Art of Scientific Computing. Cambridge, Cambridge University Press, 2002.

Polin, A., Nugent, P., & Kasen, D. 2019, ApJ, 873, 84. doi:10.3847/1538-4357/aafb6a

Rappaport, S., Vanderburg, A., Schwab, J., et al. 2021, ApJ, 913, 118. doi:10.3847/1538-4357/abf7b0

Ricker, G. R., Winn, J. N., Vanderspek, R., et al. 2015, Journal of Astronomical Telescopes, Instruments, and Systems, 1, 014003. doi:10.1117/1.JATIS.1.1.014003

Rowan, D. M., Tucker, M. A., Shappee, B. J., et al. 2019, MNRAS, 486, 4574. doi:10.1093/mnras/stz1116

Savoury, C. D. J., Littlefair, S. P., Dhillon, V. S., et al. 2011, MNRAS, 415, 2025. doi:10.1111/j.1365-2966.2011.18707.x

Scargle, J. D. 1982, ApJ, 263, 835. doi:10.1086/160554

Schaffenroth, V., Classen, L., Nagel, K., et al. 2014, A&A, 570, A70. doi:10.1051/0004-6361/201424616

Schaffenroth, V., Barlow, B. N., Geier, S., et al. 2019, A&A, 630, A80. doi:10.1051/0004-6361/201936019

Schindewolf, M., Levitan, D., Heber, U., et al. 2015, A&A, 580, A117. doi:10.1051/0004-6361/201425581

Schlegel, D. J., Finkbeiner, D. P., & Davis, M. 1998, ApJ, 500, 525

Scholz, R.-D., Meusinger, H., Schwope, A., et al. 2018, A&A, 619, A31

Schwab, J. 2021, ApJ, 906, 53. doi:10.3847/1538-4357/abc87e

Schwarzenberg-Czerny, A. 1996, ApJ, 460, L107. doi:10.1086/309985

Scott N. J., Howell S. B., 2018, SPIE, 10701, 107010G

Shanks, T., Metcalfe, N., Chehade, B., et al. 2015, MNRAS, 451, 4238

Shappee, B. J., Prieto, J. L., Grupe, D., et al. 2014, ApJ, 788, 48. doi:10.1088/0004-637X/788/1/48

Shen, K. J. 2015, ApJ, 805, L6

Shporer, A., Kaplan, D. L., Steinfadt, J. D. R., et al. 2010, ApJ, 725, L200

Silvestri, N. M., Hawley, S. L., West, A. A., et al. 2006, AJ, 131, 1674. doi:10.1086/499494

Sirko, E., Goodman, J., Knapp, G. R., et al. 2004, AJ, 127, 899. doi:10.1086/381483

Soker, N. 1998, AJ, 116, 1308. doi:10.1086/300503

Southworth J., Maxted P. F. L., Smalley B., 2004, MNRAS, 351, 1277. doi:10.1111/j.1365-2966.2004.07871.x

Southworth J., Smalley B., Maxted P. F. L., Claret A., Etzel P. B., 2005, MNRAS, 363, 529. doi:10.1111/j.1365-2966.2005.09462.x

Southworth J., 2013, A&A, 557, A119

Soszyński, I., Stępień, K., Pilecki, B., et al. 2015, Acta Astron., 65, 39

Steinfadt J. D. R., Kaplan D. L., Shporer A., Bildsten L., Howell S. B., 2010, ApJL, 716, L146

Szkody, P., Henden, A., Fraser, O. J., et al. 2005, AJ, 129, 2386. doi:10.1086/429595

Szkody, P., Henden, A., Agüeros, M., et al. 2006, AJ, 131, 973. doi:10.1086/499308

Szkody, P., Anderson, S. F., Hayden, M., et al. 2009, AJ, 137, 4011. doi:10.1088/0004-6256/137/4/4011

Tremblay, P.-E. & Bergeron, P. 2009a, Recent Directions in Astrophysical Quantitative Spectroscopy and Radiation Hydrodynamics, 1171, 101. doi:10.1063/1.3250051

Tremblay, P.-E., & Bergeron, P. 2009b, ApJ, 696, 1755

Tremblay P.-E., Bergeron P., Gianninas A., 2011a, ApJ, 730, 128

Tremblay, P.-E., Ludwig, H.-G., Steffen, M., et al. 2011b, A&A, 531, L19. doi:10.1051/0004-6361/201117310

Tremblay, P.-E., Gianninas, A., Kilic, M., et al. 2015, ApJ, 809, 148. doi:10.1088/0004-637X/809/2/148

Torres, S., Rebassa-Mansergas, A., Camisassa, M. E., et al. 2021, MNRAS, 502, 1753. doi:10.1093/mnras/stab079

Van Grootel, V., Dupret, M.-A., Fontaine, G., et al. 2012, A&A, 539, A87. doi:10.1051/0004-6361/201118371

Van Grootel, V., Fontaine, G., Brassard, P., et al. 2015, A&A, 575, A125. doi:10.1051/0004-6361/201425386

van Roestel, J., Kupfer, T., Bell, K. J., et al. 2021, arXiv:2105.08687

VanderPlas, J. T. 2018, ApJS, 236, 16. doi:10.3847/1538-4365/aab766

Vennes S., Thorstensen J. R., Kawka A., Németh P., Skinner J. N., Pigulski A., Ste&șacute, et al., 2011, ApJL, 737, L16

Vogel, J., Byckling, K., Schwope, A., et al. 2008, A&A, 485, 787. doi:10.1051/0004-6361:20079341

Webbink, R. F. 1984, ApJ, 277, 355. doi:10.1086/161701

Weidemann, V. & Koester, D. 1983, A&A, 121, 77

Wesemael, F., Greenstein, J. L., Liebert, J., et al. 1993, PASP, 105, 761. doi:10.1086/133228

Williams, K. A., Bolte, M., & Koester, D. 2009, ApJ, 693, 355. doi:10.1088/0004-637X/693/1/355

Winget, D. E., Hansen, C. J., Liebert, J., et al. 1987, ApJ, 315, L77. doi:10.1086/184864

Winget, D. E. & Kepler, S. O. 2008, ARA&A, 46, 157. doi:10.1146/annurev.astro.46.060407.145250

Wolf, C., Onken, C. A., Luvaul, L. C., et al. 2018, PASA, 35, e010

Woosley, S. E., & Heger, A. 2015, ApJ, 810, 34

Yu, J., Li, Z., Zhu, C., et al. 2019, ApJ, 885, 20

Zucker, S., Mazeh, T., & Alexander, T. 2007, ApJ, 670, 1326. doi:10.1086/521389